Nanostructured Oxide Semiconductors for Photoelectrochemical Cells

João Pedro Ferreira Freitas
Mestrado em Engenharia Física
Departamento de Física e Astronomia
2022

Dra. Arlete Apolinário
Orientador, Faculdade de Ciências da Universidade do Porto

Prof. João Pedro Esteves de Araújo
Coorientador, Faculdade de Ciências da Universidade do Porto

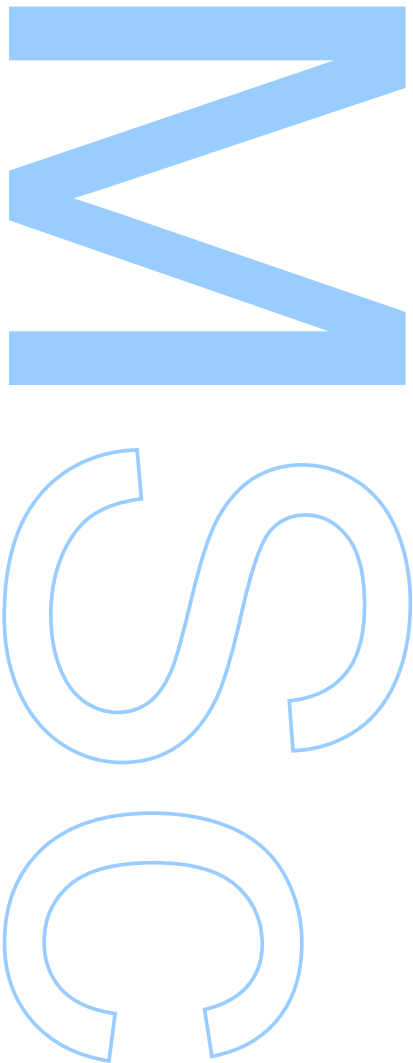

U.PORTO

FACULDADE DE CIÊNCIAS
UNIVERSIDADE DO PORTO

Todas as correções determinadas pelo júri, e só essas, foram efetuadas.

O Presidente do Júri,

Porto, _____/_____/_____

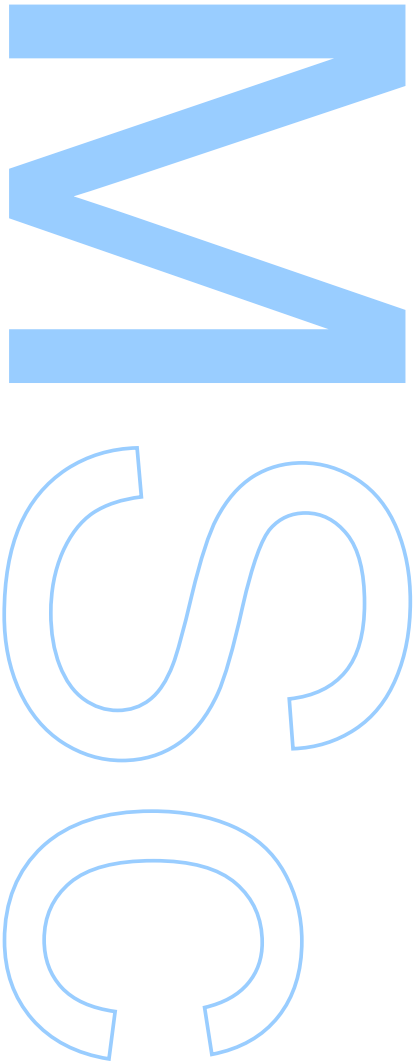

UNIVERSIDADE DO PORTO

MASTERS THESIS

Nanostructured Oxide Semiconductors for Photoelectrochemical Cells

Author:
João Pedro FREITAS

Supervisor:
Dra. Arlete APOLINÁRIO

Co-supervisor:
Prof. João Pedro ARAÚJO

A thesis submitted in fulfilment of the requirements
for the degree of MSc. Engineering Physics

at the

Faculdade de Ciências da Universidade do Porto
Departamento de Física e Astronomia
IFIMUP

December 30, 2022

Institutions involved

Funding:

This Master work was supported by FCT – Fundação para a Ciência e a Tecnologia (Portuguese Agency for Research) and the project NORTE-01-0145-FEDER-000076 (H2INNOVATE). Arlete Apolinário acknowledges FCT - Fundacao para a Ciencia e a Tecnologia, contract DL57/2016 reference SFRH/BPD/82010/2011 and project NORTE-01-0145-FEDER-000076 (H2INNOVATE).

Acknowledgements

I would like to express my deepest gratitude to everyone who directly or indirectly contributed and supported me during this thesis. To all of those without whom it would not have been possible. For all the guidance, help, support, friendship, I am truly thankful.

Firstly, I would like to thank my supervisor Doctor Arlete Apolinário for giving me the opportunity to work in a research area that motivates me so much, for welcoming me so well and for all the consideration, trust, friendship, help and support. To my co-supervisor Professor João Pedro Araújo, I thank the opportunity of being part of such a wonderful and prestigious research group and for insightful input regarding the results.

To Doctor Paula Quitério, a genuine friend and mentor, a special acknowledgement for all the constant support and dedication in guiding and assisting me with most of the laboratory and analysis procedures. This work would not have been possible without her incredible support and kindness.

I express my gratitude to the LEPABE-FEUP team, especially to Tânia Lopes, all the support, availability and kindness, for all the help with measurements and analysis of results, enabling me to learn so much about the EIS technique. Also, to Filipe Moisés, I am very thankful for the help and support with the measurements and for his sympathy.

I would like to express thanks to Doctor Sérgio Magalhães for his hospitality, kindness and availability in receiving me at the Technological and Nuclear Campus. It was an excellent learning opportunity and experience, which largely enriched the developed work.

To IFIMUP members who were always friendly and supportive: Pedro Rodrigues, Nenenu Nikhil, Bogdan Postolnyi, Armandina Lopes and João Horta.

I would also like to thank my dear colleague and friend Inês Ornelas for her good friendship over the past five years. Also, I would like to thank Carlos Teles for his camaraderie and Duarte Silva, who helped me to understand and complete many courses.

Agradeço profundamente à minha família por todo o apoio ao longo do meu percurso. À minha querida irmã Lara que me inspira a ser forte todos os dias, um agradecimento com carinho especial. À minha avó Clarisse por toda a energia enviada para que obtivesse sucesso no meu percurso, e ao meu avô José que sempre foi um modelo a seguir, um profundo obrigado. À minha tia Sónia por todas as vezes que me ligou para saber como eu estava, um grande obrigado. À minha mãe, avó Teresa e avó Clarisse por me fazerem sentir mais perto de casa, através

de toda a comida e lembranças que me mandavam. À Daniela, que desde há quatro anos aturame diariamente e com quem partilho um amor de quatro patas, a Bella, um profundo agradecimento com muito amor por seres uma fantástica namorada e melhor amiga com quem posso contar e falar de tudo.

Finalmente, ao meu adorado pai que sempre me incentivou a dar o melhor de mim, e à minha adorada mãe com quem sempre pude desabafar, palavras não servem para vos agradecer. Ambos fizeram tudo por mim, por todo o seu trabalho para darem a mim e à minha irmã tudo o de melhor, sacrificando-se todos os dias por nós, a eles devo tudo e por isso dedico-lhes esta tese.

Sworn Statement

I, João Pedro Ferreira Freitas, enrolled in the Master Degree Engineering Physics at the Faculty of Sciences of the University of Porto hereby declare, in accordance with the provisions of paragraph a) of Article 14 of the Code of Ethical Conduct of the University of Porto, that the content of this dissertation reflects perspectives, research work and my own interpretations at the time of its submission.

By submitting this dissertation, I also declare that it contains the results of my own research work and contributions that have not been previously submitted to this or any other institution.

I further declare that all references to other authors fully comply with the rules of attribution and are referenced in the text by citation and identified in the bibliographic references section. This dissertation does not include any content whose reproduction is protected by copyright laws.

I am aware that the practice of plagiarism and self-plagiarism constitute a form of academic offense.

João Pedro Ferreira Freitas

30/12/2022

UNIVERSIDADE DO PORTO

Abstract

Faculdade de Ciências da Universidade do Porto

Departamento de Física e Astronomia

IFIMUP

MSc. Engineering Physics

Nanostructured Oxide Semiconductors for Photoelectrochemical Cells

by João Pedro FREITAS

In recent years, hydrogen (H_2) has gained popularity as a strategic energy source, though 95 % of the global hydrogen produced derives from fossil sources. Although the challenge of implementing a green route to produce (green) hydrogen has already been established by water electrolysis through the use of electrolyzers, this approach is extremely dependent on external sources of energy, typically photovoltaic panels. Photoelectrochemical (PEC) cells arise as a clean and low cost alternative for direct production of H_2 using only sunlight and water as primary sources. Basically, a PEC cell consists in a semiconductor which, by the incidence of solar radiation, generates electron-hole pairs that subsequently participate in the water-splitting reaction, producing dispatchable hydrogen fuel. However, the challenge of finding a semiconductor that fulfills all the requirements for sustainable PEC device, such as efficiency, low cost, stability, non-toxicity, and scalability, still leaves this H_2 production technique in a widely and intensive research and development topic.

Oxide semiconductors, such as hematite (α-Fe_2O_3) and tungsten trioxide (WO_3), have gathered increasing attention due to their abundance, low-cost, non-toxicity and scalability, making them suitable options for PEC cells applications. In particular, hematite is considered a promising candidate due to its narrow optical band gap (2.2 eV), long-term stability and natural abundance, reaching 12.9 % solar-to-hydrogen efficiency in theory.

This dissertation focuses on the development and optimization of efficient semiconductor oxide photoanodes based on hematite, by combining different strategies, nanostructuring and elemental doping, to improve the overall PEC performance. Photoanodes based on 1D bare hematite nanowires (NWs) were obtained through two hydrothermal route. The role of the oxidizing agent, sodium nitrate ($NaNO_3$) or urea (CH_4N_2O), in the hydrothermal synthesis was

studied. Furthermore, an elemental doping of several suitable metals on the bare hematite was conducted. Mn, Co and Ti doping elements were tested, along with a study of effect of their doping concentrations (C_{dopant}), and related with the output of the photocurrent (j) output of the PEC cell. Besides the photo performance, morphology, optical, and structural by means of X-Ray Diffraction (XRD) and Rutherford Backscattering Spectrometry (RBS) characterizations techniques were carried out and their results related to the underlying physical-chemical characteristics of the photoanodes.

Here, the oxidation agent unveiled a strong impact on the synthesis of both undoped (bare, C_{dopant} = 0 %) and doped hematite NWs. The smaller thickness along with a higher conductivity suggested by the structural preferential growing in the (110) plane and higher Sn diffusion were considered the main players for the enhanced j response of method using $NaNO_3$ as the oxidizing agent. The introduction of the Mn dopant showed no j improvements in method A ($NaNO_3$), whereas in method B (urea), a 7 % Mn C_{dopant} achieved a 37 % increase in j response compared to the respective bare hematite photoanode. This increase was associated with an enhanced crystallinity quality and thinner thickness. Additionally, RBS measurements suggested that the Mn dopant promoted a higher Sn diffusion, which is associated with higher conductivity that ultimately leads to best j. Furthermore, an onset potential (V_{onset}) decrease was observed, reaching remarkable cathodic shifts of 70 mV and 60 mV for method A ($NaNO_3$) and method B (urea), respectively. This result is rather important and such shift values are not usually found in the literature putting this work in front of a novel result. On other hand, the introduction of the Co dopant for both methods, $NaNO_3$ and urea, did not result in j improvement, however, it proved to be beneficial for the decrease of V_{onset}, reaching cathodic shifts of 40 mV and 30 mV for 1 % in method A ($NaNO_3$) and 7 % in method B (urea), respectively. Finally, Ti doping with method A ($NaNO_3$) showed an optimum C_{dopant} of 0.5 %, reaching a $j \sim 0.9$ mA·cm^{-2} at 1.45 V_{RHE} (15.5 % increase response compared to bare hematite). This was associated with an increase in the effective surface area and an enhanced crystallinity quality.

In addition, Electrochemical Impedance Spectroscopy (EIS) was performed on WO_3 nanoplates multilayers synthesized by hydrothermal method in an attempt to better understand the effect that the number of layers has on electrochemical performance. EIS features corroborated the j-V results with the 5 layers sample achieving the lowest resistance to charge transfer between the semiconductor/electrolyte interface and lower flat-band potential, thereby, reinforcing the optimum WO_3 nanoplates photoanode was achieved with 5 layers.

UNIVERSIDADE DO PORTO

Resumo

Faculdade de Ciências da Universidade do Porto

Departamento de Física e Astronomia

IFIMUP

Mestrado em Engenharia Física

Semicondutores de Óxidos Nanoestruturados para Células Fotoeletroquímicas

por João Pedro FREITAS

Nos últimos anos, o hidrogénio (H_2) tem vindo a ganhar popularidade como uma fonte estratégica de energia, no entanto, 95 % do hidrogénio globalmente produzido deriva de fontes de energia fósseis. Embora o desafio de implementar uma maneira verde de produzir H_2 (verde) já tenha sido estabelecida, por eletrólise da água através do uso de eletrolisadores, esta abordagem é extremamente dependente de fontes externas de energia, tipicamente de painéis fotovoltaicos. As células fotoeletroquímicas (PEC) surgem como uma alternativa limpa e menos dispendiosa para a produção direta de H_2 utilizando apenas a luz solar e a água como fontes primárias. Resumidamente, uma célula PEC consiste em um semicondutor que, pela incidência da radiação solar, gera pares eletrão-lacuna que posteriormente participam na reação de separação da água, produzindo hidrogénio verde como combustível de energia. No entanto, o desafio de encontrar um semicondutor que cumpra todos os requisitos para um dispositivo PEC sustentável, tais como eficiência, baixo custo, estabilidade, não toxicidade e escalabilidade, ainda deixam esta técnica de produção de H_2 alvo de uma ampla e intensiva pesquisa e desenvolvimento.

Semicondutores de óxidos, como a hematite (α-Fe_2O_3) e o trióxido de tungsténio (WO_3), reuniram uma atenção crescente devido à sua abundância, baixo custo, não toxicidade e escalabilidade, tornando-os candidatos adequados à aplicações em células PEC. Em particular, a hematite é considerada um promissor candidato devido ao seu hiato de energia (2.2 eV), estabilidade a longo prazo e abundância natural, atingindo uma eficiência de solar para hidrogénio de 12.9 % em teoria.

Esta dissertação tem como foco o desenvolvimento e otimização de fotoânodos eficientes de semicondutores de óxidos baseados em hematite, combinando diferentes estratégias, como

a nanoestruturação e dopagem de elementos, para melhorar o desempenho fotoeletroquímico. Fotoânodos baseados na configuração 1D de nanofios (NWs) de hematite foram obtidos através de dois métodos hidrotérmicos. Foi estudado o efeito do agente oxidante, nitrato de sódio ($NaNO_3$) ou urea (CH_4N_2O), na síntese por método hidrotérmico. Além disso, foi realizada uma dopagem de vários metais nos nanofios de hematite. Foram testados os elementos atómicos Mn, Co e Ti, juntamente com um estudo do efeito da concentração de dopagem (C_{dopant}), relacionando com os valores de fotocorrente (*j*) obtidos pela célula PEC. Além das medidas da foto performance, foram realizadas técnicas de caracterização: morfológica, ótica e estruturais por meio de Difração de Raios-X (DRX) e Retrodispersão de Rutherford (RBS), sendo os seus resultados relacionados com as características físico-químicas subjacentes dos fotoânodos.

O agente de oxidação revelou ter um forte impacto na síntese dos NWs de hematite não dopados (C_{dopant} = 0 %) e dopados. A menor espessura, juntamente com uma maior condutividade sugerida pelo crescimento estrutural preferencial no plano (110) e maior difusão de Sn, foram considerados os principais fatores para a aprimorada resposta de *j* pelo método utilizando $NaNO_3$ como agente oxidante. A introdução do dopante de Mn não apresentou melhorias de *j* no método A ($NaNO_3$), enquanto no método B (urea), uma C_{dopant} de 7 % Mn obteve um aumento de 37 % na resposta de *j* em comparação com o respetivo fotoânodo de hematite não dopada. Este aumento foi associado a uma melhor qualidade cristalina e espessura mais fina. Além disso, as medidas de RBS sugeriram que o dopante de Mn promoveu uma maior difusão de Sn, que por estar associada a uma maior condutividade, leva ao melhor *j* obtido. Além do mais, observou-se um decréscimo do potencial de onset (V_{onset}), atingindo deslocamentos catódicos notáveis de 70 mV e 60 mV para o método A ($NaNO_3$) e método B (urea), respetivamente. Este resultado é bastante importante uma vez que tais valores de deslocamento não são normalmente encontrados na literatura, colocando este trabalho na frente de um resultado inédito. Por outro lado, a introdução do dopante Co para ambos os métodos, $NaNO_3$ e urea, não resultou em melhora de *j*; porém, mostrou-se benéfico para a diminuição do V_{onset}, atingindo desvios catódicos de 40 mV e 30 mV para 1 % no método A ($NaNO_3$) e 7 % no método B (urea), respetivamente. Finalmente, a dopagem de Ti no método A ($NaNO_3$) mostrou um C_{dopant} ótimo de 0.5 %, atingindo um $j \sim 0.9$ mA·cm^{-2} at 1.45 V_{RHE} (15.5 % de aumento de resposta em relação à hematite não dopada). Isto foi associado a um aumento na área de superfície efetiva e a uma aprimorada qualidade cristalina.

Além disso, foram desenvolvidas nanoplacas de WO_3 pelo método hidrotérmico. A Espectroscopia de Impedância Eletroquímica (EIS) foi realizada em nanoplacas de WO_3 na tentativa

de melhorar a compreensão sobre o efeito que o número de camadas tem no desempenho eletroquímico. As medidas de EIS corroboraram os resultados de *j-V*, com a amostra de 5 camadas a alcançar a menor resistência à transferência de carga entre a interface semicondutor/eletrólito e menor potencial de banda plana, vindo assim a reforçar que o ótimo fotoânodo de nanoplacas de WO_3 ótimo foi alcançado com 5 camadas.

Contents

List of Figures

Physical Constants

Speed of light	c	=	$2.997\,924\,58 \times 10^{8}$ m·s^{-1}
Planck's constant	h	=	$6.626\,070\,15 \times 10^{-34}$ J·s
Planck's constant	h	=	$4.135\,667\,696 \times 10^{-15}$ eV·s
Vacuum permeability	ϵ_0	=	$2.997\,924\,58 \times 10^{8}$ m·s^{-1}
Boltzmann constant	k_B	=	$1.380\,649 \times 10^{-23}$ J·K^{-1}
Boltzmann constant	k_B	=	$8.617\,333\,262 \times 10^{-5}$ eV·K^{-1}
Scherrer constant	K	=	0.94

Symbols

c	Speed of light	ms
e^-	Electron	
h^+	Hole	
j	Photocurrent density	$mA{\cdot}cm^{-2}$
ΔG^0	Gibbs Free Energy	kJ
ε	Microstrain	
f, υ	Frequency	Hz

Glossary

BSE	Backscattered electrons
CCS	Carbon Capture and Storage
C_B	Conduction Band
CE	Counter Electrode
D_{XRD}	Crystallite size
D	Diameter
E_g	Band gap
E	Electric Field
EIS	Electrochemical Impedance Spectroscopy
FTO	Fluorine-doped Tin Oxide
FWHM	Full Width at Half Maximum
GHG	Greenhouse Gas
H_2	Hydrogen
HER	Hydrogen Evolution Reaction
L	Thickness

NPs	Nanoparticles
NTs	Nanotubes
NWs	Nanowires
OER	Oxygen Evolution Reaction
PP	Parallel Beam
PEC	Photoelectrochemical
PV	Photovoltaic
P	Porosity
Q	Charge
RE	Reference Electrode
RHE	Reversible Hydrogen Electrode
RT	Room Temperature
RBS	Rutherford Backscattering Spectrometry
SEM	Scanning Electron Microscopy
SE	Scattered electrons
STH	Solar to Hydrogen
V	Potential
V_B	Valence Band
W	Depletion Layer

WE Working Electrode

XRD X-ray Diffraction

UV-Vis Ultraviolet-Visible

This dissertation is dedicated to my mother and my father.

Esta dissertação é dedicada à minha mãe e ao meu pai.

Introduction: Houston, we have a some problem(s) ...

Energy shapes our world. Since humans learned to control fire to power entire cities, life has completely changed. An undoubtful improvement has occurred, allowing humans to drive further beyond expected. Energy is everywhere in our lives, in the form of electricity used to power our alarms to wake us up, gadgets to spend time, machines to sustain all industrial processes and home appliances. An enormous effort has been put to supply most people with a cheap and stable energy chain, that most young people, nowadays, do not know what it is to experience a blackout or get stuck in an elevator. However, there are still 770 million people without access to electricity, mostly in Africa and Asia [1]. Figure 1 shows a clear relationship between the energy usage and wealth production, supporting the premise that energy propels an economic growth.

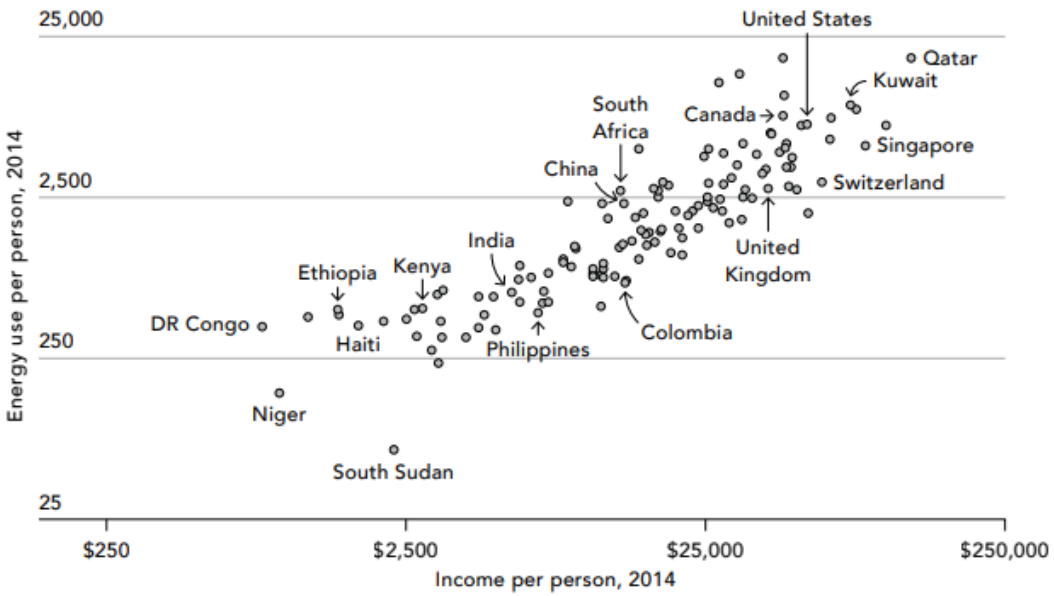

FIGURE 1: Comparison between the average income and energy consumption per person, in 2014. [Adapted from [2]]

Unfortunately, the current energy produced is far from being sustainable, both for the environment and ourselves. About 63 % of the electricity production in 2019 came from fossil fuels [3], accounting for 27 % of global greenhouse gas (GHG) emissions [2]. Combining electricity production with transportation and heat/cooling, the share of global emissions rises to 50 %, as can be seen in Figure 2. GHGs emissions lead to global warming as they trap the radiation emitted by the Earth inside our atmosphere, increasing the greenhouse effect. Even though this is an incredible process that allowed us to maintain a habitable temperature on Earth for all our existence, the increase in GHG emissions observed in the last 60 years provoked a disruption in this process, converting it into a heater process instead of a thermoregulation process. At this point, a temperature increase effect is inevitable. The question now is: How much will it be? And the answer is extremely important. An increase difference of just half degree Celsius (2.0 °C instead of 1.5 °C) leads to an additional 23 % of Earth's population being exposed to severe heatwaves at least once every five years; an 8, 16 and 18 % loss of vertebrates, plants and insects, respectively; a 99 % loss of coral reefs with a 3 million extinction of fishing shoals; among others [4].

Although multiple promises and agreements were made to keep this increase at 1.5 °C by 2100 [5], we continue off the pace to minimize it. As seen in Figure 3, keeping the current policies will lead to a temperature increase of 2.5 - 2.9 °C. Therefore, a remarkable and notorious development in technology and political change is mandatory to remain at the 1.5 °C target.

On the one hand, there is an urgency to stop GHGs emissions, keeping the 1.5 °C target alive. On the other, there is an inability to accomplish it, owing to the lack of green [1] and reliable energy sources available to sustain our current level of life and reach the population who does not

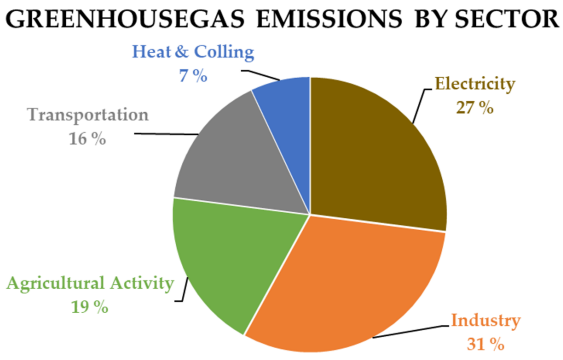

FIGURE 2: Global greenhouse gas emissions by sector. [Adapted from [2]]

[1] Whenever a technology is mention to be green, it refers to having a net-zero GHGs emissions.

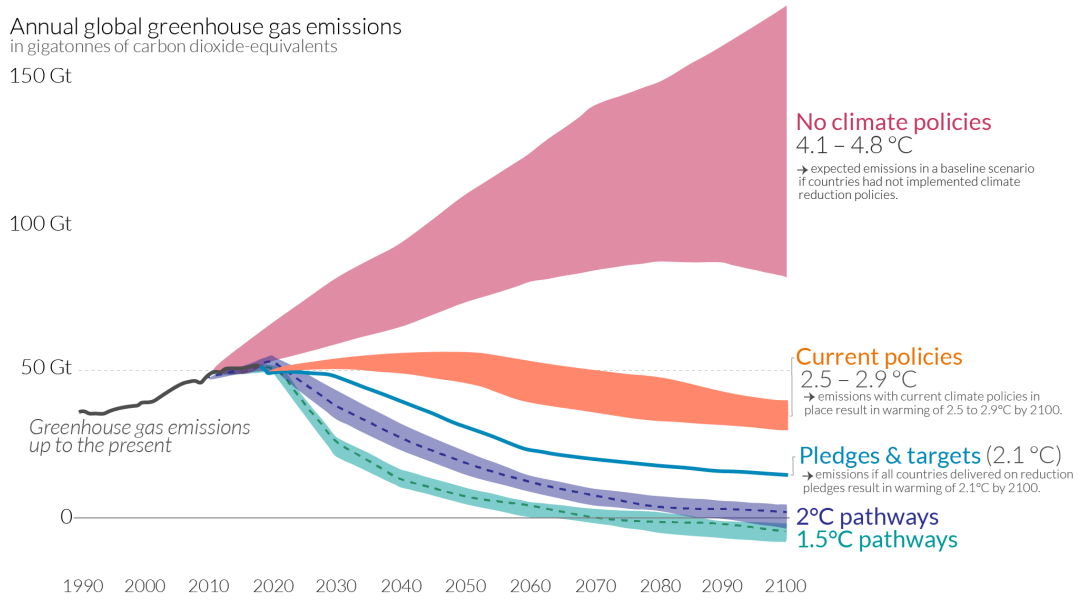

FIGURE 3: Greenhouse gas annual emissions from 1990 to 2100, according to different scenarios. [Adapted from [6]]

have access to electricity. We cannot simply shut down every fossil fuel source of energy production without having a cheap and reliable alternative, as it will lead to economic regressions and an unimaginable number of human deaths. We must not be blind! A global agreement plan must be done with clear measures and commitment, outlining a path where a net-zero economy is reached with security and stability through cooperation between all the countries in the world.

As always, it is easier said than done. A singular clean, cheap, and worldly permanently available energy source does not exist, causing the incorporation of green alternatives an expensive process with political constraints in most cases. Nevertheless, I believe in Human perseverance to find an array of clean, stable and low-cost alternatives to be strategically applied to solve our problems. If we can develop energy sources which are sustainable, clean and cheaper than fossil fuels, both developed and developing countries will feel compelled to incorporate them. Of course, these technologies are not yet available, as some await further development and others to be discovered. While the search and development continue, other alternatives, despite not being perfect, must compensate and lower fossil fuel consumption. Although hydro technology is close to reaching maximum efficiency, solar and wind energies have been growing. The importance of these green energies can not be underestimated, as demonstrated, for instance, by (solar and wind energies) preventing the European Union (EU) from importing 70 billion cubic meters of Russian natural gas during the war in Ukraine [7].

Another renewable energy source which has been gathering attention is Hydrogen (H_2). The lightest element molecule on Earth can act as a cheap, sustainable and permanent energy source (24 hours a day, all year round). Additionally, it is stable, presents minimal self-discharge and has a high volume and mass energy density (> 1 kWh/L). On the other hand, it is a gas (it can be liquefied, but it is not profitable) making it difficult to handle, store and transport, and displays a low round-trip-efficiency of ca. 35 %. Although not the ideal energy vector, hydrogen will play an important role in the electricity mix production and the transportation industry, with fuel cells vehicles and the synthesis of synthetic fuels, in the following years.

This work explores one of the available methods for green hydrogen production, namely by using photoelectrochemical (PEC) cells to perform solar water splitting. Firstly, we inspect hydrogen production methods, followed by a contextualization of photoelectrochemical (PEC) cells with the materials and strategies applied to improve them (in Chapter 1). Chapter 2 describes the experimental methods and materials for the synthesized samples, along with the characterization techniques performed in this work. Chapters 3 to 5 report the research done with hematite, a promising semiconductor for PEC cells. Moreover, the analysis of electrochemical impedance spectroscopy measures of tungsten trioxide multilayers PEC cells is presented in Chapter 6. Finally, the overall conclusions and ongoing/future work are discussed in Chapter 7.

The work was -, is and will continue to be - motivated by the faith in achieving an energy economy with net-zero emissions, capable of providing accessible, low-cost and sustainable energy all across the planet, assuring the continuous development of Humanity in communion with nature.

Chapter 1

Hydrogen: A novel trend in fuel generation

Hydrogen is the lightest and most abundant element known in the universe. On Earth, hydrogen generally exists in molecular forms, like water and organic compounds, or as a gas of diatomic molecules with a covalent bond between two hydrogen atoms, forming molecular hydrogen, H_2. Since hydrogen rarely appears in nature as a gas, it has to be separated from other molecules.

Hydrogen was firstly observed in 1520 by Theophrastus von Hohenheim, who documented an ascending gas through the dissolution of metals in sulfuric acid. Two centuries later, Henry Cavendish identified a chemical element discovered by Robert Boyle when reacting iron with dilute acid. However, the current name was only given in 1783 by Antoine Lavoisier. The first report of water electrolysis came in 1789 with Rudolph Deiman and Adriaan Paets van Troostwijk using an electrostatic machine on gold electrodes in a Leyden jar filled with water [8]. Years later, a voltaic pile was used to decompose water in hydrogen and oxygen by William Nicholson and Sir Anthony Carlisle. [9, 10]

Historically, hydrogen has received many applications: such as the Hindenburg transatlantic zeppelin, which completed ten successful flights, but went up in flames in 1937; the hydrogen bomb, only tested so far; hydrogen-powered vehicles with an internal combustion engine using hydrogen as fuel ("Erren engine"); and fuel cells used in space missions. Nowadays, hydrogen is mainly used in industrial processes, like the synthesis of ammonia for fertilizer production and petroleum refining to remove sulphur from fuels and to upgrade heavy oil fractions [9]. Recently, fuel cell vehicles fed by hydrogen have been receiving attention, together

Storage Method	**Energy Volume Density [kWh · L^{-1}]**	**Mass Density [g · L^{-1}]**
STP conditions	2.98×10^{-3}	0.089
Liquefied 20 K	2.3	70
Compressed 350 bar	640×10^{-3}	19
Compressed 700 bar	1.3	39
Gasoline	9.3	0.78

TABLE 1.1: Comparison hydrogen between storage methods, with gasoline as a fossil fuel comparison [13, 14].

with synthetic fuels (e-fuels), produced by combining hydrogen, CO_2 and electricity, as the case for e-methanol [11].

Motivated by public pressure regarding climate change, new energy alternative sources have been searched. Hydrogen began to receive a powerful lobby in the energy industry, owing to a feasible production, storage and electric energy generation without greenhouse gases (GHGs) emissions. Therefore, it is a constant energy source (24 hours a day, all year round), with the possibility of being transported and stored everywhere.

However, hydrogen usage as an energy source is not all a fairy tale. As a result of being the smallest and lightest element on Earth, storage and transportation present a real challenge, as the volume density is extremely low, which requires the gas to be compressed to 700 bar to have an energy volume density compared with other fuels (see Table 1.1). Liquefying offers a higher energy volume density, though it presents a loss of 2-3 % of volume per day suffered by hydrogen evaporation (the liquefaction process requires the cryostat to be open); not to mention liquefy and keeping the cryogenic temperature consumes a high amount of energy. Other solutions to the transportation problem consist of using hydrides, which are hydrogenated inorganic compounds that can store hydrogen; and bending hydrogen in the existing natural gas pipelines (H_2 - CH_4), as it was already tested in the United Kingdom [12].

In addition, hydrogen must present a high round-trip efficiency to compensate for the low energy volume density. Even though it is currently only at 35 % [15], the last few years have been full of efforts in terms of scientific research and technology innovation, with notorious research and development placed into advanced electrolyzers and new technologies to produce sustainable hydrogen. In detail, one of the most innovative and advanced ways to obtain hydrogen is from photoelectrochemical (PEC) cells, as will be presented in this dissertation. But first, an understanding of how hydrogen is currently produced and the alternative routes available is broken down in the following section.

1.1 Hydrogen Production

Hydrogen can be produced by different methods, namely by steam-reforming methane, methane pyrolysis and water electrolysis. To simplify, a colour scheme has been assigned for each production method, as shown in Figure 1.1.

Nowadays, about 95 % of hydrogen produced derives from fossil fuels (the so-called grey hydrogen), mainly by steam-reforming methane (SMR) or coal gasification, contributing to an estimated 21.9 metric tons of GHGs emissions [17]. With the aim of reducing carbon emissions, these methods can combine with carbon capture and storage (CCS) devices to diminish CO_2 emissions (blue hydrogen). However, grey and blue hydrogen continue to rely on finite resources, which are highly exposed to fossil fuel price fluctuations and dependent on the expensive prices of CCS devices.

Turquoise and green hydrogen are the only approaches with zero GHGs emissions. Turquoise hydrogen is produced by methane pyrolysis (or decomposition). Contrary to SMR, pyrolysis consists on the thermal decomposition of methane in hydrogen and solid carbon black, as witnessed in Equation 1.1. Hydrogen can then be stored or transported to generate electricity, while carbon black integrates the existing market, providing an additional profit. However, the high temperatures (900 °C [18] and 1000 °C [19]) necessary to conduct the decomposition reaction associated with expensive costs remain significant improvement areas regarding this technique.

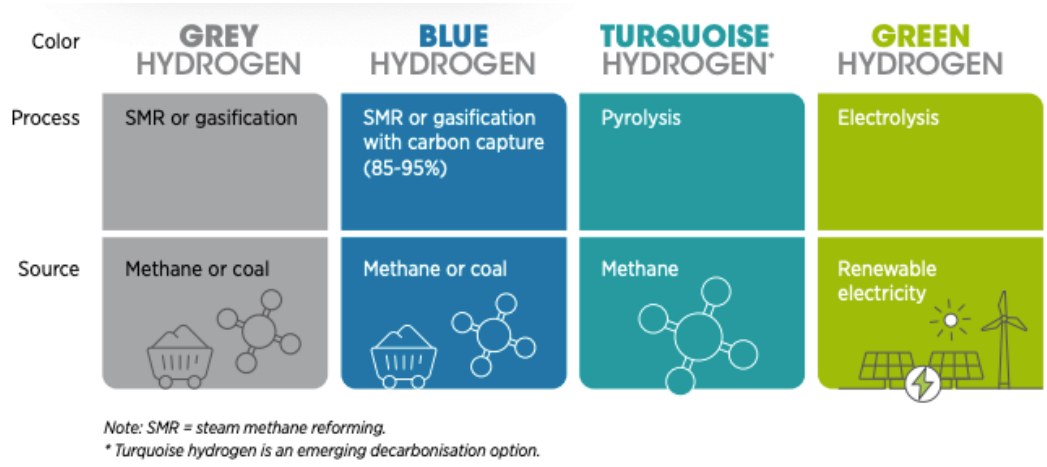

FIGURE 1.1: Main shades of hydrogen according to the production method. [Extracted from [16]]

$$CH_4\ (g)\ \rightarrow\ C\ (s) + 2H_2\ (g), \quad \Delta H^0_{298K} = 74.8 kJ \cdot mol^{-1} \tag{1.1}$$

Finally, green hydrogen consists on the electrolysis of water (H_2O). Water, which accounts for 71 % of the Earths surface, is composed of two hydrogen atoms bonded to an oxygen atom, making it the most appealing molecule to extract hydrogen. Equation 1.2 represents the water electrolysis reaction, where completely sustainable hydrogen and oxygen are produced. Energy needs to be provided to separate water molecules, making this an endothermic reaction. Therefore, a bias potential from renewable sources (e.g. wind, solar, etc.) must be supplied for the reaction to occur. Water splitting is usually carried out by electrolysers using energy from renewable sources, like photovoltaic (PV) panels (this strategy is named PV-E). Besides the required energy bias, PV-E modules employ an extensive number of materials and space with long wiring cables to connect the PV panels to the electrolysers.

One promising technology is photoelectrochemical (PEC) cells, which allow the on-site production of green hydrogen by solar water splitting in a single device. The less material and wiring required make PEC cells potentially cheaper, with the ability to attain higher potential efficiencies as electrons travel a shorter distance, avoiding resistance in wiring and resistive losses [20].

$$H_2O\ (l)\ \rightarrow\ H_2\ (g) + ½O_2\ (g), \quad \Delta H^0_{298K} = 237.2 kJ \cdot mol^{-1} \tag{1.2}$$

A detailed look at the working principles of PEC cells, materials and strategies to improve their performance is examined in the remainder of the chapter.

1.2 Photoelectrochemical Cells

Initially introduced in 1972 by Fujishima and Honda [21], photoelectrochemical (PEC) cells have been under constant development, especially in recent years, where nanotechnology has allowed substantial improvements in the efficiency of these cells.

A PEC cell (illustrated in Figure 1.2) consists on a semiconductor[1] (the working electrode) and a counter-electrode (usually platinum), both immersed in water. The incidence of solar radiation with energy higher than the band gap of the semiconductor generates electron-hole

[1] A semiconductor is a material in which the conduction and valence bands are separated by a small energy gap, denominated band gap (E_g). By applying an energy equal or higher to the band gap ($E > E_g$), the material generates electron-hole pairs ($e^- - h^+$), which turns the material conductive.

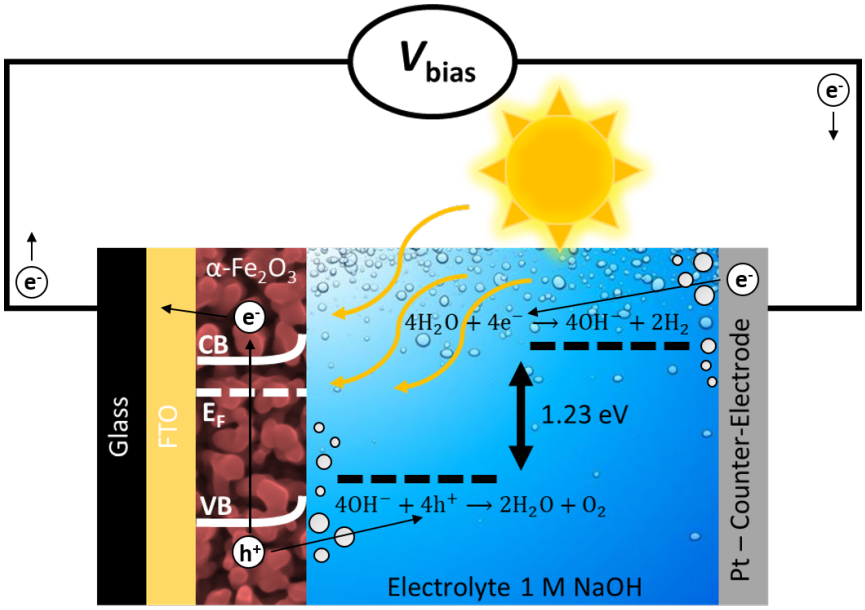

FIGURE 1.2: Schematic of a PEC cell for solar water splitting with hematite as the semiconductor (working electrode). Solar light generates electron-hole charge carriers pairs on the semiconductor; holes facilitate the oxidation reaction that produces oxygen on the working electrode, while the free electrons flow to the counter-electrode to promote the reduction reaction that generates hydrogen.

pairs ($e^- - h^+$) that will participate in water-splitting reactions. Electrons are collected by a conductive substrate (fluorine-doped tin oxide - FTO in the Figure 1.2) and directed, through an external circuit, to the counter-electrode of platinum, where they will participate in the reduction reaction for the hydrogen evolution reaction (HER). On the other hand, holes are transferred to the water-based electrolyte in order to participate in the oxidation reaction of the oxygen evolution reaction (OER). The electrochemical reactions at each electrode, working and counter electrodes, are described as follows:

- Working electrode: composed by the semiconductor material, where the oxidation reaction occurs:

$$\text{Basic media: } 4OH^- + 4h^+ \longrightarrow 2H_2O + O_2, \qquad E^\circ_{O_2/OH^-} = -0.401\,V \tag{1.3}$$

$$\text{Acid media: } H_2O + 2h^+ \longrightarrow 2H^+ + {}^1/_2O_2, \qquad E^\circ_{H_2O/H_2} = 1.23\,V \tag{1.4}$$

- Counter electrode: composed by a metal resistant to corrosion (e.g. Pt), where the reduction reaction occurs:

$$\text{Basic media: } \quad 4H_2O + 4e^- \longrightarrow 2H_2 + 4OH^-, \qquad E^\circ_{H_2O/H_2} = -0.828\,V \tag{1.5}$$

$$\text{Acid media: } 2H^+ + 2e^- \longrightarrow H_2, \qquad E^\circ_{H_2O/H_2} = 0.0\,V \tag{1.6}$$

From these equations, we conclude that, under standard conditions, the water electrolysis is not spontaneous, requiring a minimum potential of 1.23 V at 25 °C for the reaction to occur. The need for a bias potential represents one of the drawbacks of PEC cells, as it leaves them dependent on other energy sources to produce hydrogen. Coupling low-cost PV devices with PEC cells (PEC/PV tandem cells) offer the external bias potential needed for hydrogen production to occur unassisted [22–25]. Additional challenges are associated with poor semiconductor efficiencies, lack of long-term stability, optical losses, mass transport limitations and scalability of cells, which are overcome with specific materials and applied strategies, as discussed in Sections 1.2.1 and 1.3.

1.2.1 Sustainable Photoanode Materials

Photoanode is one of the principal factors in the performance of photoelectrochemical cells, with some requirements needed to be fulfilled, as shown in Figure 1.3. As mentioned in the previous section, the photoanode material must be a semiconductor for the cell to be photoactive. Secondly, the semiconductor band gap should cover the HER and OER potentials, having at least the minimum potential of 1.23 V plus the activation energy needed for the reaction to initiate (low kinetic overpotentials). An ideal band gap (of ca. 1.8 eV) lowers the dependence on an external bias potential, contributing to a more efficient cell. Furthermore, semiconductor materials should possess a strong absorption of visible light since visible light has the best availability/energetic relation of all sunlight. Chemical stability, low-cost, non-toxicity and scalability represent additional requirements for PEC cells to enter suitably in the energy market. Another factor to consider is the synthesis method of the photoanode materials. These synthesis methods must be equally efficient, simple and scalable to not compromise the low-cost of materials.

Finding a single material to fulfil all requirements is extremely difficult, being the search for a unique material that obeys all requirements the holy grail of this research area. In the meanwhile, the available materials are engineered to extract the optimum possible performance. For instance, an ideal semiconductor material must simultaneously cover the band edges of HER and OER redox potentials, while also absorbing a significant share of visible light. From Figure 1.4 we conclude that there is no material capable of simultaneously fulfilling these two requirements. In these situations, studies need to be conducted to determine a optimum agreement between factors that improves the cell performance.

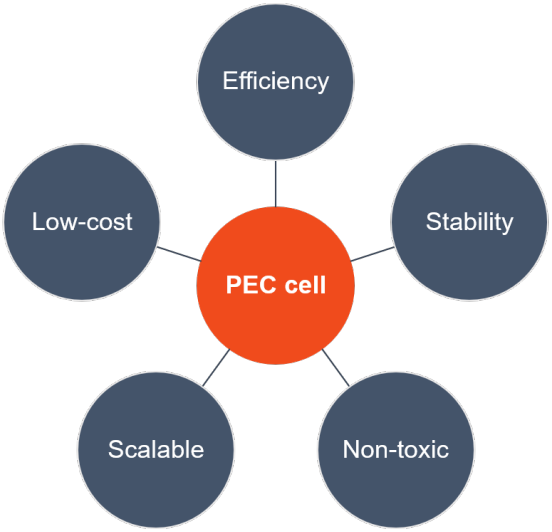

FIGURE 1.3: Properties for a sustainable and efficient photoanode material. [Adapted from [26]]

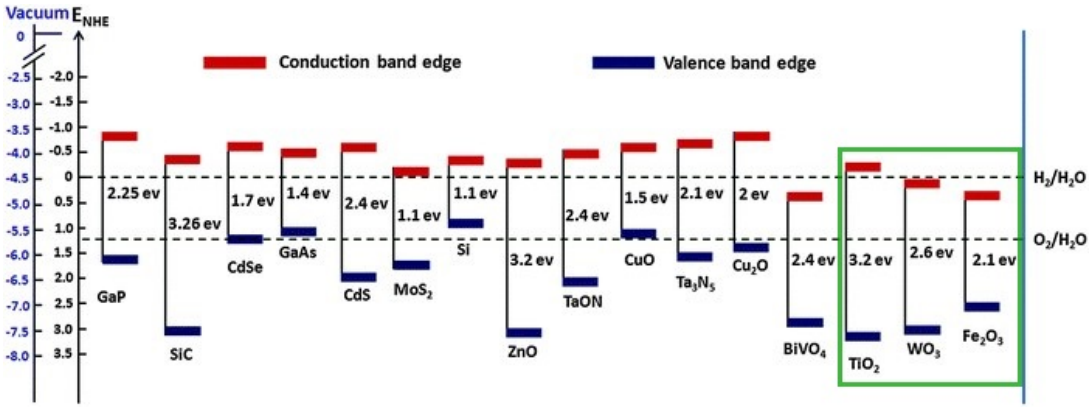

FIGURE 1.4: Band gap positions for several semiconductor materials in contact with the aqueous electrolyte at pH = 0 relative to normal hydrogen electrode (NHE) and the vacuum level. The HER (upper dash line) and OER (lower dash line) redox potentials are presented for comparison. [Extracted from [27]]

Oxide semiconductors, namely, hematite (α-Fe_2O_3) [28–30], tungsten trioxide (WO_3) [31–33] and titanium dioxide (TiO_2) [34–36] have been going through extensive study due to their abundance, non-toxicity and scalability. Advances in the performance of these semiconductors were made, with an inspiring number of methods and strategies emerging. Yet, despite the successes achieved to date, there is not still a single system capable of offering all requirements, such as high solar-to-hydrogen (STH) efficiency, affordability, and scalability, with high performance and long-term stability.

In this thesis, we focus on the development of photoanodes based on two oxide semiconductors, α-Fe_2O_3 and WO_3, employing strategies like nanostructuring and doping with scalable and low-cost synthesis techniques, to improve the performance of PEC cells. The following

sections (Sections 1.2.1.1 and 1.2.1.2) introduce the physical and electrochemical properties of the developed semiconductors, giving particular attention to hematite due to the outstanding properties that cause it to have one of the highest theoretical photoconversion efficiency.

1.2.1.1 Hematite

Hematite (α-Fe_2O_3) is the most stable form of iron oxide under ambient conditions, making it the most abundant form of crystalline iron oxide. In the past few years, hematite has been gaining significant research attention owing to a short optical band gap (2.0 - 2.2 eV, which provides an ampler visible light absorption), pre-eminent chemical stability, low-cost and natural abundance, which enable a predicted solar-to-hydrogen (STH) efficiency of 12.9 % in theory [37]. However, the current reported STH values are significantly lower than the theoretical, mainly due to several material limitations, such as low conductivity ($\sim 10^{-2}$ cm^2 V^{-1} s^{-1}) [38] and high recombination rate of electron-hole pairs caused by a short hole diffusion length ($\sim$ 2 e 4 nm) [39] and short lifetime of photogenerated charge carriers (< 10 ps) [40].

A deeper discussion of hematite properties is taken to understand the advantages and challenges hematite faces in the application for PEC cells. The following paragraphs discuss the crystal structure of hematite and its optical, electronic and photoelectrochemical properties.

Crystal Structure Iron oxide exists as amorphous Fe_2O_3 and as four polymorphs (α, β, γ, and ϵ). α-Fe_2O_3, also called hematite, is the most common Fe_2O_3 polymorph existing in nature. Iron and oxygen atoms crystallise in a rhombohedral centered hexagonal structure of the corundum type (α-Fe_2O_3), with trigonal-hexagonal scalenohedral symmetry in the space group R-3c, lattice parameters a = 5.0356 Å, c = 13.7489 Å, and six formula units per unit cell. The O^{2-} anions arrange in a hexagonal close-packed lattice along the [001] direction, with the Fe^{3+} cations occupying two-thirds of the octahedral interstices in the (001) basal planes and the tetrahedral sites remaining unoccupied [41–43]. Figure 1.5 shows the pairs of FeO_6 octahedra that share edges inside the basal (001) plane and one face with an octahedron in an adjacent plane in the [001] c-axis. This face-sharing results in repulsion between Fe atoms along the direction normal to the [001], causing the cations to shift closer to the unshared faces, which causes a trigonal distortion from the ideal packing [42]. The crystal orientation of the nanostructures is also a determinant factor in the performance of PEC cells, as structures having multiple orientations yield less performance compared to structures with a preferential orientation [44].

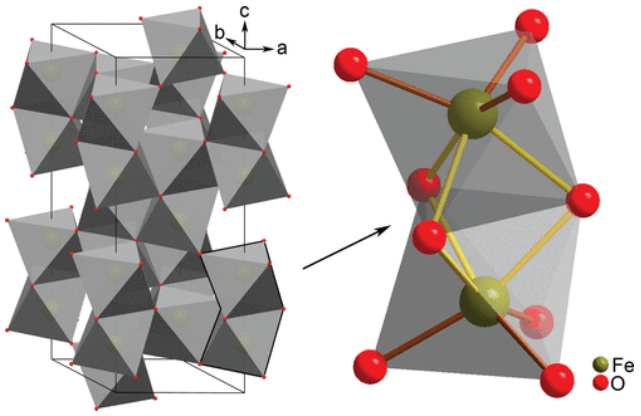

FIGURE 1.5: Schematic illustration of the hematite unit cell with octahedral face-sharing (left). The detailed view (right) represents one face-sharing dimer (Fe_2O_9), with longer (yellow) and shorter (brown) Fe-O bonds resulting from the repulsion between the Fe^{3+} cations. [Extracted from [45]]

Optical Properties The optical absorption of hematite begins in the near-infrared spectral region, formed by $d-d$ transition states between energy levels for the electron configuration d^5 of the Fe^{3+} ion, which are split by an intrinsic crystal field [46]. Hematite presents a band gap energy between 2.0 to 2.2 eV (corresponding to λ = 620 to 560 nm), meaning only radiation with the same or higher energy than the band gap is absorbed. The red-brown characteristic colour of hematite is given by the transmission of orange to infrared photons and the strong absorption of yellow to ultraviolet radiation in the visible spectrum.

Assuming that the energy bands are parabolic with respect to the crystal momentum, the Tauc analysis of the absorption coefficient indicates that the band gap is indirect, i.e. phonon participation is necessary for the photoexcitation process. As a consequence, the absorption length (α^{-1}) of hematite is relatively long, e.g. α^{-1} = 118 nm at a photon wavelength of 550 nm [47].

In terms of PEC performance, the band edge positions are of extreme importance. UV photoelectron spectroscopy indicates that the bottom of the conduction band lies 0.1 – 0.2 eV lower than the HER potential, as can be observed in Figure 1.6 [48, 49]. Therefore, even for heavily n-doped hematite where the quasi-Fermi for electrons (E_{Fn}) lies just below the bottom of the conduction band, complete water splitting using hematite as a single photoabsorber cannot take place without an external bias. The valence band lies about 0.7 eV below the OER potential. Figure 1.6 displays the band gap position of hematite compared to an ideal photocatalyst for PEC cells.

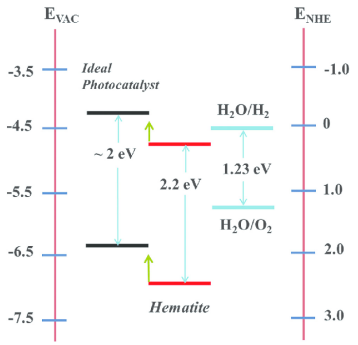

FIGURE 1.6: Band gap positioning of hematite compared with an ideal photoanode. [Extracted from [50]]

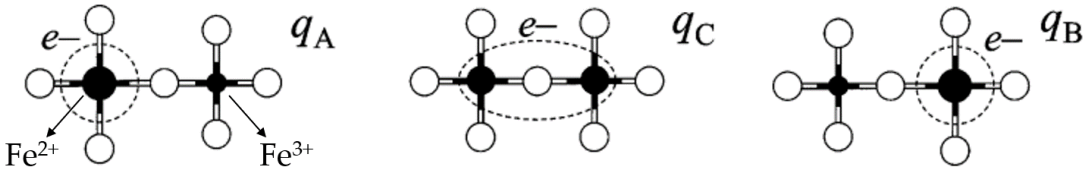

FIGURE 1.7: Schematic of the $Fe^{2+}/^{3+}$ valence alternation in the electron transfer reaction between nearest-neighbour iron atoms. Fe^{2+} ionic radius is bigger than Fe^{3+}. The important nuclear configurations concerting electron transfer are those of the reactants, q_A, and products, q_B, and the crossing-point configuration, q_C. [Adapted from [51]]

Electronic Properties In terms of electronic properties, hematite is described as a Mott insulator where charge transport follows the adiabatic small polaron model, including the effect of the size difference between Fe^{2+} and Fe^{3+} ions and the associated lattice distortion. The introduction of an extra electron provokes a $Fe^{2+}/^{3+}$ valence alternation in the electron transfer reaction between nearest-neighbour iron atoms. As a result, the ionic radius of the iron site increases and the surrounding lattice polarizes, which originates a distortion that traps the electron (see Figure 1.7). The distortion of the surroundings moves with the migrating charge when an electron or a hole migrates to an adjacent iron atom, thus conducting electricity.

Hematite is considered a weak n-type semiconductor, with electrons (majority charge carriers) being the principal responsible for α-Fe_2O_3 conductivity. Since the majority charge carriers (photogenerated electrons) decay rapidly from the conduction band due to either the intrinsic electronic structure of the material or a high density of trapping states, the light-generated charge carriers in α-Fe_2O_3 have a short lifetime, leading to poor conductivity [43, 52].

Photoelectrochemical Properties Photocurrent density-voltage (j-V) curves are the main evaluation of a photoanode of water splitting. Figure 1.8 shows a typical j-V curve, where the potential (V) is applied while the photocurrent density is measured. Two main parameters are taken from these measures: the plateau current (j), which is the highest value of photocurrent

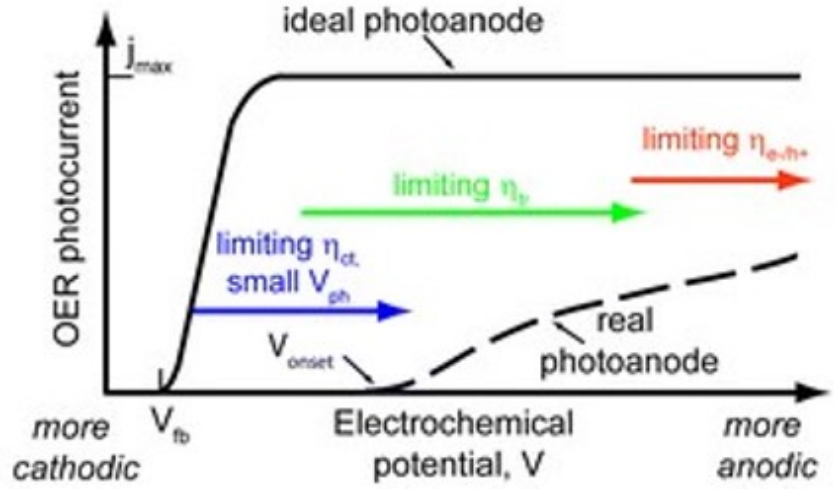

FIGURE 1.8: Photoelectrochemical curves of an ideal photoanode compared to the state-of-the-art of hematite.

at a given potential (usually 1.23 V_{RHE} or 1.45 V_{RHE}), and the onset potential (V_{onset}), given by the minimum bias potential applied for the OER reaction to occur (Equation 1.4). The plateau current is proportionally related to the hydrogen rate production, i.e. as the photocurrent increases, more hydrogen is produced. The ideal hematite photoanode presents a plateau current of 12.6 mA·cm^{-2} (under AM 1.5 G 100 mW/cm^2 simulated sunlight conditions), which corresponds to an incident photon to current efficiency (IPCE) of a unity. Additionally, the plateau current is reached within 0.1 V from the onset potential that equals the flat band potential (V_{fb})[1], with a potential ca. + 0.4 V versus reversible hydrogen electrode (RHE) [53]. However, the current state-of-the-art presents a V_{onset} of 1.0 – 1.1 V_{RHE}, taking up to 0.4 – 0.5 V to reach the maximum photocurrent value of 4 mA·cm^{-2} at 1.5 V_{RHE} [54].

The photoelectrochemical performance of the ideal and real hematite photoanode can be compared in Figure 1.8. From the *j*-*V* curve behaviour, three regions are defined according to their principal limiting factor of performance [48]. For $V_{fb} < V < V_{onset}$, holes transferred to the electrolyte efficiency (η_{ct}) and the small photovoltage (V_{ph}) are the bottlenecks. For V moderately more anodic than V_{onset}, the fraction of photogenerated charges reaching the respective solid/liquid interface (η_{tr}) limits the reaction. Finally, for V highly more anodic than V_{onset}, the performance is only limited by the efficiency of the photons absorbed (η_{e^-/h^+}).

These limiting factors are overcome by strategies like nanostructuring, doping and the use of co-catalysts, which enhance the photocurrent to its maximum photoconversion efficiency

[1]The flat band potential defines the potential at which there is no depletion layer at the semiconductor/electrolyte interface. In a simplified manner, this is the theoretical potential needed to be applied to initiate the water electrolysis.

(Section 1.3 will address these strategies).

1.2.1.2 Tungsten Trioxide

Afterwards attracting much interest as an electrochromic material in "smart window" applications [55, 56], gas/humidity sensing and x-ray shielding [55], tungsten trioxide (WO_3) was firstly reported as a potential efficient photoanode for water splitting applications by Hodes et al. in 1976 [57]. Since then, WO_3 has been through a detailed study to improve its PEC performance through innovative morphologies and strategies [58, 59].

Similarly to hematite, WO_3 is a low-cost material widely available, with high stability against photocorrosion and easily synthesized through user-friendly and scalable methods, such as hydrothermal or electrochemical anodization [31–33]. On the contrary, tungsten trioxide presents high conductivity (6.5 $cm^2 \cdot V^{-1} \cdot s^{-1}$), higher carrier lifetime (1-9 ns) and higher carrier concentration (5×10^{19} cm^{-3}), long hole ($\sim$ 150 nm) and electron ($\sim$ 500 nm) diffusion lengths, favourable energy band edge for oxygen evolution, high stability in acidic aqueous solutions and presents isotropic electronic properties [58, 59]. However, the large band gap of 2.6 – 2.8 eV implies a poor absorption of 12 % of the solar spectrum, with low visible light absorption. Combined with kinetic losses, WO_3 presents a maximum solar-to-hydrogen conversion efficiency of just 4.8 % (under standard AM 1.5 solar illumination)[1] [37, 59, 60].

Crystal Structure Tungsten Trioxide exists in six stable phases: tetragonal (α-WO_3), orthorhombic (β-WO_3), monoclinic I (γ-WO_3), triclinic (δ-WO_3), monoclinic II (ε-WO_3) and cubic WO_3 (not commonly observed). All the crystallographic phases arise from deviations from the ideal ABO3 perovskite structure of WO_3, which bases on the three-dimensional networks of corner-sharing WO_6 octahedra, mainly due to distortions of antiferroelectric displacements (Figure 1.9) [58]. In the bulk form, WO_3 shows phase transitions during annealing or cooling in the following sequence: monoclinic II (ε-WO_3 for < -43 °C), triclinic (δ-WO_3 from -43 °C to 17 °C), monoclinic I (γ-WO_3 from 17 °C to 330 °C), orthorhombic (β-WO_3 from 330 °C to 740 °C) and tetragonal (α-WO_3 for > 740 °C) [58, 61]. Additionally, orthorhombic [61] and hexagonal [62] phases (named orth-WO_3 and hex-WO_3, respectively) were observed. Among all crystallographic phases, the monoclinic I (γ-WO_3) has been reported as the beneficial phase for water splitting applications, with specified preferential orientations leading to PEC improvements [26].

[1] Remember that hematite has a theoretical STH efficiency of 12.9. %.

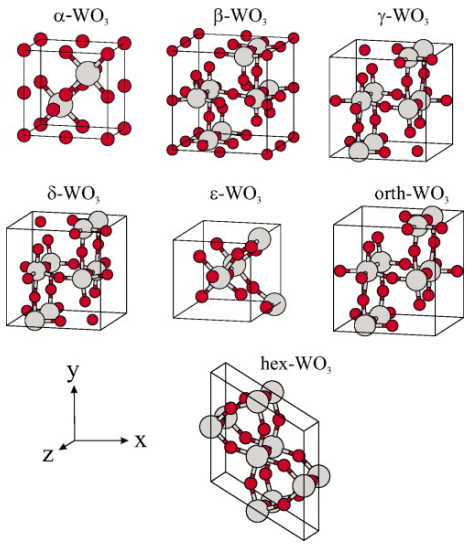

FIGURE 1.9: Unit cells of different phases of WO_3, with tungsten atoms (larger gray balls) and oxygen atoms (smaller red balls). [Extracted from [63]]

Optical Properties The electronic band gap of nanostructured WO_3 is blue-shifted compared to its bulk form, with a smaller band gap of 2.5 – 2.6 eV for crystalline WO_3 as opposed to the 3.25 eV band gap for amorphous WO_3 [64]. Consequently, stoichiometric WO_3 is essentially transparent to most visible light, with a yellow colour for smaller band gap samples.

In the same way as hematite, tungsten trioxide is an n-type semiconductor with a suitable valence band for water oxidation (lower than the OER potential) and a conduction band inconvenient for water reduction (lower than HER potential). Therefore, unassisted water splitting using WO_3 as a single photoabsorber cannot take place without an external bias.

Electronic Properties Tungsten trioxide electrical conduction relies on a significant concentration of the majority charge carriers (free electrons) being present in the conduction band. The majority charge carrier density in such materials is mainly determined by the number of stoichiometric defects, like oxygen vacancies [65]. Research has found that the increased volume of grain boundaries, which contributes to more trapping and scattering of free charge carriers, decreased the conductivity of WO_3 nanoparticles [58]. Additionally, the impact of lattice strain and crystal distortions in charge transport also contributes to a decrease in conductivity. On the other hand, high conductivity values were attained by enhancing the crystalline nature and orientation of the nanostructure through a temperature increase [66]. Overall, the electronic properties of WO_3 are strongly dependent on the synthesis techniques and the growth conditions.

Photoelectrochemical Properties WO_3 exhibits a high resistance against photocorrosion and good chemical stability in acidic aqueous solutions (pH < 4) under solar illumination. In terms of performance, although the high conductivity, carrier lifetime and carrier concentration enabled a much higher STH conversion, the low absorption of solar light and large band gap limit the PEC performance to a theoretical maximum solar-to-hydrogen efficiency of just 4.8 %. Nonetheless, research has consistently found new ways to overcome these limitations, optimizing the performance of tungsten trioxide to integrate further cell arrangements of higher efficiency, like heterojunctions [67, 68] and PEC/PV tandem cells [23].

1.3 Strategies to Improve Photoelectrochemical Cells

Several strategies have been developed to overcome the weaknesses of the semiconductor materials used as photoanodes. Among them, the design of nanostructures, elemental doping, heterojunctions and modifications of the surface/interface have been the ones, by far, most widely addressed (Figure 1.10).

Nanostructured photoanodes provide an efficient collection of photogenerated charges by improving the surface area of the photoanode/electrolyte interface. Moreover, coupling different semiconductors materials in layers, so-called heterojunctions, enhance charge separation of electron-hole pairs. Typically, photogenerated holes in the internal layer move to the valence band of the outer layer, whereas electrons generated in the external layer fall to the conduction band of the inner layer, facilitating electron collection by the FTO conductive substrate.

Doping intrinsic semiconductors with other elements has been widely used to promote charge transfer, as it enables the presence of additional free electrons in the case of n-type doping or additional vacancies in the case of p-type doping. Finally, surface/interface modifications like surface passivation reduce the electron-hole pair recombination by improving the electron collection by the substrate, while surface co-catalysts increase the water oxidation kinetics, which dispatches holes and reduces the recombination of electron-hole pairs. A scheme with these strategies and their beneficial improvements is illustrated in Figure 1.10.

In this work, nanostructuring was applied to synthesize hematite nanowires (NWs) that improve charge collection. Using a hydrothermal method, we produced non-toxic, stable and low-cost photoanodes through a user-friendly, low-cost and scalable technique. To improve the photoanode performance, elemental doping with Sn, Mn, Co and Ti promoted the charge

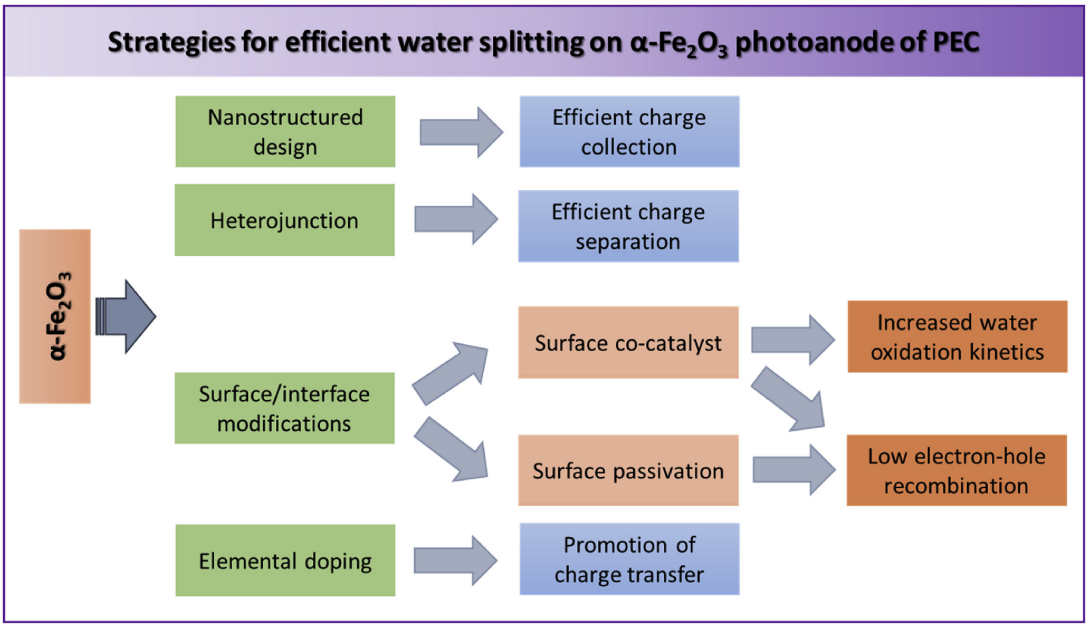

FIGURE 1.10: Strategies reported to improve semiconductors photoanodes for PEC cells. [Extracted from [30]]

transfer, leading to a more efficient PEC cell. Furthermore, the increase of water oxidation kinetics through the deposition of co-catalysts is being exploited as ongoing work, taking us closer to fulfilling all requirements of a sustainable PEC cell.

1.3.1 Nanostructuring

As previously discussed (Section 1.2.1.1), the photoelectrochemical performance of hematite photoanodes is heavily limited by the high recombination of electron-hole pairs derived from the short hole diffusion length and lifetime of photogenerated charge carriers.

Nanostructuring improves charge collection by enabling cleaner and shorter paths for electrons to reach the conductive substrate and for holes to reach the photoanode/electrolyte interface. The synthesis of different morphologies is obtained through both bottom-up or top-down approaches, composed of synthesis techniques: e.g. anodization of Fe foils [69], electrochemical routes [70, 71], chemical vapor deposition (CVD) [53], spray pyrolysis [72, 73] and hydrothermal [74–76]. Regarding hematite photoanodes, Figure 1.11 presents numerous morphologies developed to exploit the nanostructuring advantages. Among them, nanowires (nanorods) [70, 74, 75, 77, 78], nanotubes [69, 79, 80], cauliflower-like structure [53, 76, 81], nanoflakes [71, 82] and nanoparticles [72, 73, 80] have shown remarkable improvements compared to bulk films.

The highlight of hematite nanostructures falls on Tilley et al. with their cauliflower-like hematite photoanode synthesized by atmospheric pressure chemical vapour deposition, which

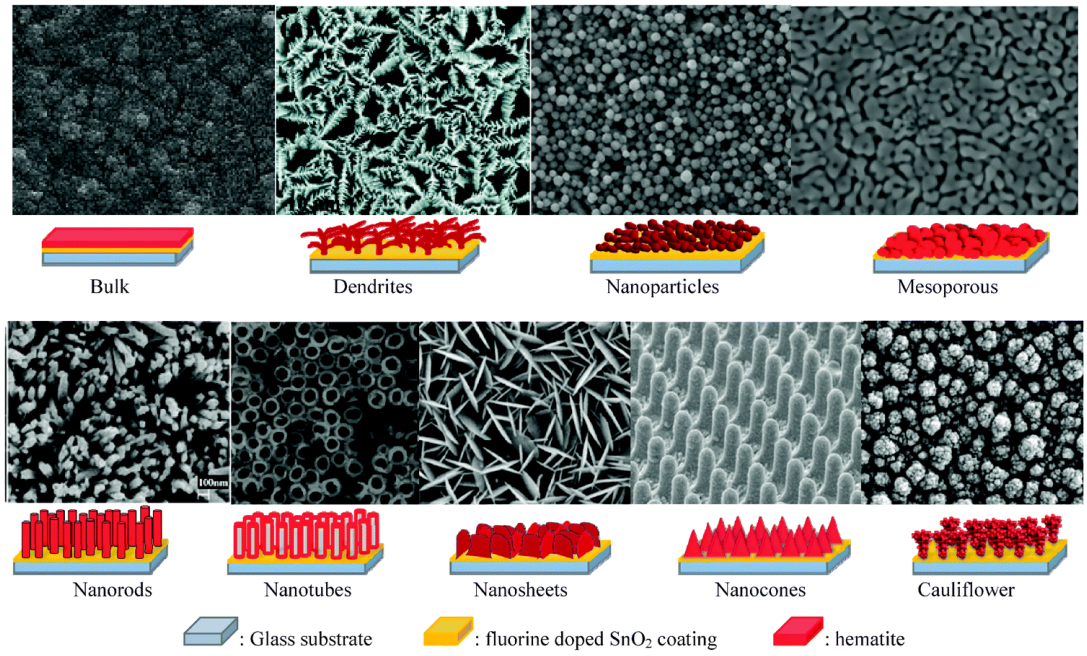

FIGURE 1.11: SEM images and respective schemes of distinctive hematite morphologies grown on the FTO coated glass substrate. [Extracted from [27]]

reached up to 3.45 mA·cm^{-2} at 1.23 V_{RHE} [53]. However, as we search for abundant, non-toxic and low-cost materials, their synthesis methods should equally be sustainable. The hydrothermal method stands out as a perfect candidate due to its diverse, user-friendly and scalable approach to conceiving nanostructured materials. Distinct architectures have been synthesized by hydrothermal method, like nanowires [74, 75], nanoflakes [83], nanosheets [84] and cauliflower-type structures [76], showing functional applicability and appealing performance for solar water splitting.

1.3.1.1 Nanowires (Nanorods)

Nanowires (NWs) caught significant attention for their simple structure, which enables the electrons to travel a straightforward path to the substrate [75, 85]. Additionally, the increase in the surface area of contact between the semiconductor and the electrolyte facilitates the collection of holes by the photoanode/electrolyte interface (Figure 1.12(a)). The first report on hematite NWs goes back to 2001 when Vayssieres et al. set an initial procedure to prepare hematite NWs by hydrothermal method, proving their synthesis through scanning electron microscopy images (SEM) images [74]. Then, Beerman et al. used this strategy to show an efficiency improvement of two orders of magnitude compared to other hematite films [86]. Since then, several works have explored this topic, using this and other methods, like annealing on an iron foil and

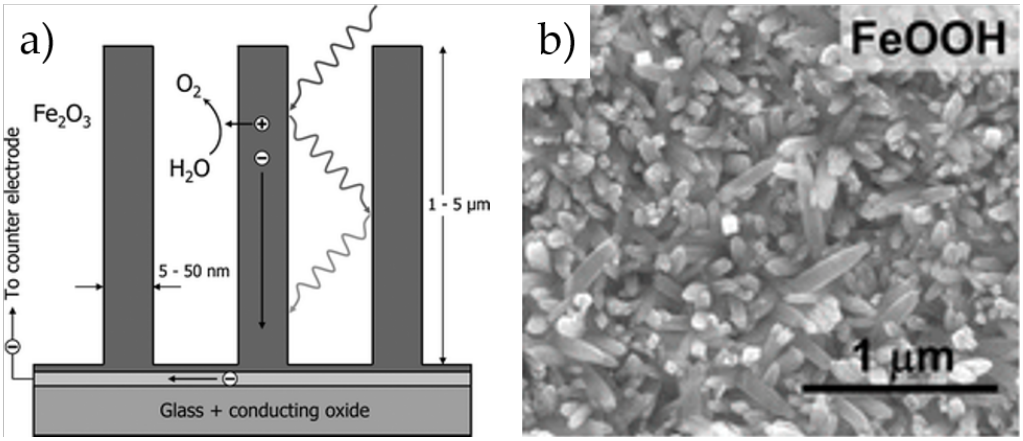

FIGURE 1.12: (a) Nanowires structure scheme representing the charge carriers (electrons and holes) paths after photogeneration. The increase of surface area is also observed as the electrolyte and sun light enter through the structure. [Adapted from [85]] (b) SEM image of β-FeOOH nanowires after hydrothermal treatment. [Adapted from [29]]

electrochemical routes, to find the optimum synthesis process that maximises the PEC performance.

Dedicating our focus to the hydrothermal method, the NWs grow vertically oriented on the conductive substrate from an aqueous chemical bath solution containing the Fe^{3+} precursor and an oxidation agent. High pressure and temperature conditions allow stable nucleation of the iron ions [87]. A low pH chemical solution and a high ionic strength reduce the interfacial tension between the solution and the as-formed crystals, which promotes the formation of a metastable iron oxyhydroxide phase (β-FeOOH, also called akageneite [Figure 1.12(b)]) [74, 88].

Many studies reported the combination of the Fe^{3+} precursor reagent with sodium nitrate ($NaNO_3$) [83, 84, 89–91] as did Vayssieres et al., while others opted for a novel strategy by Xi et al. [92] employing urea (CH_4N_2O) as the oxidation agent [93–95]. Although the contribution of these oxidation agents is usually not considered when analysing the results, the impact it has on the synthesis of a stable and pure form of iron oxide makes it a crucial factor for the performance of the photoanode. Mentions of the effect the oxidation agent has on hematite are not reported in the literature since results are always attributed to other aspects, like the iron precursor concentration or pH value [88] or changes in morphology (NWs diameter and thickness) [28]. Therefore, it is challenging to establish a comparison between the two agents and their effect on the prepared hematite photoanodes.

1.3.2 Elemental Doping

The incorporation of different elements (e.g. Sn, Co, Ti, to name a few) as dopants is an effective strategy to enhance the photoelectrochemical activity of hematite photoanodes [30, 96]. Intrinsic hematite is considered a weak n-type semiconductor with poor electric conductivity [38, 52]. Thus, doping increases the donor density, which raises the concentration of the majority charge carriers available, enhancing the electric conductivity of hematite.

Doping introduces chemical impurities in the intrinsic material structure, changing its electrical, optical and structural properties, turning it into an extrinsic semiconductor [97]. The dopant concentration stands out as a crucial parameter regarding semiconductor photoactivity. While low dopant concentrations do not sufficiently increase the donor density, over-doping introduces localized impurity states that act as recombination centers within the semiconductor band gap, decreasing the photoresponse [30]. Therefore, an optimum doping concentration for each material and applied dopant should be found in order to effectively enhance the PEC activity of hematite photoanodes [30, 76, 93, 94, 98, 99].

Hematite has been doped with diverse elements, such as B [89], Co [93, 100], Cr [90], Ge [84], Mn [94, 95], Ni [101], Ru [102], Sn [91], Ti [103–107] and Zr [83] to form a heavily n-type semiconductor with increased donor density and higher conductivity. Additionally, a p-type semiconductor can be formed by doping hematite with Cu [76] or Zn [99, 108]. In this case, the conductivity rises due to an increase in the acceptor density (related to holes/vacancies). Figure 1.13 presents a table representing the studies employed with these doping elements found in the literature.

Tin doping of hematite nanorods (NRs) was reported by Ling et al. through a two-step annealing approach without using any external reagent [91]. The first annealing ensured the transformation of the akagenite phase (β-FeOOH) into hematite (α-Fe_2O_3), whereas a second annealing step with temperatures above 750 °C promoted the Sn diffusion from the fluorine-doped tin oxide (FTO - F:SnO_2) conductive substrate. A photocurrent density improvement from 0.035 to 1.24 mA·cm^{-2} at 1.23 V_{RHE} was associated with the tin doping from the second annealing stage. Quitério et al. corroborated the Sn diffusion upon thermal annealing by Rutherford Backscattering Spectrometry (RBS) measurements that showed an in-depth percent Sn profile ca. 10 times higher than the sample with only the first stage, displaying higher photocurrent and lower onset potential [29].

Another approach to dope photoanodes consists on introducing a reagent with the dopant element precursor into the chemical solution of the hydrothermal method. This simple method

allows to effectively dope metal oxide films with any existing element. For instance, Gurudayal et al. [94] and Huang et al. [95] used $MnCl_2{\cdot}4H_2O$ as the Mn^{2+} precursor to dope hematite nanorods. Both works reported PEC enhances, with Gurudayal et al. attaining a photocurrent of 1.40 mA·cm^{-2} at 1.23 V_{RHE} for 5 % Mn doping, while 7 % Mn doping sample achieved 1.60 mA·cm^{-2} at 1.23 V_{RHE} in the case of Huang et al.. In terms of the onset potential, Huang et al. did not report any significant change upon Mn doping, whereas Gurudayal et al. attained a 30 mV cathodic shift with their 5 % Mn-doped sample. Nevertheless, the onset potential values remained high (V_{onset} ~ 0.8 - 0.9 V_{RHE}) when compared with the ideal hematite photoanode (V_{onset} ~ 0.4 V_{RHE}).

Moreover, Xi et al. [93] synthesized Co-doped hematite nanorods by adding a 5 % doping concentration of $Co(NO_3)_2$ to the mixture solution of the hydrothermal stage. The photoanode surface became rougher, increasing the surface area, which led to improvements in the charge separation and transport to the semiconductor/electrolyte interface. All of these combined contributed to an improvement in photocurrent density from 0.72 (untreated hematite sample) to 1.20 mA·cm^{-2} at 1.23 V_{RHE}, and an onset potential shift of around 40 mV to lower potentials.

Another dopant worth discussing is Ti, as proved by the number of studies involving Ti-doped hematite photoanodes [98, 103–107, 109–112]. Deng et al.[109] reported the highest photocurrent density obtained so far for Ti-doped α-Fe_2O_3 nanorods synthesised by hydrothermal method. The Ti doping promoted urchin-like nanostructures on top of nanorod arrays which increased the effective surface area, reduced the electron-hole recombination and increased the donor density, leading to a j of 1.91 mA·cm^{-2} at 1.23 V_{RHE}. Likewise, Wu et al. [112] observed a decrease in the feature size of the nanorods as Ti was introduced in the hematite structure, increasing j by 2.2 times compared with the undoped hematite. A novel strategy introduced by Yang et al. [103] led to the successful synthesis of Ti-doped hematite NRs through a two-step hydrothermal method. A short first hydrothermal stage without the dopant formed an undoped underlayer, which ensured homogeneity and low defect density at the interfaces, reducing the recombination centers in the electrode. Afterwards, the Ti dopant was introduced for a second stage to dope hematite NRs. This photoanode design reached a photocurrent density of 1.37 mA·cm^{-2} at 1.23 V_{RHE} and an onset potential of 0.84 V_{RHE}, with remarkable improvements against a comparative hematite film prepared by spray pyrolysis.

Taking everything into consideration, a straightforward hydrothermal synthesis method has not yet been consensually agreed upon across the scientific community. Although the reagent

$Fe_2O_3 \cdot 6H_2O$ is established as the Fe^{3+} precursor, the oxidation agent keeps changing between sodium nitrate and urea from one study to another. Moreover, the parameters of the hydrothermal method, such as temperature and time, differ not only from the oxidation agent and doping element used but also across the same doping element. To exemplify, while Deng et al. [109] reported the synthesis of Ti-doped hematite NRs with a hydrothermal stage at 95 °C for 4 h, Fu et al. [98] needed a higher temperature and longer time stage (100 °C for 10 h) to accomplish it.

In this work, we performed a comparative study of the oxidation agent between sodium nitrate ($NaNO_3$) and urea (CH_4N_2O) to finally allow a direct comparison of the morphological, structural, optical and photoelectrochemical impacts of these two reagents. The hydrothermal method with each oxidation agent was then coupled with a study of the dopant concentration for the Mn, Co and Ti elements, adjusting the doping range in accordance with the respective literature. With this work, we were able to determine the impact of the oxidation agents while making use of the improved charge collection given by the nanowires morphology (nanostructuring), the reduction of recombination centers in the photoanode achieved by the undoped hematite underlayer (surface/interface modifications) and the electric conductivity enhancement by the Mn, Co and Ti dopants introduced in the hematite structure (elemental doping).

Sample											Photoelectrochemical Performance			Reference
Photoanode	Dopant		2nd reagent	Size [cm²]	Nanostructure	Diameter [nm]	Thickness [nm]	Treatment		Electrolyte	Illuminate area [cm²]	On-set potencial	Plateau current	
	Reagent	%						Type	Temperatures & Times					
B-doped	$Na_2B_4O_7$ (pH=9.2)	0.10 M	$NaNO_3$	2 x 4	Nanowires	50	200	Soaked in solution for 5 min	HT 95°C 4h; ANL 550°C 2h + 650°C 25min.	1 M NaOH	—	0.90 V_{RHE}	1.12 mA/cm² at 1.23 V_{RHE}	doi.org/10.1016/j.jphotochem.2017.08.045
Co-doped	$Co(NO_3)_2$	5 % (7.5 mM)	Urea	—	Nanorods	80	≈ 380	Hydrothermal	HT 100°C 8h; ANL 550°C 2h + 800°C 20min.	1 M NaOH	0.2	0.66 V_{RHE}	1.2 mA/cm² at 1.23 V_{RHE}	dx.doi.org/10.1021/jp304285r
Cr-doped	1 M $Cr(ClO_4)$	16 at. %	$NaNO_3$	3 x 1	Nanorods	—	—	Hydrothermal	HT 100°C 6h; ANL 550°C 4h.	1 M NaOH	0.2	—	≈ 1.5 mA/cm² at 1.4 V_{RHE}	doi.org/10.1016/j.electacta.2017.12.049
Ge-doped	—	—	$NaNO_3$	3 x 1.5	Nanosheets	—	—	Ge colloidals in 2nd stage HT	HT 120°C 3h (FeOOH); HT 180°C 30h (Ge); ANL 550°C 2h.	1 M NaOH	0.10-0.15	≈ 0.96 V_{RHE}	1.40 mA/cm² at 1.23 V_{RHE}	doi.org/10.1016/j.nanoen.2014.08.005
Mn-doped	$MnCl_2$-H_2O	5 % (7.5)	Urea	1 x 2.5	Nanorods	≈ 70	≈ 400	Hydrothermal	HT 100°C 10h; ANL 550°C 2h + 750°C 20min.	1 M NaOH	—	≈ 0.9 V_{RHE} (less 30 mV than pristine hematite)	1.40 mA/cm² at 1.23 V_{RHE}	doi.org/10.1021/am500643y
Mn-doped + NiFe-LHD coat	$MnCl_2$-H_2O	7 % (0.105 mmol in 10 mL)	Urea	—	Nanorods	50 - 60	≈ 400	Hydrothermal	HT 100°C 10h; ANL 550°C 2h + 700°C 15min.	1 M NaOH	—	Mn: ≈ 0.80 V_{RHE} Mn + NiFe: ≈ 0.6 V_{RHE}	Mn: 1.60 mA/cm² at 1.23 V_{RHE} Mn + NiFe: ≈ 2.10 mA/cm² at 1.23 V_{RHE}	doi.org/10.1016/j.jcat.2016.05.007
Ni-doped	$NiCl_2$-$6H_2O$	8 % (0.4 M)	NaF + H_2O_2 + KCl	3 x 1	Nanospheres	500	—	Electrodeposition	Electrodeposition at 50°C; ANL 500°C 4h.	1 M NaOH	0.25	≈ 1.40 V_{RHE}	1.50 mA/cm² at 1.65 V_{RHE}	doi.org/10.1016/j.electacta.2011.10.051
Ru-doped	Ru-(acac)$_3$	5 % (5 mM)	—	0.5 x 1.5	Nanorods	8.6	≈ 500	Hydrothermal	HT 180°C 20min; Centrifug 5000rpm 5min; 20cycles doctor bladine: ANL 700°C	1 M NaOH	0.75	0.71 V_{RHE}	5.74 mA/cm² at 1.23 V_{RHE}	doi.org/10.1016/j.nanoen.2015.07.005
Sn-doped	$SnCl_4$	10 mg/ml in 1 mL	$NaNO_3$	—	Nanowires	60	≈ 700	From FTO vs Hydrothermal	HT 95°C 4h; ANL 550°C 2h + 800°C 20min.	1 M NaOH	—	a-Fe_2O_3: 0.6-0.8 V_{RHE} Sn: 0.65-0.8 V_{RHE}	a-Fe_2O_3: 1.24 mA/cm² at 1.23 V_{RHE} Sn: 1.84 mA/cm² at 1.23 V_{RHE}	doi.org/10.1021/nl200788y
Sn-doped	—	—	—	—	Nanocrystaline clusters of spherical grains	30 - 50	≈ 200	Pulse Reverse Electrodeposition(PRED) - doped from FTO	ANL 800°C 13.5min	1 M NaOH	—	≈ 0.76 V_{RHE}	0.65 mA/cm² at 1.23 V_{RHE}	dx.doi.org/10.1016/j.solmat.2015.05.020
Ti-doped	$Ti(OBu)_4$	1 % (1.5 mM)	$NaNO_3$	—	Nanorods	50	500	Hydrothermal with dopant on 2nd stage	HT 95°C 50min (s/dopant) + HT 95°C 13h (c/dopant) ANL 550°C 2h	1 M NaOH	—	Ti-Fe_2O_3: 0.88 V_{RHE} U/Ti-Fe_2O_3: 0.84 V_{RHE}	Ti-Fe_2O_3: 1.37 mA/cm² at 1.40 V_{RHE} U/Ti-Fe_2O_3: 1.64 mA/cm² at 1.40 V_{RHE}	doi.org/10.1039/C3TA13830E
Ti-doped	TiO_2	1%	—	—	Film with pores	—	≈ 400	Pulse Laser Deposition (PLD)	—	1 M NaOH	0.28	≈ 1.25 V_{RHE}	≈ 1.10 mA/cm² at 1.23 V_{RHE}	/dx.doi.org/10.1016/j.ijhydene.2013.10.031
Ti-doped	$C_{12}H_{28}O_4Ti$	2 % (0.6 mM)	—	2 x 2.5	Flower like (clusters)	—	≈ 400	Spray Pyrolysis	Pre-heated 350°C; Sprayed; ANL 550°C 2h.	0.1 M K-Pi	0.1256	≈ 1.14 V_{RHE} With H_2O_2: 0.64 V_{RHE}	1.09 mA/cm² at 1.8 V_{RHE} With H_2O_2: ≈0.88 mA/cm² at 1.23 V_{RHE}	doi.org/10.1016/j.electacta.2018.11.166
Ti-doped	$TiCl_4$	6.6 % (0.01 M)	—	—	Uniform dense packed structure	—	—	Spray Pyrolysis	Pre-heated 350°C. Sprayed.	0.1 M NaOH	—	?	0.80 mA/cm² at 0.95 V_{SCE}	doi.org/10.1016/j.tsf.2014.12.003
Ti-Fe_2O_3/Cu_2O		0.01 M Ti			Porous structure				Also sprayed.			?	2.60 mA/cm² at 0.95 V_{SCE}	
Ti-doped	$TiOCl_2$	0.2 % (0.3 mM)	—	1 x 3	Nanorods	—	480	Hydrothermal	HT 100°C 10h; ANL 600°C 2h.	1 M NaOH	—	≈ 0.9 V_{RHE}	1.25 mA/cm² at 1.23 V_{RHE}	doi.org/10.1016/j.apsusc.2015.10.170
Ti-doped NaF assisted		3 mM Ti +2mmol NaF in 10 mL	NaF		Nanocubes	≈ 900	850					≈ 0.87 V_{RHE}	2.35 mA/cm² at 1.23 V_{RHE}	
Zr-doped	$ZrO(NO_3)_2$-xH_2O	5.26 % (0.05 M)	$NaNO_3$	1 x 1	Nanoflakes	—	—	Hydrothermal	HT 120°C 16h; ANL 700°C 2h.	1 M KOH	—	> 1.40 V_{RHE}	0.52 mA/cm² at 1.5 V_{RHE}	doi.org/10.1016/j.apsusc.2018.12.061

FIGURE 1.13: State of the art of doping hematite.

Chapter 2

Experimental and Characterization Techniques

This chapter presents the detailed synthesis methods description and characterization techniques of the photoanodes fabricated in this thesis. An overview of the materials and growth processes underlying the photoelectrodes fabrication is taken, followed by a brief description of the different characterization techniques used: morphological, structural, photoelectrochemical, and optical characterizations.

2.1 Materials and Synthesis Methods

This section presents the materials and methods used to obtain the desired photoanodes under different fabrication conditions. Each step of the synthesis process will be carefully described: from the description of the materials' growth under the hydrothermal method and thermal annealing to the specific application in the fabrication of hematite and tungsten trioxide photoanodes.

Previously to experimental procedures, the safety data sheets of chemical reagents were consulted to evaluate all the risks and to be aware of the necessary individual safety equipment, such as goggles, lab coat, gloves or masks. For instance, an FFP3 mask was used to weigh the powder reagents, whereas a gas mask (double filter A1B1E1K1P3) was used for liquid/solvent reagents. Individual protection (lab coat and gloves) was always used during all laboratory experiments. Furthermore, all chemical procedures were manipulated inside an hotte bench, ensuring that all experiments are performed under safe conditions.

2.1.1 Materials

Chemicals employed in the experimental work were used as purchased without further purification. Deionized water (99.9 μS/cm) was used for cleaning purposes, while Ultra-Pure water (5.8 MΩ·cm) to prepare solutions. Both types of water were obtained from a Direct-Pure UP Ultrapure & RO Lab Water System from Rephile.

All the materials and chemical reagents are presented according to their purposes, with the chemical formula (when applied), name of the material/reagent, supplier company and purification percentage (when applied) as follows:

- Substrates:
  SnO_2, Fluorine-doped tin oxide coated glass substrates (FTO) - Solaronix, Switzerland, 7 Ω square^{-1}, 2.2 mm thick;
  SnO_2, Fluorine-doped tin oxide coated glass substrates (FTO) - Solaronix, Switzerland, 10 Ω square^{-1}, 1.0 mm thick.

- Substrate cleaning:
  CH_3COCH_3, Acetone - Labsolve, 99.7 % Vol.;
  C_2H_6O, Ethanol - JMGS - 99 % Vol;
  KOH, Potassium Hydroxide Pellets - Panreac, 85 %;
  Detergent - Derquim, 5-10 %.

- Hydrothermal method:
  $FeCl_3$·$6H_2O$, Iron (III) chloride hexahydrate - Acros Organics, 99+ %;
  $NaNO_3$, Sodium Nitrate BioXtra - Sigma Aldrich, 99 %;
  HCl, Hydrochloric acid - Fisher Scientific, 37 %;
  CH_4N_2O, Urea - Alfa Aesar;
  Na_2WO_4·$2H_2O$, Sodium tungstate dihydrate - Acros Organics, 99+ %;
  $(NH_4)_2C_2O_4$, Ammonium oxalate - Chem-Lab.

- Doping:
  $MnCl_2$·$6H_2O$, Manganese (II) chloride hexahydrate - Riedel-de Han, 97 %;
  $Co(NO_3)_2$·$6H_2O$, Cobalt (II) nitrate hexahydrate - Alfa Aesar 99.999 %;
  $SnCl_4$·$5H_2O$, Tin (IV) chloride pentahydrate - Sigma Aldrich, 98 %;
  $C_6H_{18}N_2O_8Ti$, Dihydroxybis (ammonium lactato) titanium (IV), 50 % w/w aq. sol.

- Electrolyte (for PEC measures):

  NaOH, Sodium Hydroxide - Chem-Lab, 1 M;

  Na_2SO_4, Sodium sulfate - Acros organics, 0.5 M.

2.1.2 Synthesis Methods

This section describes the synthesis techniques employed for developing the different photoanodes. Firstly, we clarify the cleaning process and preparation of the substrates for the subsequent photoanode depositions. Secondly, the hydrothermal method and thermal annealing treatment are explained, following the specific application in the fabrication of hematite and tungsten trioxide photoanodes. Last but not least, the electrodeposition setup is described as part of the metallic co-catalyst depositions of the ongoing work

Previously to any deposition, all conductive substrates of fluorine-doped tin oxide (FTO - F:SnO2) were cleaned based on an adapted sequential cleaning method reported by Francisco et al. [113]. FTO pieces (~ 1.2 x 2.5 cm^2) were carefully rubbed with acetone and detergent, following a sequence of ultrasonic baths with detergent (10 min), ethanol (10 min), detergent (10 min), ethanol (10 min), solution of 2 M KOH in ethanol 70 % (20 min) and deionized water (10 min). In more detail, acetone removes major contaminations, like the acetate ink used to mark the substrates; then, detergent removes grease and dirt, followed by ethanol which removes the detergent and organic waste. The KOH solution erodes the FTO surface, making it smoother for the photoanodes nanostructure to grow.

After cleaning, the substrates were placed on top of laboratory paper in a vertical position, supported and covered by a small beaker and a dome of glass (also cleaned and dried), respectively, to avoid dust contamination from the air. Then, a small area of the FTO surface (~ 1.2 x 0.75 cm^2) was covered with Kapton® tape in order to allow an electrical contact for electrochemical measurements, i.e. the non-deposited area establish a connection to an external circuit in which the photogenerated electrons in the photoanode that were collected by the FTO substrate can transfer to the external electric circuit.

Since different photoanodes and groups of samples require distinct reagents and concentrations, as for the case of elemental doping, this section introduces a general description of the synthesis methods, with specific details about the processes being present in the "Experimental Details" sections of Chapters 3 to 5.

FIGURE 2.1: Teflon recipient and the stainless-steel autoclave used to synthesize the photoanodes through hydrothermal method.

2.1.2.1 Hydrothermal method

As observed in Chapter 1, the hydrothermal method is a low-cost, user-friendly and scalable technique to the formation of diverse nanostructures.

The reaction process involves the combination of soluble precursor metal salts with an oxidation agent in an aqueous and/or organic solution inside the autoclave[1]. The growth of single crystals involves the sum of macro- and microprocesses occurring between the interface boundary of the solution and the crystal. Specifically, the metallic precursor in the solution (heavier) settles in the lower part of the autoclave. Upon heating, a temperature gradient is created along the autoclave, dissolving the metal solute in the hotter zone and transporting the saturated aqueous solution by convection currents to the upper cooler zone, where it is deposited on the seed crystal.

Acidic solutions (low pH, in the order of 1.5) are generally used to avoid the precipitation of species (Fe, W or other) in the solution during the procedure, allowing their availability for the nucleation processes. Particularly in the case of the iron oxyhydroxide phase (β-FeOOH), the use of a low pH chemical solution with a high ionic strength medium lowered the interfacial tension between the solution and the crystals being formed, promoting the stabilization in the akaganeite phase [74, 114].

The chemical solution is placed in a Teflon recipient (inert material) covered by a stainless-steel autoclave (Figure 2.1), in a heating chamber (Figure 2.2(a)). High pressure and temperature conditions allow the crystallization and dissolution processes to occur. For safety issues, no more than 3/4 of the recipient capacity should be filled due to high pressure and temperature conditions.

[1] Although the oxidizing agent is not mandatory, it is usually utilized.

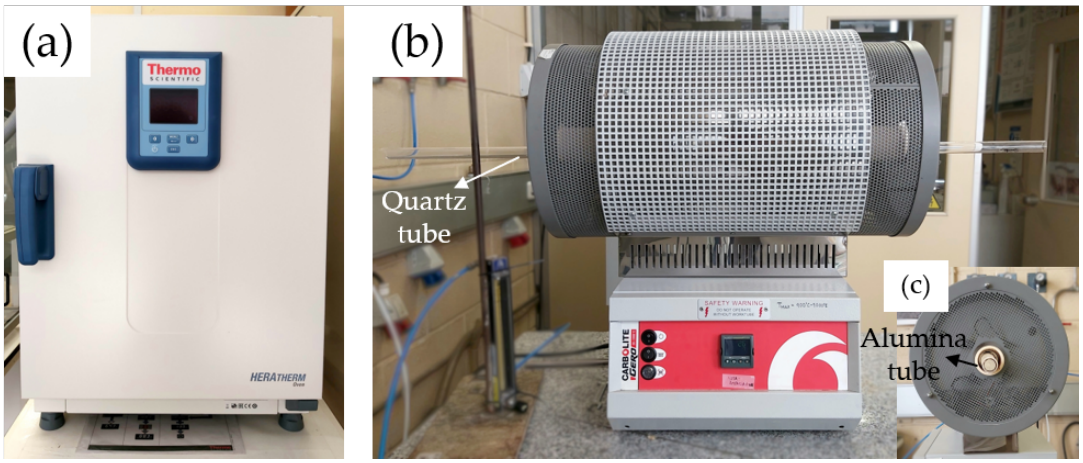

FIGURE 2.2: (a) Hydrothermal heating chamber. (b) Annealing furnace front view, and side view on (c).

Besides the reagents and concentrations of the chemical solution, the temperature and time of the hydrothermal stage are essential factors in the synthesis process. These factors were all taken into account, altering some - the oxidation reagents, dopant concentrations and time of hydrothermal stage - and maintaining others - Fe^{3+} precursor and concentration, and temperature of the hydrothermal stage - according to previous works from the IFIMUP laboratory [29, 115]

2.1.2.2 Thermal Annealing

Thermal annealing is a crucial part of the synthesis process of semiconductors to allow the photoanodes to oxidize. More specifically, this treatment restructures the lattice, eliminates defects/contaminants and promotes the crystallinity of the photoanodes, converting them into stable phases.

Moreover, when using FTO substrates, a diffusion of Sn^{4+} ions from the substrates to the nanostructures can be achieved with certain values of temperature, largely enhancing the photocurrent density outputs of the undoped photoanodes [29, 45, 91]. According to Ling et al., a significant Sn doping amount occurs for temperatures above 750 °C [91]. However, FTO substrates suffer thermal degradation for temperatures higher than 800 °C or heating times higher than 30 min at 800 °C, turning into an insulator, which increases its resistance, disrupting the sample performance [45, 116]. Following the study already conducted in our laboratory [29], the diffusion of Sn^{4+} ions was achieved by a second annealing stage of 800 °C for 20 min, with the TCO 10-10, as it maintains the FTO properties while taking advantage of the Sn diffusion.

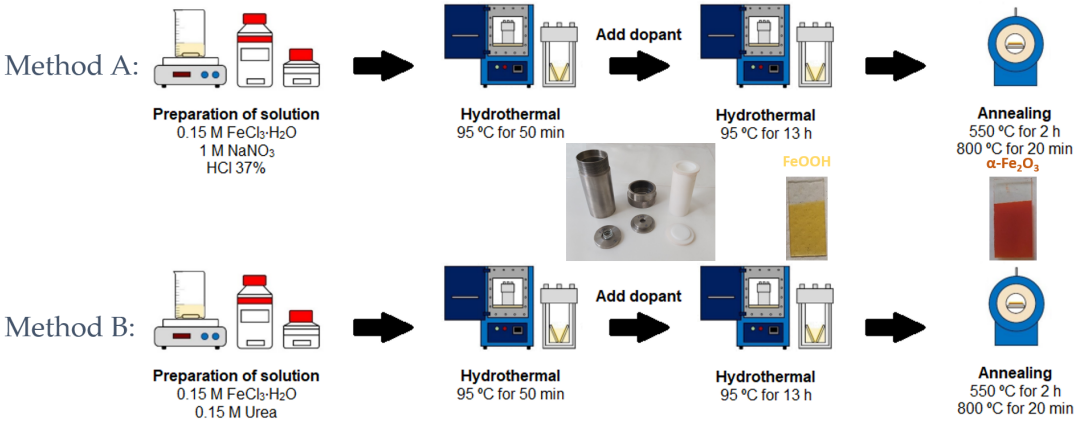

FIGURE 2.3: Synthesis methods used to prepare the doped hematite nanowires photoanodes. [Individual schemes adapted from [117]]

The thermal annealing was carried out in the furnace shown in Figure 2.2 (b). The as-prepared samples from the hydrothermal method were placed inside a quartz tube, covered by an alumina tube (Figure 2.2 (b) and (c)). The alumina tube avoided heat dissipation, while the quartz tube prevented contamination.

2.1.3 Hematite Nanowires

As introduced in Chapter 1, two distinct hydrothermal methods were applied in the synthesis of hematite NWs in order to compare the effect of the oxidation agent.

After cleaning and preparing the FTO substrates as previously described, a chemical solution was prepared with 0.15 M $FeCl_3 \cdot 6H_2O$ (iron (III) chloride hexahydrate, the Fe^{3+} precursor) and an oxidation agent. In method A, 1 M $NaNO_3$ (sodium nitrate) was used as the oxidation agent along with 56 μL HCl (hydrogen chloride) to set the pH to 1.5, whereas in method B only 0.15 M CH_4N_2O (urea) was needed to prepare hematite NWs. Then, the solution was transferred to a 25 mL capacity Teflon stainless-steel autoclave (Figure 2.1), where FTO substrates were placed with the conductive side facing the wall of the autoclave. Afterwards, a first hydrothermal stage of 50 min at 95 °C, with the undoped solution was performed to deposit a uniform undoped β-FeOOH layer, as revealed by Yang et al. and Quitério et al. [29, 103]. This layer acts as an underlayer as well it prepares the substrate for the formation of the doped β-FeOOH NWs, suppressing the back-diffusion of electrons from the FTO and improving the crystallinity at the hematite/FTO interface [103]. After the first stage, the dopant[1] was introduced for the second stage of 13 h at 95 °C, where it mixed with the undoped solution, doping the β-FeOOH NWs. In order to compare bare hematite with the doped samples, bare hematite photoanodes of both

[1] Dopant reagent and concentrations presented in the "Experimental Details" sections of Chapters 3 to 5.

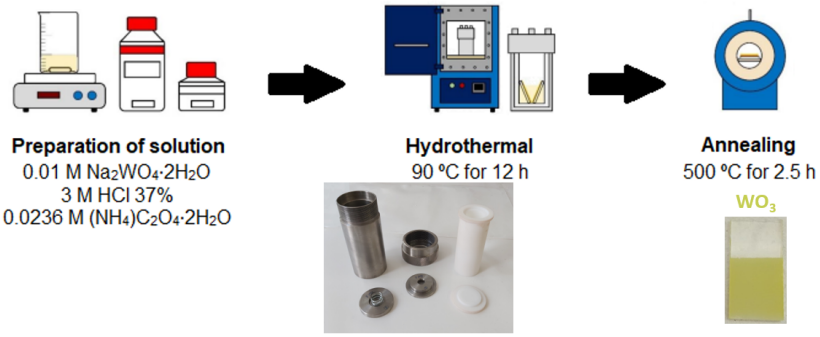

FIGURE 2.4: Synthesis method used to prepare the WO_3 nanoplates photoanodes. [Individual schemes adapted from [117]]

methods (A and B) were prepared by keeping the initial undoped solution for the second hydrothermal stage. Finally, a thermal annealing treatment at 550 °C for 2 h (10 °C/min ramp) and 800 °C for 20 min (8 °C/min ramp) was conducted on all samples to convert the as-prepared β-FeOOH phase (yellow sample on Figure 2.3) into the stable hematite phase (red sample on Figure 2.3). A schematic of the two synthesis methods used to prepare the hematite NWs is found in Figure 2.3.

2.1.4 Tungsten Trioxide Nanoplates

The WO_3 nanoplates were grown on FTO in two steps. Firstly, through a hydrothermal method previously reported [31], 9 mL of 0.01 M $Na_2WO_4{\cdot}2H_2O$ (sodium tungstate dihydrate) was dissolved in Ultra-Pure water under constant stirring at room temperature. Then, 3 mL HCl was added drop by drop, forming a yellowish precipitate, followed by 9 mL of 0.0236M $(NH_4)_2C_2O_4$ (di-ammonium oxalate), resulting in a total of 21 mL solution. The solution was then transferred into a 40 mL capacity Teflon stainless-steel autoclave along with the cleaned FTO substrates placed with the conductive side facing the wall of the autoclave. The autoclave was sealed and put in the oven for a hydrothermal stage of 12 h at 90 °C. Secondly, the samples were annealed in air at 500 °C for 2.5 h, forming the WO_3 nanoplates.

2.1.4.1 Electrodeposition

Electrodeposition, a shortcut for electrochemical deposition, is a common and user-friendly technique for the growth of metallic films on conducting substrates or NWs in templates. The method uses a three-electrode configuration: the conductive substrate as the working electrode (WE), platinum (Pt) mesh as the counter electrode (CE) and Ag/AgCl/saturated KCl electrode as

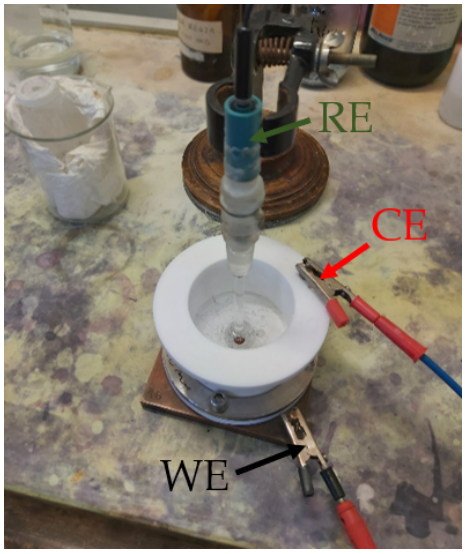

FIGURE 2.5: Electrodeposition homemade setup.

the reference electrode (RE). A homemade setup was used (Figure 2.5), consisting on an anodization cell made from a Teflon container placed on top of the substrates connected with a copper plate. The cell is filled with an ionic electrolyte containing the metal ionic species to be deposited. Applying a voltage between the cathode (conducting substrate) and the anode (Pt mesh), the metallic ions flow to the conducting substrate to electrochemically reduced, growing the metallic structure on top of the substrate.

The electrodeposition can be performed in three different modes: direct-current (DC) electrodeposition, alternating-current (AC) electrodeposition and pulse electrodeposition (PED). In this work, only direct-current (DC) electrodeposition was used, i.e. a constant potential was applied during all the deposition. Electrodepositions were conducted at room temperature, with a circular deposition shape of 0.5 cm^2 diameter. Current density-time (j-t curves) were recorded and monitored using an electrodeposition program provided by NOVA 2.1.5 Metrohm Autolab software.

2.2 Characterization Techniques

This section briefly describes the characterization techniques applied to evaluate the performance and properties of the developed photoanodes. In specific, the morphological, structural, photoelectrochemical and optical characterizations.

2.2.1 Morphological Characterization

2.2.1.1 Scanning Electron Microscopy (SEM)

Scanning Electron Microscopy (SEM) is one of the most versatile techniques for morphology examination and analysis, also providing chemical composition characterization [118, 119]. Since Dr. Zworykin [120] (in 1942) first used SEM to examine thick specimens with the emission of secondary electrons, an enormous development was made in the SEM instruments allowing it to be applied to a wide variety of samples, from films to nanostructures and crystals [119]. SEM provides images on nanometer (nm) to micrometer (μm) length scale, with a resolution from a few millimetres to ~ 2.5 nm [118].

The basic principle relies on irradiating the surface of a sample with a high-energy electron beam, set and focused by electrostatic and magnetic lenses, in a high vacuum. This irradiation emits electrons and photons that, according to their intensity, are used to form SEM images when all the spots are convoluted. Figure 2.6 represents the different generated signals: secondary electrons (SE), backscattered electrons (BSE), characteristic x-rays (EDX), continuum x-rays and other photons of various energies, which allows different imaging modes of scanning electron microscopy. For instance, BSE derives from elastic scattering, whereas inelastic scattering includes the formation of SE, characteristic x-rays, continuum x-rays and other photons of various energies. Backscattered electrons result from at least one elastic collision between the electron emitted by the electron beam and the sample's atom nucleus (Figure 2.6 (b)). Hence, samples composed by high atomic number (Z) elements, more positive charges on nucleus, will scatter more electrons, producing a higher BSE signal (brighter image). This contrast mechanism allows the recognition of different phases in the sample. BSE escape from the surface on straight trajectories with an energy higher than 50 eV, coming from deeper beneath the surface (see Figure 2.6 (a)). Therefore, detectors must be place with a large solid angle, causing a low lateral resolution (1.0 μm), but a larger volume of information [119, 121].

On the other hand, SE are low-energy electrons (below 50 eV), which are easily collected by a positively biased collector grid on the side of the sample. They result from the collisions of the primary electron-beam with the surface atoms from the sample (few nanometers from the surface), reaching a resolution of 1-10 nm [121]. Since the SE yield depends on the tilt angle of a surface element, an topographical contrast effect is created, which enable the collection of high resolution 2D images of the sample's topography, making this mode the most widely used.

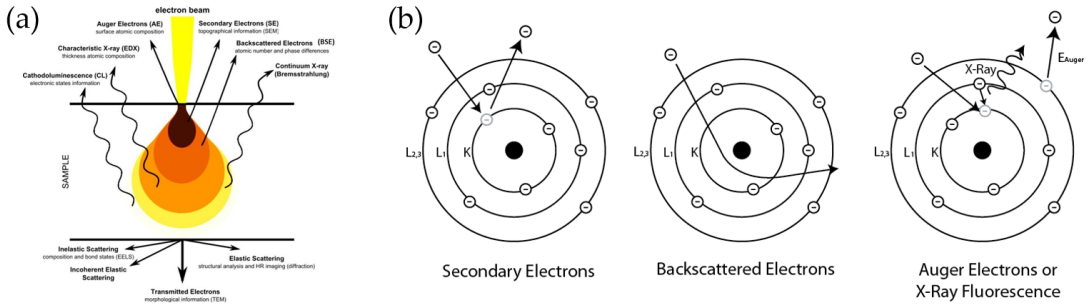

FIGURE 2.6: Schemes of (a) signals emitted from the interaction between the electron beam and the sample [Adapted from [122]], (b) SE, BSE and Auger electron interaction with atoms from the sample. [123].

FIGURE 2.7: Scanning Electron Microscope, FEI Quanta 400FEG Field Emission, at CEMUP.

In this work, SEM was performed using a FEI Quanta 400FEG Field Emission, at Materials Centre of the University of Porto (CEMUP) – Figure 2.7. Since the samples measured were semiconductors, a carbon tape was used to establish an electric discharge path, reducing the charge accumulation on the surface that would disrupt the acquired images. Images were taken from top view to determine the diameter of the NWs, and at cross-section to obtain the thickness of the photoanode deposited. These values were measure using the free software *ImageJ*.

2.2.2 Structural Characterization

2.2.2.1 X-Ray Diffraction (XRD)

X-ray diffraction is one of the most powerful techniques for determining the crystal structure of a material. From the crystal structure, it is possible to identify chemical compounds, lattice

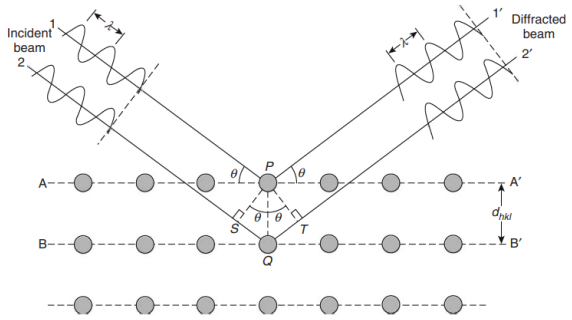

FIGURE 2.8: Bragg diffraction by crystal planes [From [124], adapted from [126]].

parameters and preferential directions, as well as the crystallite sizes and residual stress of a sample [124].

The principle behind XRD is that the incident of x-ray beams on a crystalline solid will be diffracted by the crystallographic planes of the solid, interfering with other diffracted beams, constructively or destructively. Constructively interference, i.e. waves that are 'in phase', will origin diffracted beams in specific angles (see Figure 2.8), θ, according to solid's lattice planes distance, d, as described by Bragg's law [125]:

$$n\lambda = 2d\sin\theta \tag{2.1}$$

In this work, a Rigaku SmartLab diffractometer (Figure 2.9) was used to record the diffractograms, with Cu Kα radiation (λ = 1.540593 Å) and an anode x-ray tube operated at 45 kV and 200 mA. A Ni filter was used to remove the Kβ radiation. Measurements were performed in parallel-beam (PB), 2θ mode with grazing incidence (PBGI) angles, adjusting the grazing incident angle to reduce the FTO signal compared to our samples signal (Figure 2.10). For this, values of 0.02 - 0.4° were used.

Long acquisition time scans were performed, in order to obtain enough statistic to individually fit the sample's peaks to Pseudo-Voigt functions. This allowed to conduct a peak boarding analysis, from which the crystallite size (D_{XRD}) and microstrain (ε) were estimated, using the Williamson-Hall relationship [127]:

$$w = w_{\mathrm{size}} + w_{\mathrm{strain}} = \frac{k\lambda}{D_{\mathrm{XRD}}\cos\theta} + 4\varepsilon\tan\theta, \tag{2.2}$$

where w is the full width at half-maximum (FWHM), θ the diffraction angle, k the Scherrer constant (0.94) and and λ the incident X-ray wavelength (1.540593 Å). It is important to notice that since Williamson-Hall method is established for powders and it is being used on nanostructured films, the absolute values obtained should not be considered too seriously. However,

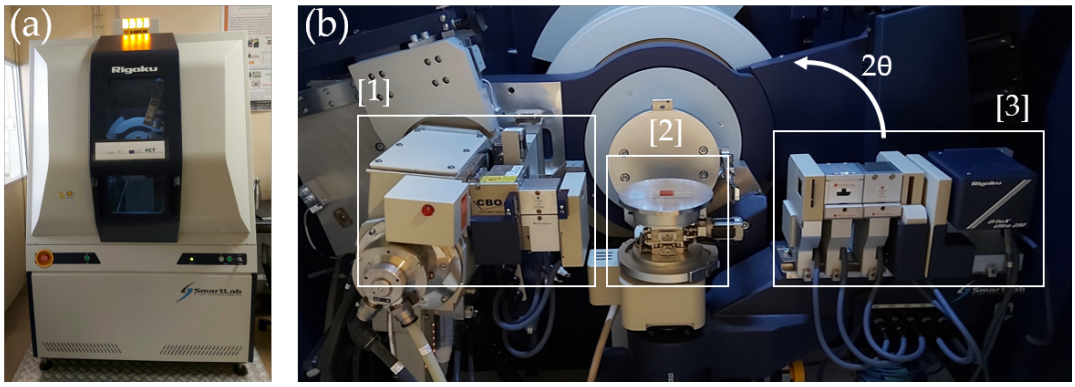

FIGURE 2.9: Rigaku SmartLab Diffractometer, at IFIMUP. (a) General view. (b) Detailed view of the main components: [1] x-ray tube generator and PB mode definition, [2] sample and sample holder, [3] Kβ filter and detector arm. The 2θ scan by the detector arm is illustrated by the arrow.

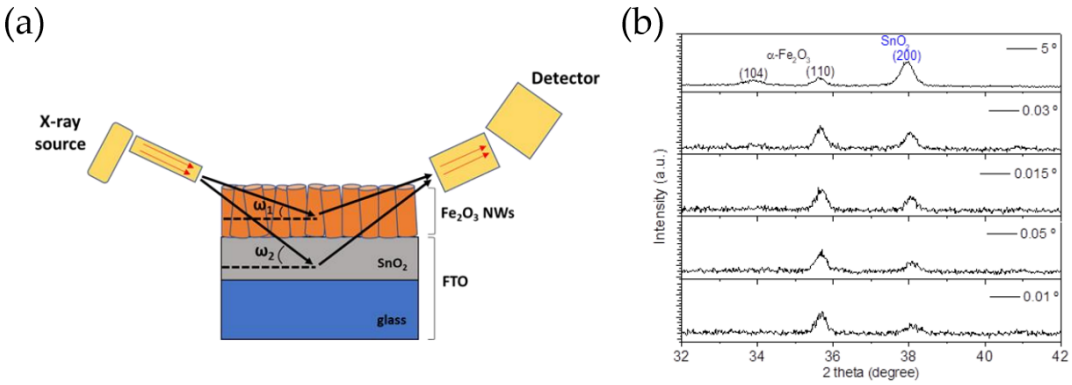

FIGURE 2.10: (a) Scheme of parallel beam mode with grazing incidence applied on hematite NWs deposited on FTO substrate. (b) It is possible to see the increase of the (110) hematite peak and reduction of the (200) FTO peak, as the grazing incidence angle decreases. [Adapted from [26]]

direct comparisons between samples were valid and enabled a further understanding of the impact that both synthesis process and dopants had on hematite NWs structure.

2.2.2.2 Rutherford Backscattering Spectrometry (RBS)

Rutherford backscattering spectrometry (RBS) is a widely used technique to study the in-depth profile of samples, allowing to determine the composition and element distribution within the sample [128]. Additionally, the thickness of the sample can be determined by knowing the materials density and energy straggling [129].

Based on Rutherford scattering principles and Geiger and Marsden experiments [130], RBS uses high energy with low mass particles positively charged (like H^+ or $4He^+$), to bombard a

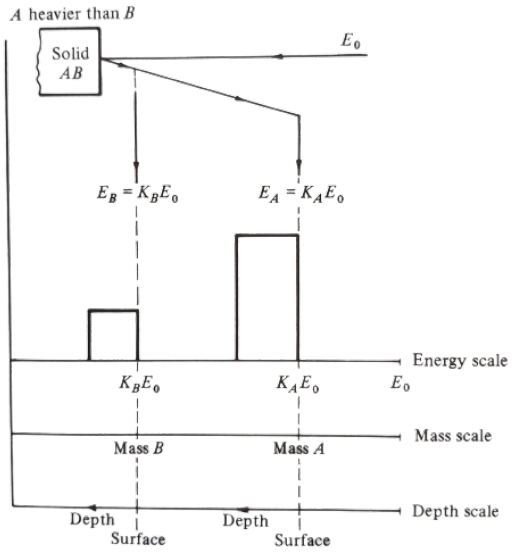

FIGURE 2.11: Rutherford Backscattering Spectrometry of a solid composed by elements of mass A and B, given that $M_A > M_B$. It is possible to see that element A has a higher backscattered energy than B, as A is heavier. Since both elements are at the surface, their peaks appear exactly at $K_A E_0$ and $K_B E_0$. If the element B was deeper below the surface, its peak will be shifted to an energy below its edge, due to the energy loss in the outer layer A. The length of the peak represents the thickness of the element's presence in the sample. In this case, both elements A and B are equally distributed in the sample, meaning their peak width is the same. [From [128]]

sample, in high vacuum, counting and measuring the energy of the particles elastically backscattered by the sample's nucleus. Hence, RBS has a great sensitivity to the detection of heavy elements (higher $Z \Rightarrow$ more positive charges $\Rightarrow$ more scattering), see Figure 2.11.

Since the collisions are elastic, energy and momentum are conserved, allowing to define a kinematic factor, K, defined by equation (2.3), which represents the ratio between the particle energy after the elastic collision and before the collision [131].

$$K = \frac{E_1}{E_0} = \left[\frac{\left(M_2^2 - M_1^2 \sin^2\theta\right)^{1/2} + M_1 \cos\theta}{M_1 + M_2} \right]^2 \tag{2.3}$$

Where E_0 and E_1 represent the particle energies before and after the collision, respectively; M_1 and M_2 are the incident particle mass and sample's atom mass, respectively; and θ is the scattering angle. Knowing these kinematics, it is possible to obtain information about the mass of the scattering center, the elements depth and the thickness of the sample [132].

RBS measurements of selected samples were performed in Campus Técnologico e Nuclear (CTN) from Instituto Superior Técnico (IST), in Lisbon. Dr. Sérgio Magalhães helped and guided the measurements and subsequent analysis, in a collaboration between IFIMUP and CTN-IST.

The setup consisted on a Van de Graaff accelerator ([1] on Figure 2.12) to produce the 2.0 MeV $^4He^+$ (α) particles beam. The beam was directed to the respective RBS line, by a controlled

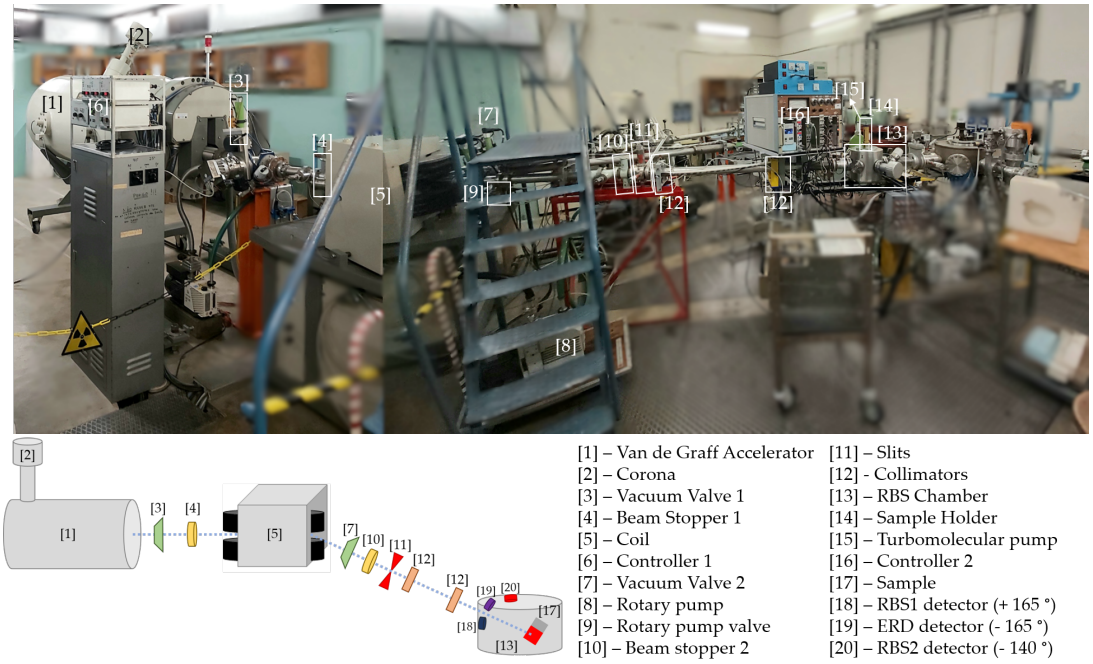

FIGURE 2.12: Rutherford Backscattering Spectrometry apparatus at CTN-IST on top. Scheme of the main components and beam line at lower left.

magnetic field generated through a coil ([5] on Figure 2.12), adjusting it for the measured currents on the slits ([11] on Figure 2.12) to be similar. An automatic stabilization system was used to make sure the slits currents remained the same. A pair of collimators ([12] on Figure 2.12) collimated the beam before it entered the chamber to hit the sample. Samples were placed on a manual goniometer, with two two monitorable axes, allowing spectra to be taken at two different angles (θ = 5, 30°) for more accurate data analysis. The backscattered particles were collected at +165, -140, and -165 ° (detectors RBS1, RBS2 and ERD, respectively) using silicon p-i-n diode detectors.

All along the measurements, high vacuum (lower than 10^{-5} mbar) was maintained by a turbomolecular pump ([15] on Figure 2.12), backup up by a rotary pump of two stages ([8] on Figure 2.12), in order to minimize the spread of the beam and sample backscattered particles due to collision with air molecules. The target was positively polarized to minimize the secondary electron emissions by the sample, reducing target current oscillations. Since the samples are semiconductors, no special attention was needed on the beam intensity, to avoid accumulation of charges at the surface of the sample. Regarding the analysis, simulations and fitting with NDF code [133, 134] were performed by Dr. Sérgio Magalhães.

2.2.3 Performance Characterization

2.2.3.1 Photoelectrochemical Measures (*j-V* curves)

The photocurrent density-voltage (*j-V*) curves is one of the most, if not the most important technique for the performance characterization on photoanodes for PEC cells, as the photocurrent is proportional to the hydrogen produced [135]. A linear sweep voltammetry in the potentiostat mode is performed, by reading the current produced as a sweep across the potential is done.

The *j-V* curves were performed on all the photoanodes produced on this work. Measures under dark and 1 sun simulated sunlight – calibrated with a c-Si photodiode ([3] on Figure 2.13) – (100 mW·cm^2, AM 1.5 G) were taken, using a class B solar simulator with a 150 W Xe lamp from Oriel, Newport ([2] on Figure 2.13) at Laboratory for Process Engineering, Environment, Biotechnology and Energy (LEBAPE), Porto. A three-electrode configuration was used: Ag/AgCl/saturated KCl electrode as the reference electrode (RE), a platinum (Pt) wire as the counter-electrode (CE), and the produced photoanode as the working electrode (WE) – Figure 2.13 lower left. The electrodes were placed inside a cappuccino PEC cell ([4] on Figure 2.13) [136], filled with 1.0 M NaOH (pH = 13.6) electrolyte solution for hematite photoanodes and 0.5 M Na_2SO_4 (pH = 7.2) for tungsten trioxide photoanodes. The illuminated surface area was 0.528 cm^2. Data were recorded with a ZENNIUM (Zahner Elektrik, Germany) workstation in potentiostat mode ([5] on Figure 2.13), together with Thales software for data acquisition ([6] on Figure 2.13). A scan rate of 10 mV/s for the potential range between 0.6 V_{RHE} to 1.8 V_{RHE}.

Since an Ag/AgCl/saturated KCl electrode was used as RE, the measured potentials were converted to the reversible hydrogen electrode (RHE), according to the Nernst equation:

$$E_{\mathrm{RHE}} = E_{\mathrm{Ag/AgCl}} + 0.059 \cdot \mathrm{pH} + {E^0}_{\mathrm{Ag/AgCl}}, \tag{2.4}$$

where E_{RHE} is the converted potential vs. RHE, $E_{\mathrm{Ag/AgCl}}$ is the potential measured experimentally against the reference Ag/AgCl electrode and ${E^0}_{\mathrm{Ag/AgCl}}$ = 0.1976 V at 25 °C.

The *j-V* curves were measured under front-illumination since it results in higher photocurrent than back-side illumination, as it can be seen in Figure A.1 at Appendix A. Since the majority carriers (electrons) have less transport limitations within hematite photoelectrodes than the minority carriers (holes), the transport of photogenerated electrons from hematite illuminated side through FTO direction is easier than the contrary trajectory holes (which have a short diffusion length of 2 - 4 nm) have to travel when the photoanode is illuminated from the back [26].

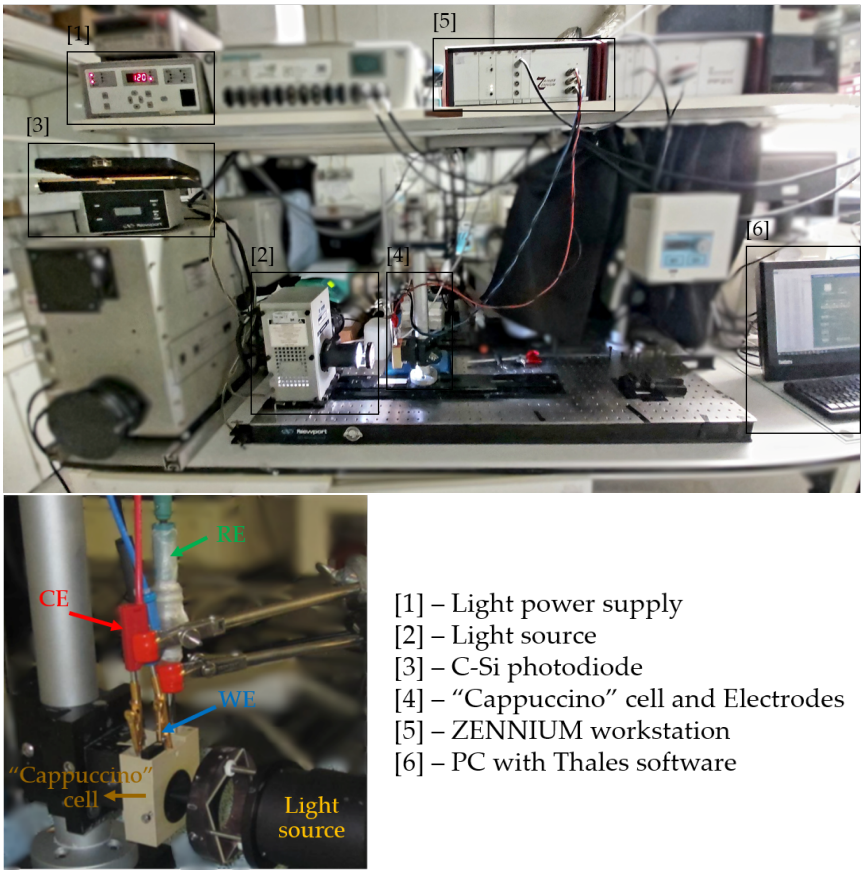

FIGURE 2.13: Electrochemical characterization setup at LEBAPE on top. Zoom on [4], showing the "cappuccino" cell and the three-electrodes at lower left.

One of the main results to take from these curves is the photocurrent density (j) at 1.45 V_{RHE}, which serves as a standard measure to evaluate the efficiency of the photoanodes, since j is proportional to the H_2 produced. The onset potential (V_{onset}) marks the minimum potential needed to begin the redox reactions. Therefore, a high j at 1.45 V_{RHE} indicates that a high volume of H_2 is produced, while a low V_{onset} means a low bias potential is needed to start producing H_2. A careful analysis must be done when comparing results, both of j and V_{onset}, as this values are dependent of experimental conditions that normally vary from work to work, or are omitted in the reports. For instance, the illumination area highly impacts the j result, as lower area achieve higher currents due to the defects of the active structure. Additionally, the irradiance intensity (standard value: 100 mW·cm^2), absence of ultraviolet (UV) or residual reactions occurring in the electrolyte filter may overvalue the photoanode performance.

2.2.3.2 Electrochemical Impedance Spectroscopy (EIS)

Electrochemical impedance spectroscopy (EIS) is an excellent method to study the charge transfer reactions occurring at the semiconductor/electrolyte interface, as the transport in the bulk

semiconductor. The operation of a PEC cell consists on a number of individual processes. Since most of them proceed at different rates, it is possible to separate them, according to the frequency at which they are occurring [136, 137].

EIS technique is an user-friendly technique, which consists on applying a small potential sinusoidal perturbation to the system, recording the amplitude and phase shift of the resulting current response, with an electrochemical station. However, it is very sensitivity, as it as the ability to provide information about the structure of the electrical double layer at the semiconductor/electrolyte interface and the charge transport processes occurring in the semiconductor and in the electrolyte [138]. A careful analysis must be done, considering other characterization info, like the nanostructure, thickness of sample and photocurrent density-voltage behavior, in order to achieve meaningful results.

The EIS measurements were performed under dark conditions, to promote charge accumulation, allowing a better study of the semiconductor/electrolyte interface. A similar setup as *j-V* curves was used (Figure 2.13), using the smaller sample holder of the cappuccino PEC cell with an opening area of 0.283 cm^2 (surface area of contact between the photoanode and the electrolyte). The three-electrode configuration was used, with a Ag/AgCl/saturated KCl electrode as the reference electrode, a platinum wire as the counter-electrode and the WO_3 NPs photoelectrodes as the working electrode, all immersed in a 0.5 M Na_2SO_4 electrolyte solution (pH = 7.2). Applying a small potential sinusoidal perturbation to the system, the amplitude and the phase shift of the resulting current response was recorded, using an electrochemical station (ZENNIUM workstation). The EIS spectra were collected at room temperature, between 0.6 V_{RHE} to 2.15 V_{RHE}, with steps of 0.05 V_{RHE}; in the frequency range of 0.1 Hz 100 kHz, and with a perturbation signal of 10 mV amplitude. The impedance data were fitted using the equivalent electrical model presented in Figure 6.5 at Chapter 6, using the ZView software (Scribner Associates Inc., USA).

2.2.4 Optical Characterization

2.2.4.1 UV-Vis Spectroscopy

Ultraviolet-Visible (UV-Vis) spectroscopy measures the optical properties of a material, in terms of light reflection efficiency (reflectance, *R*) and light transmission efficiency (transmittance, *T*), in the range of 200 nm to 700 nm. From this, the light absorption efficiency (absorbance, *A*) can then be calculated from:

$$A\,(\%) = 100 - R - T \tag{2.5}$$

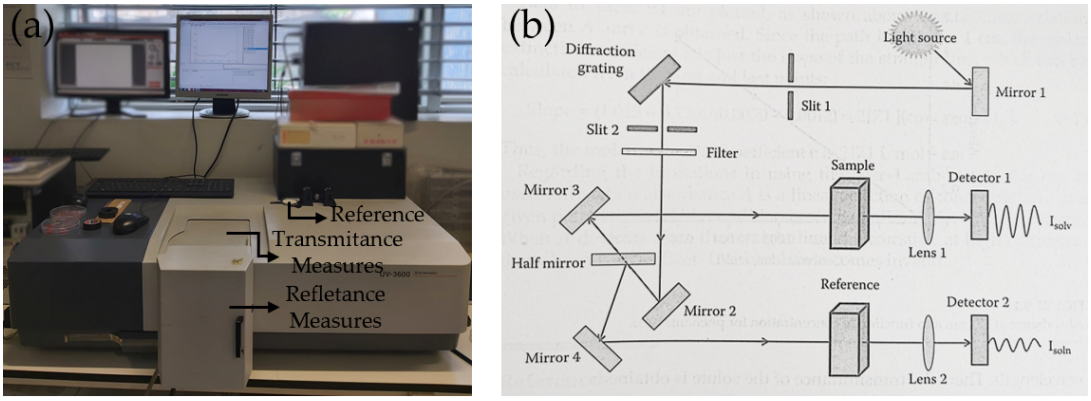

FIGURE 2.14: Ultraviolet-Visible spectroscopy (a) setup at LEBAPE; (b) system scheme. [Adapted from [139]]

Reflectance and transmittance data were collected using an UV-vis-NIR spectrophotometer from Shimadzu Scientific Instruments Inc., model UV-3600, Kyoto (Figure 2.14), at LEBAPE, Porto. FTO spectra were also collected, to subtract the FTO contribution on sample measures.

Combining the absorption spectra obtained by the UV-Vis spectroscopy, with the thickness of the samples determined by the SEM cross-section images, it is possible to assess the optical band gap of the photoanodes semiconductor, through Tauc plots [140]:

$$(\alpha h\upsilon) = B(h\upsilon - E_G)^n, \tag{2.6}$$

where α the absorption coefficient factor ($\alpha = 2.303 \cdot A/L$, L is the thickness of photoanode), $h\upsilon$ is the incident photon energy (in eV), E_G the optical band gap energy (in eV) and B and n are constants dependent on the electronic transition; being n = 2 for direct and n = 1/2 for indirect allowed transitions [43, 115].

Chapter 3

Unveiling the Oxidation Agent Effect on Bare and Manganese-doped Hematite Nanowires

3.1 Overview

Manganese (Mn) is a suitable dopant for hematite because of the iron-like atomic radius, which substantially avoids distortion of hematite crystal structure [94]. Additionally, based on the similar ionic radius to Fe, Mn doping has been reported to create fewer interface states as it is better accommodated in the hematite lattice, therefore increasing the reactivity towards the reduction of oxygen [141].

As a matter of fact, Mn-doped hematite material arises as an attractive photocatalyst due to this findings. As demonstrated by Cha et al. in their synthesis of Mn-doped hematite nanocrystals obtained by a hydrothermal method, for the degradation of methyl orange (MO) dye molecule [142]. Recently, Ramprasath et al. prepared 3D flower-like nanostructures by a polyolassisted hydrothermal process to photocatalytically degrade methylene blue (MB) dye solution [143]. Both studies found that Mn extended the interplanar space of the hematite structure and lowered the recombination rate of photogenerated electron-hole pairs, ultimately resulting in higher photocatalytic activity.

Moreover, Varshney et al. analysed the manganese influence in Mn-doped hematite (α-$Fe_{2-x}Mn_xO_3$) in terms of structural and transport properties [144]. At room temperature, the resistivity decreased from ca. 5.4 Ω-cm to ca. 800 Ω-cm with a Mn composition of x = 0.1.

Thereby, it was concluded that Mn doping increased the conductivity of hematite, even for small amounts of doping (x = 0.01, 0.10 and 0.50).

For PEC applications, although several dopants (e.g. Ti and Sn) has been highly implemented in hematite nanowires (NWs) via hydrothermal method, few works have been reported concerning Mn doping. Gurudayal and co-authors were the first to apply Mn-doped photoanodes for PEC cells applications [94]. Through a hydrothermal method based on urea as the oxidation agent, the authors synthesized hematite nanorods with a Mn doping concentration between 1 – 10 %, achieving the optimum PEC performance for a 5 % doping concentration. Even though a photocurrent density (j) of 1.40 mA·cm^{-2} at 1.23 V_{RHE} was achieved, the authors reported a faradaic efficiency[1] of 70.03 %. This reveals that the actual amount of O_2 evolved was inferior to the expected (i.e. the j value has a contribution from residual reactions apart from the OER and HER). The same photoanode also presented a cathodic shift of 30 mV in the onset potential (V_{onset}) compared with undoped hematite (~ 0.9 V_{RHE}). On the other hand, when other studied of the Mn concentration on hematite NWs (also obtained by hydrothermal route) were carried out, no improvement of the V_{onset} was found [95]. Though, higher j (1.60 mA·cm^{-2} at 1.23 V_{RHE}) was attained for a 7 % Mn-doped concentration, associated with an increase in the donor density and enhanced charge separation efficiency. However, the calculated faradaic efficiency was only 65 %.

Table 3.1 summarises the obtained results concerning j and V_{onset} reported in the literature. However, the presented faradaic efficiencies allow the determination of rectified values of j, calculated by multiplying the presented j values by the reported faradaic efficiency. This effective j traces the approximately same j for both studies (~ 1 mA·cm^{-2} at 1.23 V_{RHE}). Additionally, other factors, such as the lower illumination areas (or even not reported), enhance the difficulty of comparing the PEC results in the literature. In spite of an improvement in photocurrent density, mainly attributed to an increase in donor density and enhanced charge separation efficiency, appear to be established for Mn doping of α-Fe_2O_3 nanorods, the onset potentials remain unduly anodic compared to the ideal hematite photoanode (V_{onset} ~ 0.4 V). Reported onset potentials remain at ca. 0.8 – 0.9 V_{RHE}, still requiring excessive energy to begin hydrogen production.

Typically, sodium nitrate ($NaNO_3$) is extensively used as the oxidation agent in the hydrothermal synthesis of undoped (bare hematite) [29] and doped hematite with several elements (like B [89], Co [100], Cr [90], Ti [109], Zr [83], etc.). Though, to the best of our knowledge, no reports of

[1] The faradaic efficiency is defined as the ratio of the experimentally detected amount of an objective gas (e.g. O_2) and the amount of theoretically generated gas.

Reference	**Mn doping concentration [%]**	***j* at 1.23 V_{RHE} [mA·cm^{-2}]**	**V_{onset} [V_{RHE}]**	**V_{onset} shift [mV]**
Gurudayal et al. [94]	5	1.40	~ 0.90	30
Huang et al. [95]	7	1.60	~ 0.80	—

TABLE 3.1: Photoelectrochemical performance features, j and V_{onset}, of Mn-doped hematite nanorods (NWs) studies from literature.

using $NaNO_3$ as the oxidation agent for the implementation of Mn-doped hematite NWs have been found.

In this chapter, a systematic and multifaceted study of Mn doping in hematite nanowires is presented, combining the variation of two parameters: (i) the oxidation agent of the hydrothermal solution and (ii) the concentration of the Mn dopant. The oxidation agent used to oxidize to Fe^{3+} precursor in the hydrothermal treatment was tested with $NaNO_3$ (method A) and urea (method B). Secondly, the doping concentration of Mn was tested for 1, 7 and 13 %, according to the doping range from literature studies [94, 95]. Furthermore, the impact of these synthesis parameters on the PEC performance was correlated with morphological, structural and optical characterization.

3.2 Experimental Details

Mn-doped hematite photoanodes were prepared by a hydrothermal method (Subsection 2.1.3 of Chapter 2). The FTO glass substrates were cleaned by the methodology described in Subsection 2.1.2 and placed in a 25 mL stainless-steel autoclave filled with a 20 mL chemical solution made according to two approaches: method A – 0.15 M $FeCl_3{\cdot}6H_2O$ + 1 M $NaNO_3$ (oxidation agent) + 56 μL HCl; method B – 0.15 M $FeCl_3{\cdot}6H_2O$ + 0.15 M CH_4N_2O (oxidation agent).

Afterwards, a first hydrothermal stage of 50 min at 95 °C with the undoped solution was performed to deposit a uniform undoped β-FeOOH layer (Subsection 2.1.3). Then, the amount of $MnCl_2{\cdot}6H_2O$ (1, 7, 13 % in relation to the Fe^{3+} concentration) was added to the solution for the second stage of 13 h at 95 °C, merging with the undoped solution to dope the β-FeOOH NWs with Mn^{2+}. This 2nd stage was performed on both methods (A and B). In order to compare bare hematite with the doped samples, bare hematite photoanodes of both methods (A and B) were prepared by keeping the initial undoped solution for the second hydrothermal stage. Finally, a thermal annealing treatment at 550 °C for 2 h (10 °C/min ramp) and 800 °C for 20 min (8 °C/min

	Synthesis Method	
	Method A – $NaNO_3$	Method B – Urea
Doping Concentration [%]	0	0
	1	1
	7	7
	13	13

TABLE 3.2: Mn-doped and bare hematite photoanodes prepared.

ramp) was conducted on all samples to convert the as-prepared β-FeOOH phase into the stable hematite phase (Subsection 2.1.3) [29]. The two groups of samples are summarized in Table 3.2.

Summarizing, four samples according to the concentration of Mn dopant (0, 1, 7 and 13 %) were synthesized for both methods A (with $NaNO_3$) and B (with urea) to allow a methodical analysis of not only the oxidation agents but also the doping concentration impact on hematite NWs.

3.3 Results and Discussion

3.3.1 Photoelectrochemical response

The photoelectrochemical performance of the hematite NWs photoanodes was assessed by photocurrent density-voltage (j-V) curves. Figure 3.1(a) and (b) show the j-V characteristic curves under dark and simulated sunlight for the two sets of samples (Table 3.2), synthesized with method A ($NaNO_3$) and method B (urea), as described in the previous section. Dark j-V curves present negligible currents until a potential higher than $\sim$ 1.65 V_{RHE} is applied, from which the oxygen evolution reaction (OER) begins to occur between the FTO substrate/electrolyte interface. By illuminating the photoanode with simulated sunlight, a j sharp increase in current is obtained at much lower potentials, eventually stabilizing in a plateau photocurrent density (plateau current) for higher applied potentials.

As discussed in Chapter 2, the plateau current (j at 1.45 V_{RHE}) is proportional to the H_2 produced, while the minimum potential needed to begin the OER reaction defines the onset potential (V_{onset}). Therefore, high j at 1.45 V_{RHE} indicates the production of high volume of H_2, while a low V_{onset} shows a reduced cell dependence on external energy sources. For both sets of samples, j at 1.45 V_{RHE} and V_{onset} were extracted from j-V curves and plotted against the Mn doping concentration (C_{dopant}) (Figure 3.1(c) and (d), respectively).

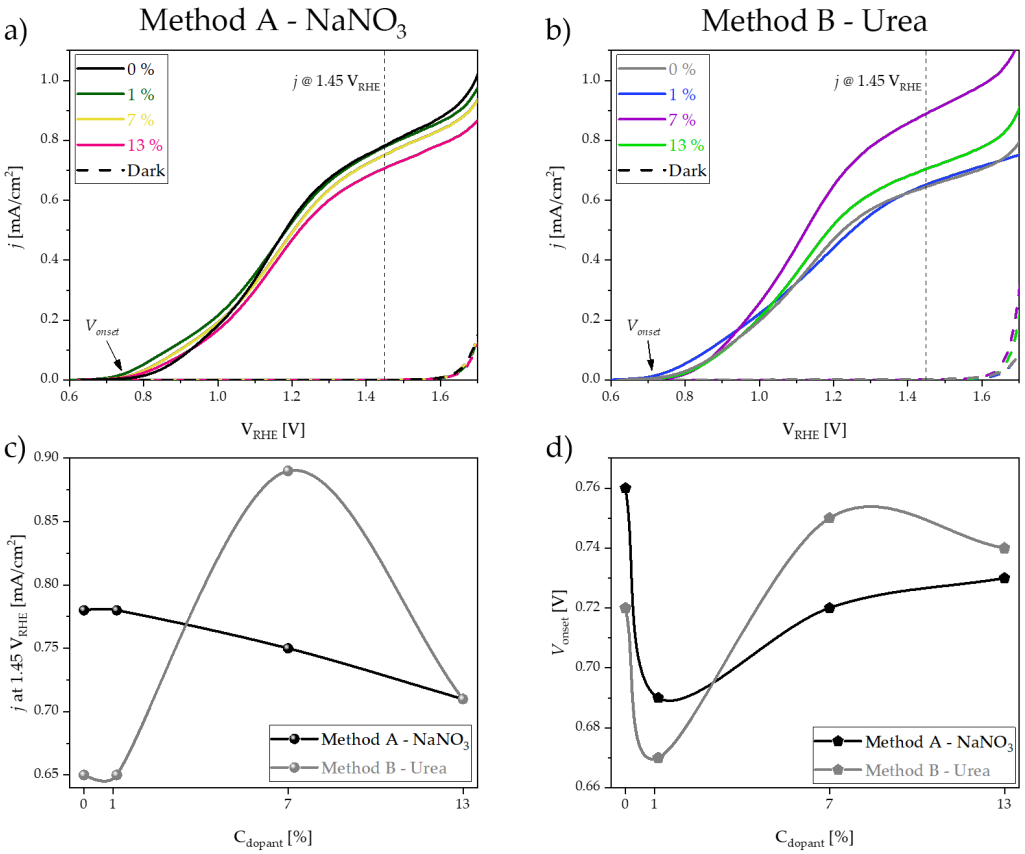

FIGURE 3.1: Photocurrent density-voltage characteristic curves of the Mn-doped hematite nanowires according to the synthesis method: (a) method A with $NaNO_3$ and (b) method B with urea. (c) j at 1.45 V_{RHE} and (d) V_{onset} for the different synthesis methods as a function of doping concentration (C_{dopant}).

Bare hematite photoanodes (without doping - C_{dopant} = 0 %) synthesized by the two hydrothermal methods (A and B) showed that the oxidation agent ($NaNO_3$ or urea) affected differently the PEC performance of hematite NWs. Higher j was attained by Method A ($j \sim 0.78$ mA·cm^{-2}) compared with method B ($j \sim 0.65$ mA·cm^{-2} at 1.45 V_{RHE}). Although the V_{onset} for method A is 60 mV higher than for method B, the significant j gain in method A leads to the usual preferential choice of $NaNO_3$ as the oxidizing agent in the hydrothermal synthesis of bare hematite NWs [29, 114].

Introducing 1 % of Mn dopant, the j response remained the same as bare hematite (C_{dopant} = 0 %). However, increasing the Mn doping concentration to 7 % led to opposite j responses: for method A, j smoothly decreased to 0.75 mA·cm^{-2}, while for method B, j sharply increased up to 0.89 mA·cm^{-2} at 1.45 V_{RHE}. Once again, the oxidation agent exhibited a noticeable impact on the photoanode performance, as opposite j behaviours were observed in the two approaches considered. Further doping to 13 % was found to decrease the j response, resulting in identical

j values of 0.71 mA·cm^{-2} at 1.45 V_{RHE} for both A and B methods.

Generally, method B samples showed lower j values than method B (concluded by the average j values: $\overline{j_A} \sim 0.76$ compared to $\overline{j_B} \sim 0.73$ mA·cm^{-2} at 1.45 V_{RHE}). In detail, method A ($NaNO_3$) reported similar j values for bare and Mn-doped photoanodes. The maximum j value of 0.78 mA·cm^{-2} at 1.45 V_{RHE} for bare and 1 % Mn C_{dopant} decreased to 0.71 mA·cm^{-2} with further doping amounts (Figure 3.1(c)). On the other hand, method B (urea) presented to be more sensitive to the Mn presence in hematite NWs (grey line and dots in Figure 3.1(c)). An optimum j performance of 0.89 mA·cm^{-2} at 1.45 V_{RHE} was observed for 7 % Mn-doped hematite NWs synthesized by method B (urea), reaching a 37 % increase when compared to the respective bare hematite.

In terms of the V_{onset}, samples with 1 % Mn doping prepared either with A or B approach led to lower V_{onset} when compared with the undoped hematite sample (Figure 3.1(d)). Remarkable cathodic shifts of 70 mV and 60 mV were obtained for methods A and B, respectively. Further doping increased the V_{onset} to higher values for both schemes. Although the absolute values of V_{onset} depend on the experimental setup and the method used to determine it [48], it is worth mentioning that the V_{onset} obtained by the 1 % Mn-doped hematite NWs photoanodes from method A (~ 0.67 V_{RHE}) is very close to the ideal hematite photoanode (~ 0.4 V_{RHE}) [53], especially when comparing with the ones reported in the literature ($\sim 0.8 - 0.9$ V_{RHE}) [94, 95].

3.3.2 Morphological Characterization

Scanning electron microscopy (SEM) allowed the observation of the photoanodes' morphologies at a micro and nanometer scale. Through SEM images, we were able to study the morphological impact of both strategies, the oxidation agent and the Mn doping concentration, on hematite NWs.

Figure 3.2 revealed that the nanowires morphology and growth on top of the FTO substrates was successively achieved for all photoanodes of both sets of samples. Generally, a NWs' euhedral shape was unveiled due to the fusion between neighbouring NWs due to the second annealing step at 800 °C [29]. Comparing the morphology of bare hematite ($C_{\mathrm{dopant}} = 0$ %) photoanodes of both oxidation agents (0 % samples from methods A and B in Figure 3.2), it was possible to observe that method A ($NaNO_3$) promoted more NWs aggregation than method B (urea). The NWs aggregation created areas surrounded by void paths (as illustrated by the red lines in Figure A.2 from Appendix A). While all Mn-doped samples prepared with method A kept this feature, in method B, only 1 % and 13 % Mn-doped samples presented NWs aggregation,

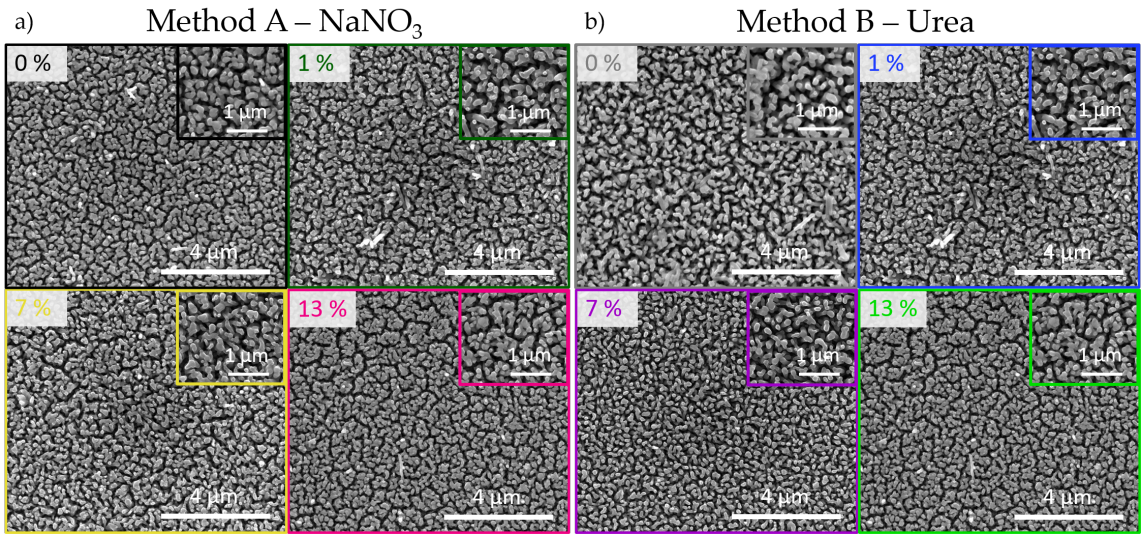

FIGURE 3.2: Scanning electron microscopy images of Mn-doped α-Fe_2O_3 NWs synthesized by (a) method A with $NaNO_3$ and (b) method B with urea. Inset figures show a closer look at the photoanodes' NWs.

even though with a lower degree. The sample with 7 % Mn doping from method B led to uniformly dispersed NWs with a better overall distribution. The dispersion of NWs usually leads to higher penetration of the electrolyte through the semiconductor, which increases the working surface area of the photoanode, thus enhancing its PEC performance [85, 91, 109]. Indeed, the sample with the most dispersed NWs, 7 % Mn-doped hematite from method B, led to the maximum j attained of 0.89 mA·cm^{-2} at 1.45 V_{RHE}.

Top-section SEM images (Figure 3.2) allowed us to measure the diameter (D) of the NWs for all the samples. Figure 3.3(a) represents D behaviour as a function of the Mn C_{dopant} for both methods A and B. A similar trend was observed for both A and B approaches, in particular, a general decrease of D occured upon Mn doping. Moreover, in the case of method B, it is worth mentioning that D *vs* C_{dopant} showed a similar behaviour as j *vs* C_{dopant}, where broader D led to the highest j value (7 % Mn doping).

In addition, the NWs thickness (L) in length was determined from the SEM cross-section images, as illustrated by the inset image in Figure 3.3(b). By altering the oxidation agent in the hydrothermal synthesis for bare hematite, highly different values of L are obtained. While for the most widely used and reported oxidation agent for bare hematite (method A – $NaNO_3$) the measured L was ca. 378 ± 16 nm, for the urea oxidizing agent (method B) twice the thickness was obtained (ca. 684 ± 27 nm). On the contrary to D *vs* C_{dopant} behaviour, L *vs* C_{dopant} presented completely different trends for each (A or B) hydrothermal synthesis method (Figure 3.3(b)). While in method A ($NaNO_3$) adding just 1 % of Mn caused a sharp L decrease (from

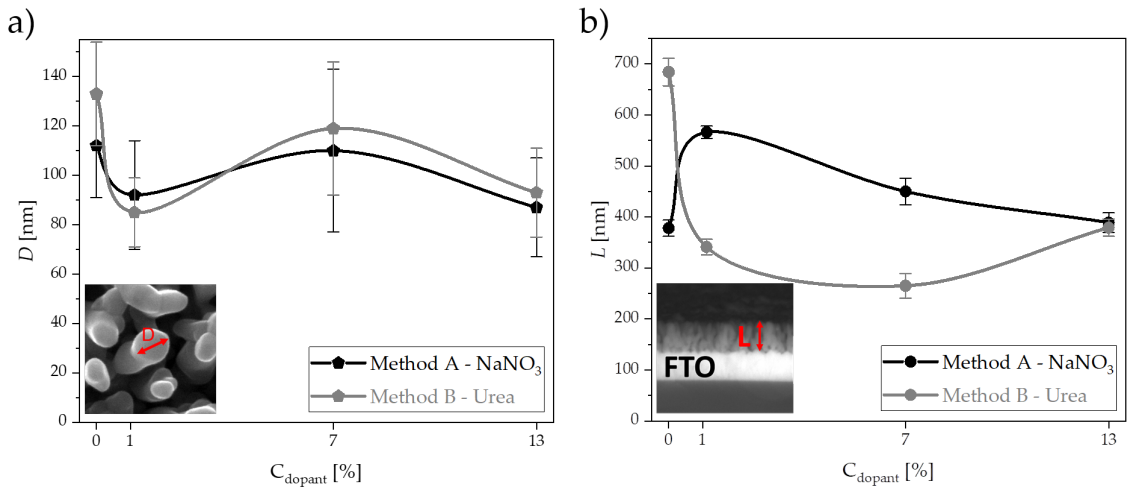

FIGURE 3.3: (a) Diameter (D) and (b) thickness (L) of Mn-doped α-Fe_2O_3 NWs as a function of doping concentration (1 – 13 %).

684 ± 27 nm to 341 ± 15 nm), method B (urea) resulted in a smooth increase (from 378 ± 16 nm to 566 ± 12 nm). Further doping increases (7 % and 13 %) smoothly altered L values in the same range with the lower L for 7 % Mn-doped of method B.

Mn doping by method B induced photoanodes with smaller L, which makes an easier pathway for the electrons to reach the conductive substrate, thus reducing the probability of electron-hole recombination [115, 145]. Indeed, the smallest thickness obtained for 7 % Mn-doped (method B: L = 265 ± 24 nm) could be the cause of the optimum j exhibited for this sample (Figure 3.1(c)). Additionally, the larger L (~ 684 nm) of bare hematite from method B than bare hematite from method A (~ 378 nm) led to a j ~ 0.65 and j ~ 0.78 mA·cm^{-2} (1.45 V_{RHE}), respectively. This evinces that thinner thickness leads to best j responses. However, when adding 1 % doping, neither the sharp decrease in method B nor the smooth increase in method A led to a variation of j (Figure 3.1(c)). Therefore, it appears that other factors are offsetting the expected variations in j promoted by the photoanode thickness.

3.3.3 Structural Characterization

X-Ray Diffraction

X-ray Diffraction (XRD) allowed the identification of the crystallographic phase for all fabricated samples. Using a parallel beam (PB) configuration with grazing incident omega (ω) angles allowed us to isolate the contribution of synthesized material from the FTO substrate signal [26].

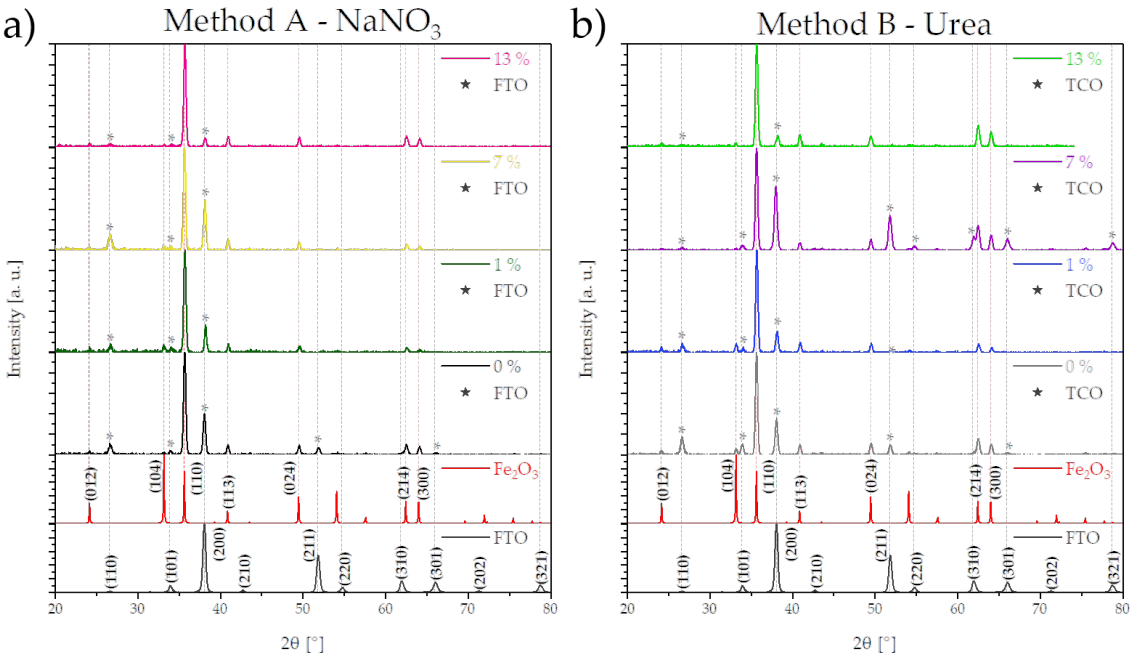

FIGURE 3.4: X-Ray Diffraction patterns of Mn-doped α-Fe_2O_3 photoanodes synthesized by (a) method A with $NaNO_3$ and (b) method B with urea.

Figure 3.4(a) and (b) present the diffractograms of the undoped and Mn-doped hematite photoanodes synthesized by the methods A ($NaNO_3$) and B (urea), respectively. After the hydrothermal growth, as-prepared NWs presented a peak with (211) orientation, corresponding to the β-FeOOH phase (JCPDS 34-1266) [103]. Applying the two-stage thermal annealing treatment, XRD diffractograms proved the synthesis of the thermodynamically stable hematite phase (JCPDS 33-0664), described as a corundum crystalline structure with hexagonal closed-packed unit cell. For both sets of samples, the preferential orientation occurred at the plane (110), contrary to what occurs in hematite thin films [146]. Additionally, smaller peaks from planes (012), (104), (113), (024), (214) and (300) were also identified. No peaks related to Mn doping were detected since the doping concentration in the material is lower than the diffractometer detection limit. Nevertheless, it can be noticed that all Mn-doped samples provoke the FTO substrate peaks to shift slightly to higher angles (observed in the FTO peak of (200) plane), except for 7 % Mn-doped samples of method B, which exhibit an opposite shift to lower angles. The FTO shift to lower angles has been associated with an expansion of the hematite lattice due to higher Sn^{4+} diffusion [147]. This implies that Mn doping with 7 % in method B improved the ability for Sn to enter the hematite NWs structure. However, further structural characterization, e.g. X-Ray Photoelectron Spectroscopy (XPS) should confirm this hypothesis.

The strong preferential orientation of the [110] axis vertical to the substrate has been shown

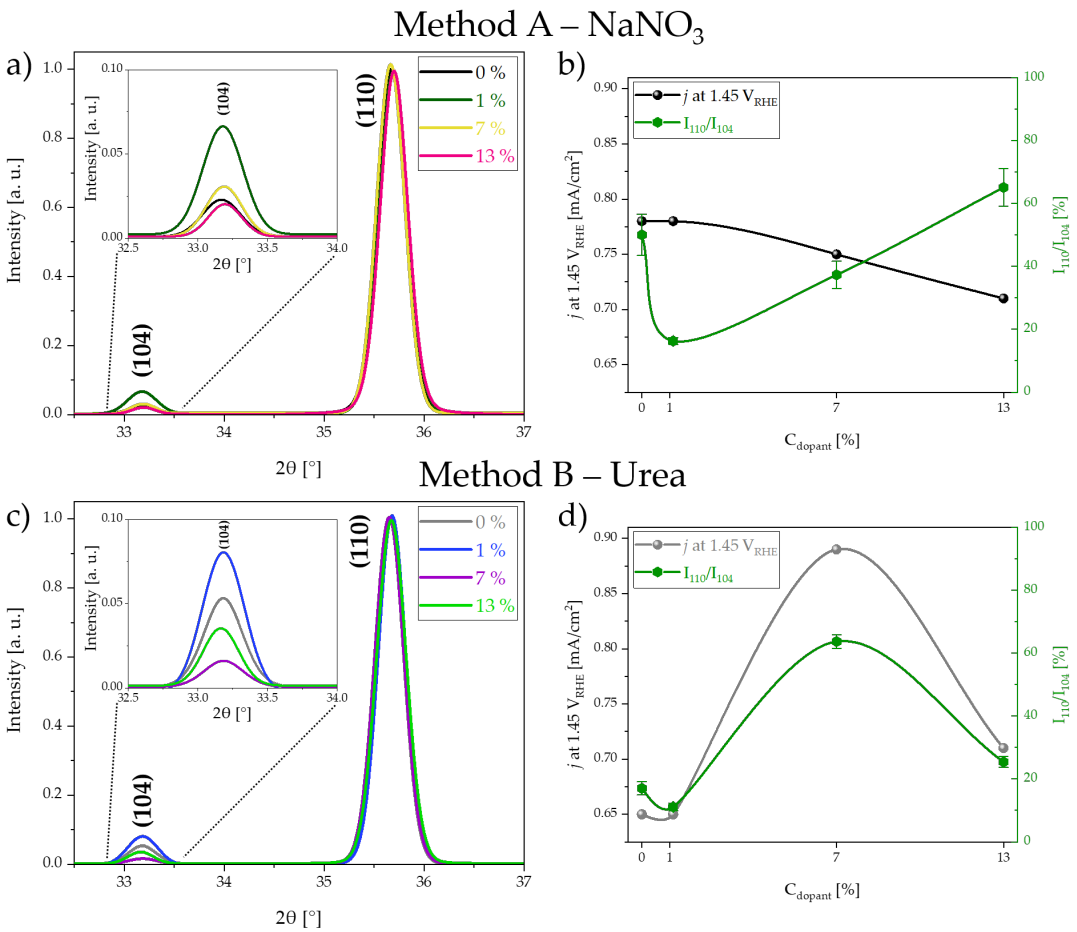

FIGURE 3.5: Pseudo-Voigt fits of XRD (110) and (104) experimental peaks, with the inset graph showing a higher magnification of peak (104). j and I_{110}/I_{104} relation as a function of Mn C_{dopant}. (a) and (b) correspond to the synthesis with method A, while (c) and (d) correspond to method B.

to own an anisotropic conductivity with four orders of magnitude higher than the perpendicular direction [44, 91, 148, 149]. On the other hand, the peak of (104) plane is usually associated with the existence of oxygen vacancies, which act as electron trapping sites and recombination centres. Thus, superior values of the intensities ratio between the (110) peak and the (104) peak (I_{110}/I_{104}) lead to j improvements [147, 148]. In fact, a clear correlation between I_{110}/I_{104} ratios and j as a function of the Mn C_{dopant} of method B is observed (Figure 3.5(b)), where the best j was attained for 7 % Mn-doped sample. On the other hand, even though 1 % doping showed lower I_{110}/I_{104} ratios than bare hematite, their j responses were the same. The higher contribution of the (104) plane signal on these samples (1 %) might be related to the cathodic shift in V_{onset} observed in PEC measures, as this plane has been associated with the surface states increase that trap the photogenerated holes in the hematite/electrolyte interface, making them available to the water oxidation reaction [147]. Moreover, the non-correlation of the I_{110}/I_{104} high ratio of

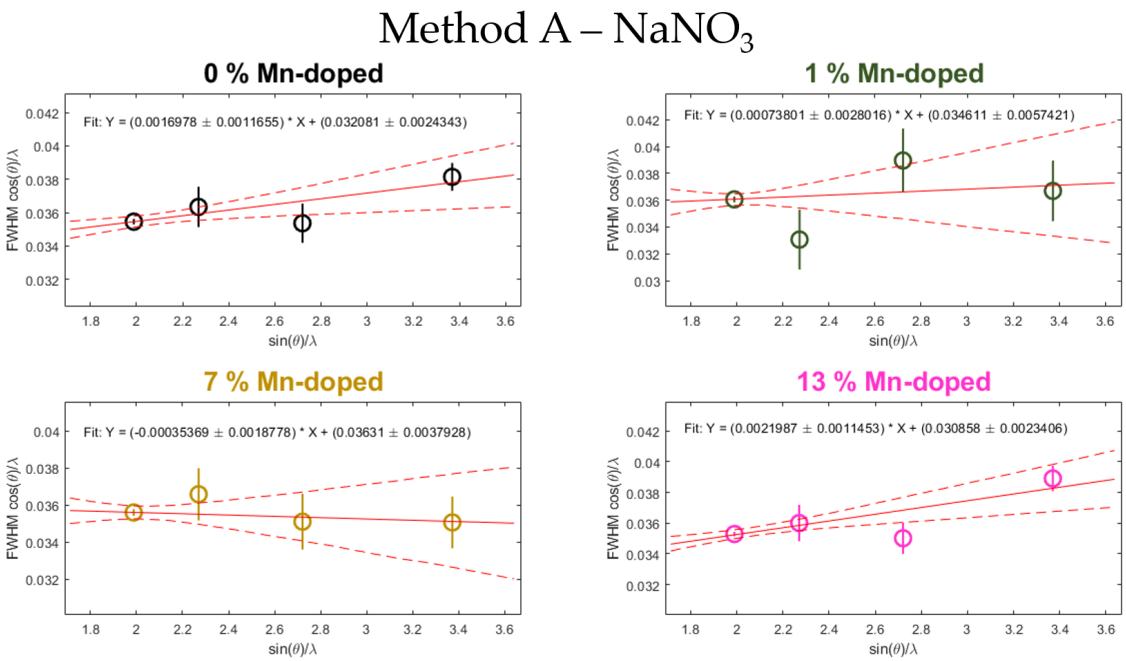

FIGURE 3.6: Linear fits using the Williamson-Hall relationship for Mn doped samples synthesized by method A (with $NaNO_3$).

13 % Mn-doped sample in method A with an expected high j can arise from an excess of dopant ions, which was found to increase surface irregularities and form a resistant oxide layer on the hematite surface, which blocks the hole transport, thus decreasing the PEC performance [147].

In addition, the crystallite size (D_{XRD}) and microstrain (ε) were estimated from diffraction peak broadening analysis. Firstly, for each sample diffractogram the identified peaks of α-Fe_2O_3 were individually fitted for all prepared samples with a Pseudo-Voigt function (Equation A.1), as exemplified in Figure A.5 from Appendix A. Afterwards, D_{XRD} and ε were estimated by rearranging the Williamson-Hall (W-H) relationship (Equation 2.2).

Plot representation and linear regression of W-H analysis were performed in a home-made MATLAB code [150] developed by Dr. Sérgio Magalhães from Instituto Superior Técnico (IST), Lisbon. Figures 3.6 and 3.7 present the $w\cos\theta/\lambda$ *vs* $\sin\theta/\lambda$ plots for undoped and Mn-doped photoanodes prepared using method A ($NaNO_3$) and method B (urea). The linear regression equation took into account the uncertainties of the fitting parameters (Δw and $\Delta\theta$). The hyperbolic boundary curves were obtain by a Monte Carlo algorithm, assuming that errors are Gaussian and centred. The linear fit parameters and respective uncertainties were computed to a degree of confidence of 95 %. D_{XRD} and ε were determined through the intercept and slope of the linear fits, respectively (values displayed in Tables 3.3 and 3.4).

Figure 3.8(a) and (b) present the behaviour of D_{XRD}, D and j as a function of the Mn C_{dopant},

	Method A - $NaNO_3$			
Doping %	0	1	7	13
D_{XRD} [nm]	29.3 ± 2.2	27.2 ± 4.5	25.9 ± 2.7	30.5 ± 2.3
ε [%]	0.04 ± 0.03	0.02 ± 0.07	-0.01 ± 0.05	0.06 ± 0.03

TABLE 3.3: Crystallite size and microstrain of Mn-doped hematite NWs synthesized by method A.

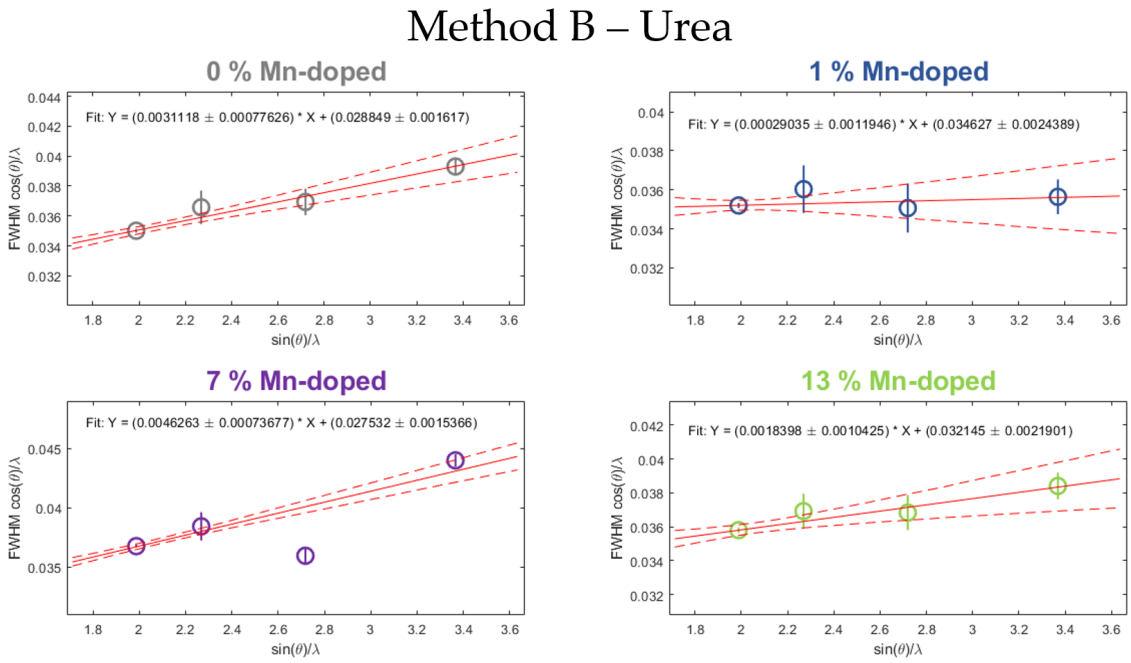

FIGURE 3.7: Linear fits using the Williamson-Hall relationship for Mn doped samples synthesized by method B (with urea).

	Method B - Urea			
Doping %	0	1	7	13
D_{XRD} [nm]	32.6 ± 1.8	27.1 ± 1.9	34.1 ± 1.9	29.2 ± 2.0
ε [%]	0.09 ± 0.02	0.01 ± 0.03	0.12 ± 0.02	0.05 ± 0.03

TABLE 3.4: Crystallite size and microstrain of Mn-doped hematite NWs synthesized by method B.

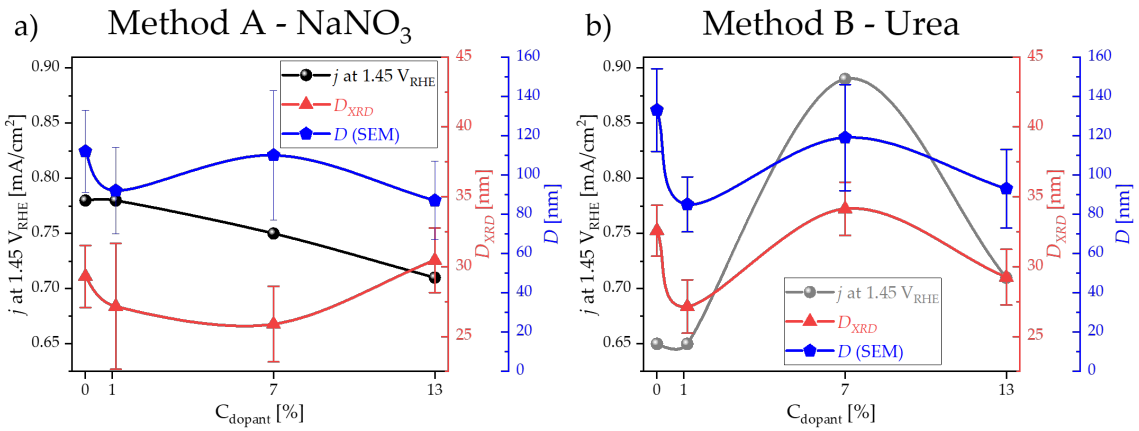

FIGURE 3.8: Photocurrent density (j), crystallite size (D_{XRD}) and NWs diameter (D) as a function of Mn C_{dopant} for (a) method A with $NaNO_3$ and (b) method B with urea.

for methods A ($NaNO_3$) and B (urea), respectively. Firstly, for method B, D_{XRD} followed a similar trend as D, while method A shows deviations for 7 % and 13 % samples. In this sense, both approaches A and B showed the same sharp decrease of D_{XRD} (and D) upon the introduction of 1 % Mn doping, as expected when introducing dopants on the crystalline structure of α-Fe_2O_3 NWs [26, 90, 143]. However, opposite effects were observed in j for larger crystallites shown for C_{dopant} = 7 % in method B (D_{XRD} = 30.5 ± 2.3 nm) and C_{dopant} = 13 % in method A (D_{XRD} = 34.1 ± 1.8 nm). While for the latter (13 %) j decreased, the former (7 %) j increased. Besides agreeing that an increased crystallinity quality (higher D_{XRD}) is a crucial factor for an enhanced j response, other contributions must be taken into consideration. In this case, the excess of doping (13 %) can be a limiting factor of the j performance, overcoming the good crystallinity structure.

Microstrain (ε) is usually correlated with structural lattice disordering, reflected by the local strain non-homogeneity due to lattice dislocations/distortions and grain surface relaxation [29]. Doping hematite can cause the occurrence of these phenomena [115, 151], leading to an increase of ε. However, when ε < 0.2 % in nanostructures, it can be considered negligible [29, 115, 152]. For all photoanodes, the ε was obtained in this range, hence not being significant for physical properties.

Rutherford Backscattering Spectrometry

Rutherford Backscattering Spectrometry (RBS) provides a detailed understanding of the in-depth profile of the photoanodes, allowing us to inspect how the doping atoms are distributed in the lattice matrix.

The RBS data is collected in channels (dimensionless) to further conversion into energy units. A calibration curve between the channels and respective energies is obtained by performing RBS measurements of well-known bulk films. In this case, three samples were used: (i) a film of AlGaN deposited on top of an alumina template – AlGaN/Al_2O_3-c, (ii) a double layer film of AlInN/GaN on top of an alumina template – AlInN/GaN/Al_2O_3-c, and (iii) a double layer film of GeSn/Sn on top of a silicon substrate – GeSn/Sn/Si.

The three calibration samples measured for each detector are presented in Figure A.6 at Appendix A. A licensed RBS calibration software from MROX [153] running in a MATLAB GUI was used to obtain the calibration curves for all detectors. Since only the atomic elements at the surface are used in the calibration, five atomic elements were used: Ga from sample (i), In and Al from sample (ii), Ge and Sn from sample (iii). The software uses the incident particle energy (E_0 = 2 MeV), detector backscattering angle (θ_i = +165, -140, and -165 °for detectors RBS1, RBS2 and ERD, respectively) and the atomic masses of the chosen elements and the incident particles (Table A.1 at Appendix A) to determine the backscattering energy (E_1) of each element through Equation 2.3. Then, the calibration curves are obtained by performing a linear fit to the backscattering energy *vs* channel plot of the identified atomic elements. Finally, the obtained calibration curves for each detector (plots and fits in Figure A.7 from Appendix A) are presented as follows:

- Detector RBS1: E = 2.1474 keV/Channel · Channel +85.8211 keV;
- Detector RBS2: E = 2.0809 keV/Channel · Channel +102.7885 keV;
- Detector ERD: E = 2.1118 keV/Channel · Channel +96.8880 keV;

The calibration curves allow the calculation of the backscattering energy at which a detector captures an atomic element located at the surface of the sample[1]. Since our samples are mainly composed of glass, a conductive film (FTO) and the semiconductor material (hematite and doping element Mn), the elements to trace are Si, Sn, Fe, O and Mn.

RBS spectrum measure the yield, i.e. backscatter rate, for each channel associated with the respective energy. When the incident $^4He^+$ (α) particles collide with a certain atomic element, a barrier appears at the backscattering energy detected. By numerical methods and simulations, the position and length of the barrier can define the distribution and thickness of the layer associated with the atomic element[2]. Figure 3.9 (a) shows the experimental RBS data with

[1] From now on, this will be called surface energy.

[2] In perspective, the ascent of the barrier being the beginning of the layer and the descent of the tilt the end of the layer.

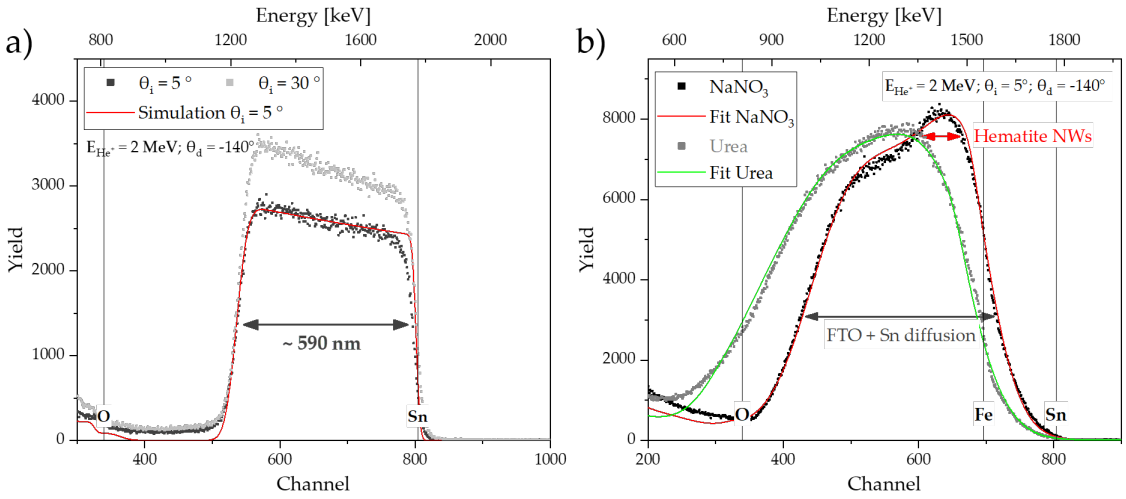

FIGURE 3.9: (a) RBS spectra of FTO substrate at two incident angles (θ_i = 5 °and 30 °), with simulation for 5 °incident angle. (b) RBS spectra of undoped hematite samples synthesized by method A (black) and method B (grey), with respective fits from NDF code.

the simulating curve of the FTO substrate (uniform, compact film), collected with the detector RBS2 at incidence angles of 5 and 30 °, with the surface energies for the atomic elements O and Sn that compose the FTO. The sharp rise of the Sn barrier at the Sn surface energy for both incidence angles confirms the Sn presence at the surface, as expected. Through simulations of the experimental data from the detector RBS2 at θ_i = 5 °on NDF code [133, 134], the thickness of the layer containing Sn depicted in Figure 3.9(a) was estimated at ~ 590 nm, in agreement with the FTO thickness measured from SEM images ($\overline{L_{\text{FTO}}}$ ~ 526 ± 22 nm) and literature studies [29].

When depositing a nanostructured film on top of the FTO substrate, RBS spectra is completely different. Figure 3.9 (b) represents the experimental RBS data and fitting curves of the undoped hematite samples from method A ($NaNO_3$) and method B (urea), collected with the detector RBS2 at an incidence angle of 5 °, with the surface energies for the atomic elements O, Fe and Sn composing the FTO + hematite. Firstly, a second barrier is identified around 1480 keV for method A and 1380 keV for method B, on top of the Sn barrier of the FTO. This additional barrier is associated with the Fe atomic element, thus, corresponding to the hematite NWs. Even though it is known that Fe is at the surface, its barrier only appears at much lower energy values, as a consequence of the energy loss resulting from the voids in the nanostructure, which causes the barriers to tilt.

The tilt of a barrier can be influenced by four factors: (i) energy resolution of the detector, (ii) variation of sample composition (different phases), (iii) increase of voids (porosity), which increases roughness and (iv) doping of hematite NWs (either by in-situ hydrothermal doping or Sn diffusion). The first hypothesis is discarded since the detector has an energy resolution

	Method A – $NaNO_3$			Method B – Urea		
Doping %	0	1	7	0	1	7
Surface $V_{fraction}$	0.82	0.85	0.88	0.89	0.86	0.86
In-depth $V_{fraction}$	0.50	0.75	0.88	0.89	0.86	0.86

TABLE 3.5: Volume fraction ($V_{fraction}$) at the surface layer and in-depth layer of the undoped and Mn-doped (1 % and 7 %) hematite NWs for both method A and B.

of 10 keV. The second is also discarded, as XRD proved that photoanodes have a single phase (α-Fe_2O_3 in photoanode and F:SnO_2 on FTO substrate). On the other hand, hypotheses 3 and 4 are valid candidates for tilting the barriers. As discussed in the previous chapters, the two-step thermal annealing conducted on the photoanodes led to a diffusion of Sn^{4+} from the FTO substrate into the hematite NWs [29, 45, 91], which can tilt the ascent of the Sn barrier. However, the tilt in the descent of the Sn barrier raises two other hypotheses: either the Sn is also diffused to the glass (which is not confirmed), or voids are present both in hematite and FTO layers. Since the two contributions could not be discriminated, the undertaken discussion of the Sn barrier equally involved both contributions, whereas the tilt of the Fe barrier was mainly associated with the presence of voids in the hematite NWs.

Concerning the number of voids, the slope of the tilt can qualitatively indicate the number of them, i.e. a high slope indicates the existence of fewer voids. Since method A ($NaNO_3$) presents a higher slope of both ascent and descent tilts than method B (urea), RBS spectra indicate that method B has more voids (thus higher porosity) than method A, both at the surface and in-depth of the photoanode. NDF code quantifies the rate of voids by a volume fraction estimation between 0 and 1 (Table 3.5) [133, 134]. NDF fits of experimental data displayed a volume fraction ($V_{fraction}$) of 0.82 for the bare hematite from method A, while method B achieved 0.89. Furthermore, the volume fraction in method A decreased to 0.5 at the in-depth profile of the sample, whereas in method B remained unchangeable, suggesting that method B promote uniform growth of NWs for the undoped hematite photoanodes. These remarks are in agreement with what was observed in the morphological characterization in Subsection 3.3.2.

RBS measurements were also performed on 1 % and 7 % Mn-doped samples for both methods A and B due to the improved V_{onset} and j characteristics reported by those samples. Figure 3.10 illustrates the experimental RBS data and fitting curves of the bare and Mn-doped (1 % and 7 %) hematite samples from both methods A (with $NaNO_3$) and B (urea), collected with the detector RBS2 at an incidence angle of 5 °, with the surface energies for the atomic elements O, Mn, Fe and Sn composing the FTO + hematite. Mn-doped samples (1 % and 7 %) from method

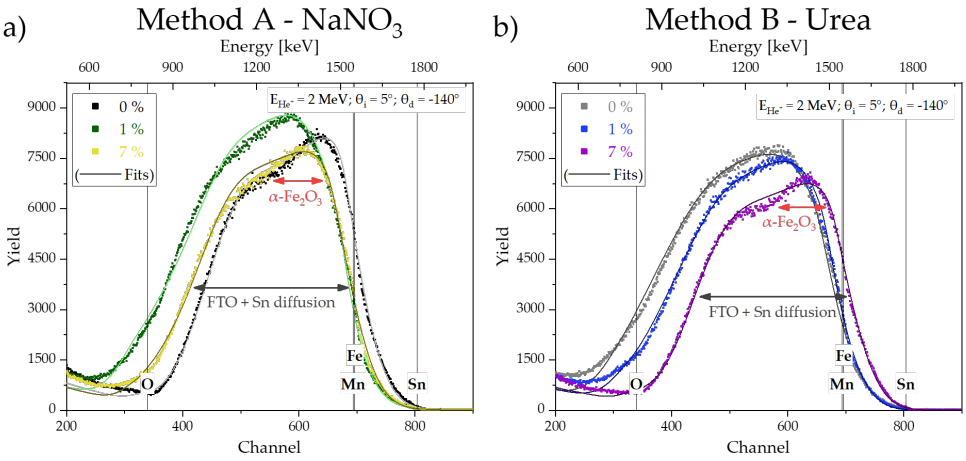

FIGURE 3.10: RBS spectra and respective fits of Mn-doped and undoped hematite samples synthesized with (a) method A ($NaNO_3$) and (b) method B (urea).

A presented a shift in the ascent of the Sn barrier to lower energies when compared to bare hematite. This is likely due to the fact that Mn doping limits the Sn diffusion from the FTO. Additionally, continuous Mn doping until 7 % lower the slopes of the Fe barrier, as shown by the increase in the volume fraction to 0.88 at the surface and in-depth, promoting uniform porosity along the photoanode. On the other hand, method B showed the opposite behaviour: the 7 % Mn-doped sample introduced a shift in the ascent of the Sn barrier to closer values of the Sn surface energy, possibly improving the Sn diffusion from the FTO, which increases hematite conductivity, as indicated by having the highest j of this set of samples. Therefore, it appears that the oxidizing agent determines whether the optimized doping of 7 % allows Sn diffusion (in method B) or not (in method A). Moreover, even though higher tilts of the Fe barrier were attained for 7 % doping in method B, thus presenting a lower porosity, the volume fraction remained the same (at 0.86) in the in-depth profile, offering a uniform NWs distribution, as shown in the morphological images (see Subsection 3.3.2).

Mn similar atomic mass as Fe associated with the low concentration on the sample made it impossible to visually distinguish the Mn dopant in the RBS spectra. Nevertheless, initial NDF fits proved the presence of a small percentage of the Mn atomic element along the α-Fe_2O_3 NWs. However, further fits are necessary to provide more accurate percentages and to determine the in-depth distribution of the Mn dopant.

3.3.4 Optical Characterization

Ultraviolet-Visible (UV-Vis) spectroscopy was performed to analyse the optical characteristic of all photoanodes. Figure 3.11 presents the absorption spectra of the photoanodes for both

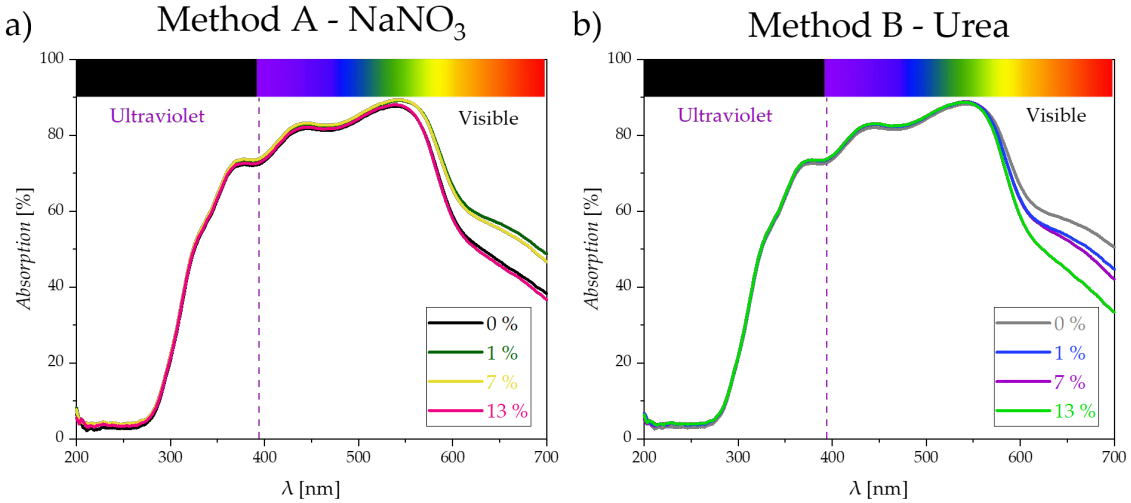

FIGURE 3.11: Absorption spectra of the undoped and Mn-doped α-Fe_2O_3 NWs synthesized by (a) method A with $NaNO_3$ and (b) method B with urea.

hydrothermal synthesis schemes (A and B). The typical absorption spectrum consists on determining the absorbance values, which are obtained from the reflectance and transmittance data (Equation 2.5)) without the FTO contribution, as a function of the incident radiation wavelength.

Generally, thin films of hematite display a maximum absorption peak around 400 nm [136, 146, 147], whereas mesoporous nanostructures display two absorption peaks at 375 and 535 nm [45]. In this study, all samples matched the typical absorption spectrum of hematite NWs [29], with a maximum absorption peak around 535 nm. Moreover, the different oxidation agents revealed distinct optical responses. While in method A, 1 % and 7 % Mn-doped samples exhibit a red-shift of the maximum absorption peak, method B did not yield significant changes in the absorption peaks. Red-shifts represent an increase in the absorption coefficient associated with the use of higher annealing temperatures or dopants [45], which were both applied to these photoanodes. Since all samples showed the maximum absorption peak around 535 nm, the overall red-shift is believed to arise from the Sn diffusion promoted by the two-step thermal annealing treatment [29, 45]. However, the additional shifts observed in method A ($NaNO_3$) for 1 % and 7 % Mn doping concentrations appear to be associated with the Mn doping impact on hematite NWs.

Since the photoanode absorption is strongly dependent on the thickness of the photoanode, the absorption coefficient (α) was calculated for each wavelength by, respectively, $\alpha = 2.303 \cdot A/L$, where A is the absorbance and L is the thickness of the photoanode. Table 3.6 displays the A and α at 535 nm, compared with the L from SEM, for all the prepared photoanodes. For

	Method A – $NaNO_3$				Method B – Urea			
Doping %	0	1	7	13	0	1	7	13
A [%]	87.6	88.9	89.2	88.0	88.1	88.6	88.7	88.6
L [nm]	378	566	450	389	684	341	265	379
α [nm^{-1}]	0.53	0.36	0.46	0.52	0.30	0.60	0.77	0.54

TABLE 3.6: Absorbance (A), photoanode thickness (L) and absorption coefficients (α) at 535 nm of the undoped and Mn-doped hematite NWs for both method A and B.

	Method A – $NaNO_3$				Method B – Urea			
Doping %	0	1	7	13	0	1	7	13
E_g [eV]	2.049	2.038	2.041	2.047	2.037	2.045	2.047	2.048
L [nm]	378	566	450	389	684	341	265	379

TABLE 3.7: Optical band gap energies (E_g) and photoanode thickness (L) of the undoped and Mn-doped hematite NWs for both method A and B.

both sets of samples, Mn doping induced a higher absorbance at the hematite NWs maximum peak. However, taking L into account, the α showed different behaviours for methods A and B. Whereas, in method A, the Mn doping decreased α, the L decrease observed in method B enhanced α. Even though it is usually described that thicker samples absorb more visible light [115], here we obtained an optimum absorption coefficient (α = 0.77) for the 7 % Mn-doped sample with the smaller L.

Further analysis was assessed by determining the band gap energy (E_g) of the photoelectrodes from the Tauc plots [140] through Equation 2.6. Figure 3.12 represents the Tauc plots of both sets of samples according to the oxidation agent ($NaNO_3$ or urea). Since we indirect electronic transitions were considered, Tauc plots consisted on the indirect absorption coefficient (α_{ind}) calculated by $\alpha_{ind} = (\alpha \cdot h\upsilon)^{1/2}$, plotted against the incident photon energy ($h\upsilon$). The x-interception of the linear adjusts presented in Figure 3.12 provide the band gap value. Table 3.7 shows that, once again, distinct behaviours were observed according to the oxidation agent. Mn doping with $NaNO_3$ (method A) lowered the semiconductor band gap, while urea (method B) led to an increase in the hematite band gap. The large L of the photoanodes seemed to play an important role in lowering E_g, as the largest samples (1 % Mn-doped hematite in method A and bare hematite in method B) presented the smaller band gap energies (2.038 and 2.037 eV, respectively).

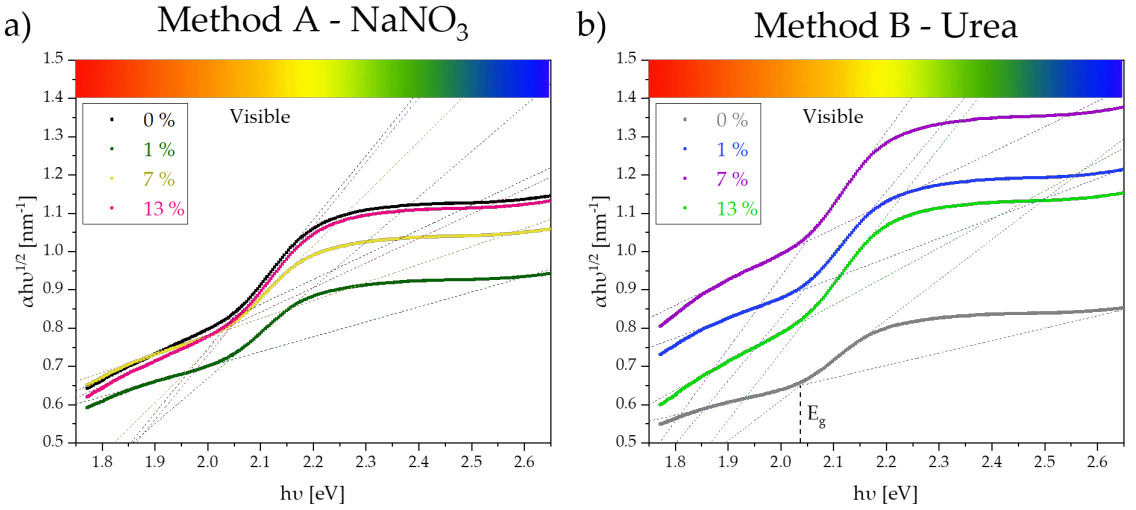

FIGURE 3.12: Tauc plots of Mn-doped α-Fe_2O_3 NWs synthesized by (a) method A with $NaNO_3$ and (b) method B with urea.

3.3.5 Conclusions

In this chapter, the impact of the oxidation agent applied on the synthesis of hematite NWs was studied by applying two hydrothermal methods: method A with sodium nitrate ($NaNO_3$) and method B with urea (CH_4N_2O) as the oxidation agent. Undoped and Mn-doped hematite NWs were prepared by both approaches, examining the Mn doping concentration for 1, 7 and 13 %, according to the doping range from literature studies [94, 95]. An important conclusion was that the photoanode PEC performance is influenced by the combination of different factors, such as an enhanced morphology, an enriched crystalline structure, the promotion of Sn diffusion from the FTO substrate and a well-adjusted optical band gap. Therefore, to assess a photoanode performance, it is important to consider the contribution of all different parameters.

Generally, the oxidation agent was found to highly impact the properties of the synthesized bare and Mn-doped hematite NWs. Comparing the bare hematite photoanodes from both methods, the higher j response from method A (0.78 mA·cm^{-2} at 1.45 V_{RHE}) was attributed to an improved conductivity provided by the higher Sn diffusion and smaller thickness, with NWs preferentially growing in the (110) plane. These properties overcame the NWs aggregation observed in SEM images of method A, yielding fewer voids along the hematite NWs layer as concluded by RBS measurements. Moreover, although a higher absorption and lower band gap value was obtained in method B, the large thickness must have suppressed the transport of the photogenerated charge carriers [115, 145], leading to a j of only 0.65 mA·cm^{-2} (1.45 V_{RHE}).

Low Mn doping (1 %) offered the same j response as bare hematite NWs for both approaches, however, explained by different sources. For instance, in method A, while the enhanced j of bar

hematite came from a higher Sn diffusion and smaller thickness of NWs preferentially growing in the (110) plane; in 1 % Mn-doped samples the *j* was explained by the higher absorption spectra and smaller band gap energy ($E_g \sim 2.038$ eV), which increased the available radiation to induce photogenerated charge carriers. Additionally, both sets of samples from method A ($NaNO_3$) and B (urea) showed remarkable cathodic shifts of the V_{onset}, associated with the rise of the (104) plane contribution in XRD diffractograms [147], thus lowering the I_{110}/I_{104} ratio. Respectively, shifts of 70 mV and 60 mV, obtained for method A ($NaNO_3$) and method B (urea) compared with bare hematite photoanodes, were much higher than the ones obtained in literature [94, 95]; and resulted in a close V_{onset} ($\sim 0.67\ V_{RHE}$) approximation to the ideal hematite photoanode V_{onset} ($\sim 0.4\ V_{RHE}$).

Further doping (7 % and 13 %) decreased the *j* response in method A. On the other hand, in method B, 7 % doping led to the highest *j* performance of 0.89 mA·cm^{-2} at 1.45 V_{RHE} attained in this study. The combination of 7 % doping with urea as the oxidation agent promoted the growth of uniform dispersed NWs in the preferential [110] axis vertical to the FTO substrate, presenting an enhanced crystallinity quality with fewer lattice defects and small thickness ($L \sim 265$ nm). Additionally, RBS measures suggested that the 7 % Mn dopant promoted a higher Sn diffusion, while UV-Vis spectroscopy showed that Mn increased the absorption of hematite NWs, with the highest absorption coefficient being reached for 7 % Mn-doped sample from method B.

All things considered, method A with $NaNO_3$ as the oxidation agent achieved the best *j* performance and properties features between the bare hematite photoanodes. The introduction of the Mn dopant showed no *j* improvements in method A, whereas method B, with urea as the oxidation agent, achieved a 37 % increase in *j* response compared to the respective bare hematite photoanode. Furthermore, low doping concentrations (1 %) proved to be beneficial in the decrease of V_{onset}, reaching cathodic shifts of 70 mV and 60 mV for method A ($NaNO_3$) and method B (urea), respectively.

Chapter 4

Unveiling the Oxidation Agent Effect on Cobalt-doped Hematite Nanowires

4.1 Overview

Sitting at the left of Fe in the periodic table, Cobalt (Co) has also been listed as a dopant candidate for hematite, with several applications. For instance, Deshmane et al. developed cobalt oxide doped hematite films by a screen printing method as a petrol vapour sensor, achieving sensitivities of 84 % at 250 °C for 1 wt % Co oxide doping [154]. Additionally, Co-doped hematite nanospheres were applied in the heterogeneous activation of peroxymonosulfate (PMS) leading to an improvement in the degradation of p-hydroxybenzoic acid (p-HBA) [155].

Regarding the development of photoelectrochemical (PEC) cells, the novel hydrothermal strategy developed by Xi et al. with urea as the oxidation agent was employed in the synthesis of in-situ Co-doped hematite NRs, obtaining a j of 1.20 mA·cm^{-2} at 1.23 V_{RHE} with a reasonable faradaic efficiency of 78.43 %, which means an effective j of 0.94 mA·cm^{-2} at 1.23 V_{RHE} [92]. Along with a ~ 40 mV cathodic shift on the onset potential, these PEC improvements were attributed to the catalytic effect of the Co_3O_4 nanoparticles and an increase in the absorption spectrum. On the other hand, using the former hydrothermal synthesis with $NaNO_3$ as the oxidation agent, Wang et al. developed Co-doped α-Fe_2O_3 NRs with an unusual annealing step (800 °C for 3 min) [100]. Although they reported an increase in j, its absolute values remained low (0.55 mA·cm^{-2} at 1.23 V_{RHE}), probably due to the quick annealing undertaken. Even so, a substantial cathodic shift of V_{onset} (~ 70 mV) was noted, cementing the cobalt effect of lowering the photoanode dependence on external energy sources. Table 4.1 summarizes the PEC features

Reference	Oxidation agent	Co doping concentration [%]	*j* at 1.23 V_{RHE} [mA·cm^{-2}]	V_{onset} [V_{RHE}]	V_{onset} shift [mV]
Xi et al. [93]	urea	5	1.20	0.66	~ 40
Wang et al. [100]	$NaNO_3$	3	0.55	0.73	~ 70

TABLE 4.1: Photoelectrochemical performance features of Co-doped hematite nanorods (NWs) studies from literature.

reported in the literature. On top of these, Kwong et al. revealed that Co doping provided a balanced optimization and long-term durability of electrocatalytic water oxidation (OER) in highly acidic media [156].

Even though studies with both synthesis methods were performed on Co-doped hematite NRs, the duration of the hydrothermal method and the thermal annealing treatment applied were different from each other. For instance, while Xi et al. used a hydrothermal stage of 8 h at 100 °C, followed by two-stage annealing at 550 °C for 2 h + 800 °C for 20 min [93]; Wang et al. performed a hydrothermal stage of 6 h at 100 °C, followed by single stage annealing at 800 °C for 3 min [100]. The non-methodical variation of several parameters at the same time makes it impossible to establish the effects the oxidation agents had on hematite NRs.

In this chapter, the systematic and multifaceted study developed in Chapter 3 was applied with Co doping on hematite NWs developed by hydrothermal route. Therefore, Co-doped hematite nanowires were synthesized by combining the variation of two parameters: (i) the oxidation agent of the hydrothermal solution and (ii) the concentration of the Co dopant. The oxidation agent used to oxidize to Fe^{3+} precursor in the hydrothermal treatment was tested with $NaNO_3$ (method A) and urea (method B). Secondly, the doping concentration of Co was tested for 1 and 7 %, according to the doping range from literature studies [93, 100].

4.2 Experimental Details

Co-doped hematite photoanodes were prepared by a hydrothermal method (Subsection 2.1.3 of Chapter 2). The FTO glass substrates were cleaned by the methodology described in Subsection 2.1.2 and placed in a 25 mL stainless-steel autoclave filled with a 20 mL chemical solution made according to two approaches: method A – 0.15 M $FeCl_3{\cdot}6H_2O$ + 1 M $NaNO_3$ (oxidation agent) + 56 μL HCl; method B – 0.15 M $FeCl_3{\cdot}6H_2O$ + 0.15 M CH_4N_2O (oxidation agent).

Afterwards, a first hydrothermal stage of 50 min at 95 °C with the undoped solution was performed to deposit a uniform undoped β-FeOOH layer (Subsection 2.1.3). Then, the amount

	Synthesis Method	
	Method A – $NaNO_3$	Method B – Urea
Doping Concentration [%]	0 1 7	0 1 7

TABLE 4.2: Co-doped and undoped hematite samples prepared.

of $Co(NO_3)_2{\cdot}6H_2O$ (1 and 7 % in relation to the Fe^{3+} concentration) was added to the solution for the second stage of 13 h at 95 °C, merging with the undoped solution to dope the β-FeOOH NWs with Co^{2+}. This 2nd stage was performed on both methods (A and B), obtaining the two groups of samples presented in Table 4.2. Finally, a thermal annealing treatment at 550 °C for 2 h (10 °C/min ramp) and 800 °C for 20 min (8 °C/min ramp) was conducted on all samples to convert the as-prepared β-FeOOH phase into the stable hematite phase (Subsection 2.1.3) [29]. The bare hematite photoanode of method A ($NaNO_3$) was the same as in Chapters 3 and 4.

Summarizing, three samples according to the concentration of Co dopant (0, 1 and 7 %) were synthesized for both methods A (with $NaNO_3$) and B (with urea) to allow a methodical analysis of not only the oxidation agents but also the doping concentration impact on hematite NWs.

4.3 Results and Discussion

4.3.1 Photoelectrochemical response

Photocurrent density-voltage (j-V) curves under dark and simulated sunlight are presented in Figure 4.1(a) and (b). For both sets of samples, the photocurrent density (j) at 1.45 V_{RHE} and the onset potential (V_{onset}) were extracted from j-V curves and plotted against the Co doping concentration (C_{Co}) in Figure 3.1(c) and (d), respectively. Generally, samples prepared with method A ($NaNO_3$) achieved higher j than the ones prepared with method B (urea). On the other hand, V_{onset} reported the opposite trend, with the oxidation agent urea leading to more favourable values than $NaNO_3$. Moreover, Co doping led to lower V_{onset} in both methods A and method B when compared with the respective bare hematite photoanodes. In detail, low doping concentrations (1 %) negatively impacted the j response, inducing a slight decrease from 0.78 to 0.75 mA·cm^{-2} (1.45 V_{RHE}) in method A ($NaNO_3$) and a sharper decrease from 0.65 to 0.48 mA·cm^{-2} (1.45 V_{RHE}) in method B (urea). However, further doping (7 %) in method A did not change the

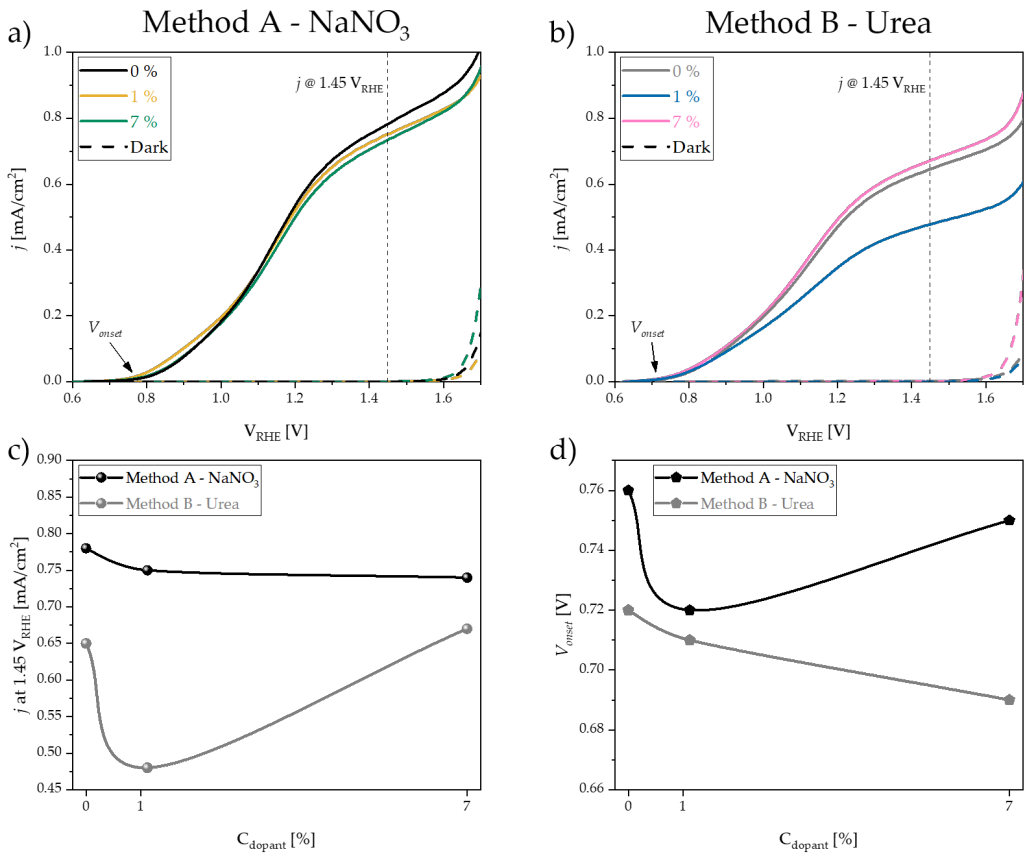

FIGURE 4.1: Photocurrent density-voltage characteristic curves of the Co-doped hematite nanowires according with the synthesis method: (a) method A with $NaNO_3$ and (b) method B with urea. (c) j at 1.45 V_{RHE} and (d) V_{onset} for the different synthesis methods as a function of doping concentration (C_{dopant}).

j value, while method B increased j to a similar value as bare hematite (0.67 mA·cm^{-2} at 1.45 V_{RHE}).

Overall, method A ($NaNO_3$) reported similar j values for bare and Co-doped photoanodes with an average j value of 0.76 mA·cm^{-2} at 1.45 V_{RHE} (black line and dots in Figure 4.1(c)), as observed in Chapter 3. On the other hand, method B (urea) presented to be sensitive to low Co (1 %) presence in hematite NWs (grey line and dots in Figure 4.1(c)), with an average j value of 0.60 mA·cm^{-2} at 1.45 V_{RHE}. In terms of j performance, photoanodes synthesized by method A ($NaNO_3$ presented higher performance than method B (Urea), concluded by the average j values of $\overline{j_A} \sim 0.76$ and $\overline{j_B} \sim 0.60$ mA·cm^{-2} at 1.45 V_{RHE}, respectively.

In terms of the onset potential, samples with 1 % Co doping prepared either with the A or B approach led to lower V_{onset} when compared with the undoped hematite sample (Figure 4.1(d)). However, the lowest V_{onset} of 0.69 mV was achieved with 7 % doping in method B. For each set of samples of methods A and B, respectively, the largest V_{onset} shifts compared to bare hematite

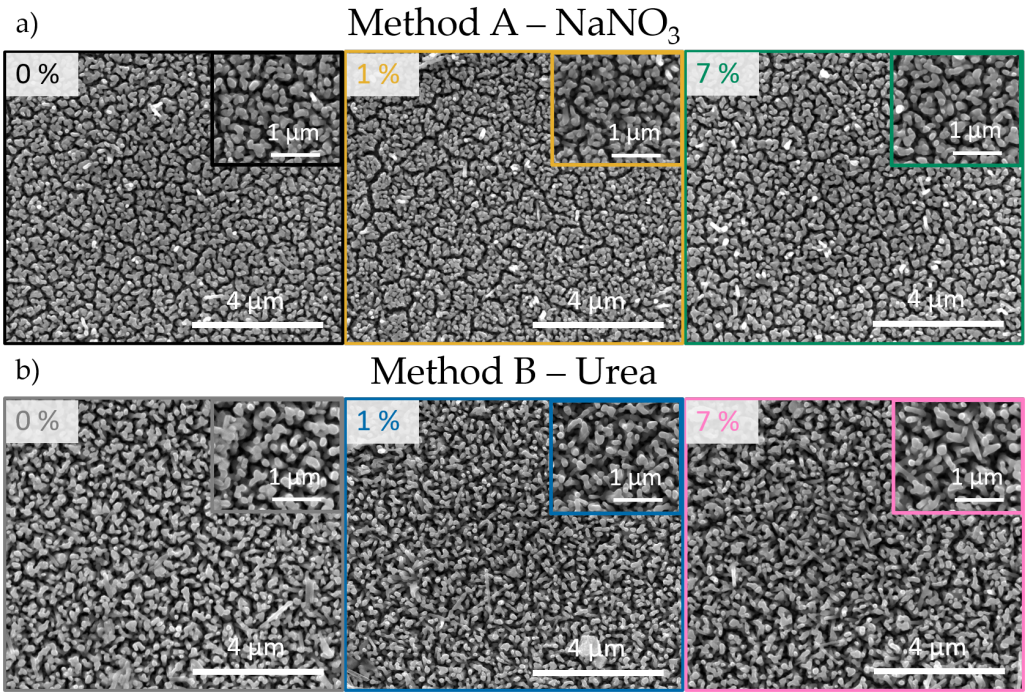

FIGURE 4.2: Scanning electron microscopy top-section images of Co-doped α-Fe_2O_3 NWs synthesized by (a) method A with $NaNO_3$ and (b) method B with urea. Inset figures show a closer look of the photoanodes' NWs.

were obtained by the Co doping concentrations (C_{Co}) of 1 % (~ 40 mV) and 7 % (~ 30 mV).

4.3.2 Morphological Characterization

The morphology of the developed photoanodes was accessed through top and cross-section SEM images. Figure 4.2 proved the synthesis of a nanowires morphology on top of the FTO substrates for all samples prepared by both methods A and B. The euhedral shape of some NWs was observed, rising from the fusion between neighbouring NWs promoted by the second annealing step up to 800 °C [29]. As observed in Chapter 3, method A ($NaNO_3$) promoted higher aggregation of NWs than method B (urea). The introduction of Co doping in both methods kept this same feature as the respective bare hematite photoanodes. Moreover, the diameter (D) of the NWs was measured on top-section SEM images (Figure 4.2) and plotted against the C_{Co} in Figure 4.3(a). Generally, a similar trend was observed between approaches, with method B (urea) leading to thicker NWs. Introducing the Co dopant, 1 % doping in both methods lowered the NWs diameter (D), while further doping to 7 % resulted in similar D as respective bare hematite photoanodes for both approaches.

Furthermore, the NWs thickness (L) was measured on the cross-section SEM images (Figure A.3 in Appendix A) for all the photoanodes prepared by both approaches. Once again, L

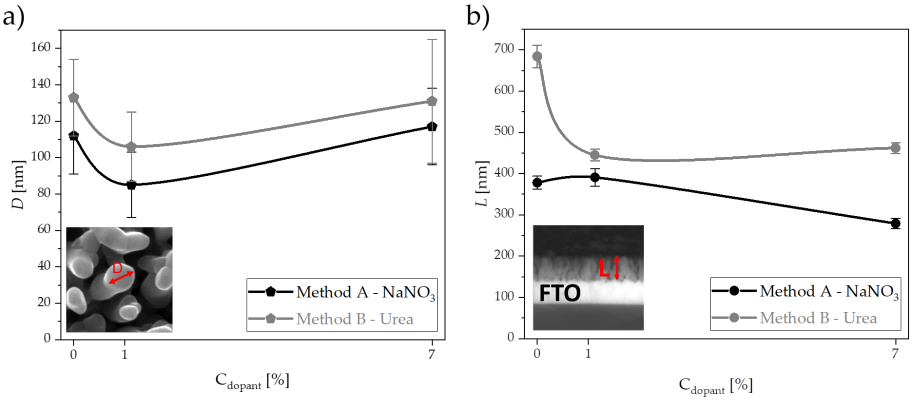

FIGURE 4.3: (a) Diameter (D) and (b) thickness (L) of Co-doped α-Fe_2O_3 NWs as function of doping concentration (1 – 7 %).

showed different behaviours by altering the oxidation agent in the hydrothermal synthesis as the doping concentration increased. While in method A, the overall L remained almost unchanged ($\overline{L_A} \sim 349$ nm ± 10), Co doping induced a sharp decrease from 684 ± 27 nm to 445 ± 14 nm with 1 % doping. Taking D and L into consideration, the thinner NWs (smaller D) with shorter thickness (shorter L) obtained by method A ($NaNO_3$) led to a higher $\overline{j_A} \sim 0.76$ mA·cm^{-2} (1.45 V_{RHE}) compared with the lowest $\overline{j_B} \sim 0.60$ mA·cm^{-2} (1.45 V_{RHE}) from method B.

4.3.3 Structural Characterization

X-Ray Diffraction

X-Ray Diffraction patterns (Figure 4.4) proved the synthesis of the thermodynamically stable hematite phase (JCPDS 33-0664) on all the prepared photoanodes. For both methods A ($NaNO_3$) and B (urea), the preferential orientation occurred at the plane (110), which, as seen in Chapter 3, is associated with a higher conductivity [44, 91, 148, 149]. Smaller peaks from planes (012), (104), (113), (024), (214) and (300) also were identified. No peaks related to Co doping were detected since the doping concentration in the material is lower than the diffractometer detection limit. Nevertheless, the analysis of the (104) and (110) peaks showed that Co doping induces peak shifts, which can relate to lattice expansions or contractions if the shift occurs for lower or higher angles, respectively [147]. Specifically, in method A, the (104) and (110) peak positions were shifted to higher angles (inset graph of Figure 4.5(a)), indicating a lattice contraction upon Co doping. In method B, doping with 1 % induced shifts to higher angles, while 7 % led to a slight shift to lower angles (inset graph of Figure 4.5(c)). Overall, shifts to higher angles were observed in samples that showed a decrease in j compared to respective bare hematite (1 % and

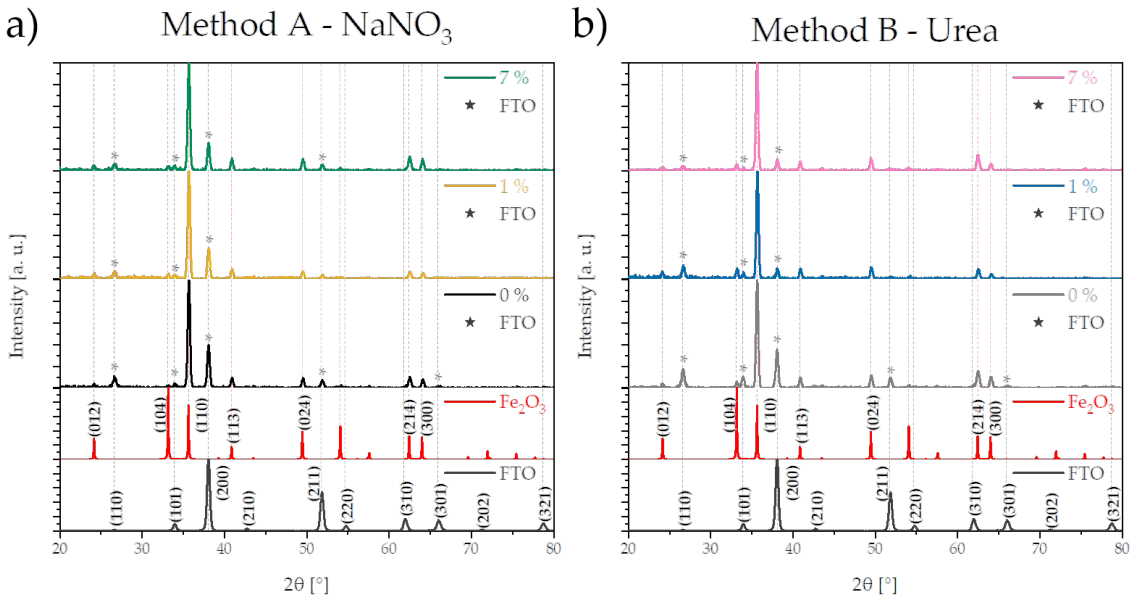

FIGURE 4.4: X-Ray Diffraction patterns of Co-doped α-Fe_2O_3 photoanodes synthesized by (a) method A with $NaNO_3$ and (b) method B with urea.

7 % from method A and 1 % from method B); whereas the slight shift to lower angles observed in 7 % from method B led to a slight increase in j to 0.67 mA·cm^{-2} at 1.45 V_{RHE}.

Moreover, the relation between the ratio of the intensity of the (110) peak and (104) peak (I_{110}/I_{104}) with the j is evaluated in Figure 4.5. For both sets of samples, Co doping increased the contribution of the (104) plane with the exception for 7 % Co-doped hematite from method B. The decrease of the I_{110}/I_{104} ratio was followed by a decrease in j performance. However, these samples presented enhanced V_{onset} as the increase of (104) plane has been associated with an increase in surface states that trap the photogenerated holes in the hematite/electrolyte interface, making them available to the water oxidation reaction [147].

Finally, peak broadening analysis allowed us to estimate the crystallite size (D_{XRD}) and microstrain (ε), as described in Chapters 2 and 3. Figure 4.6 present the $w\cos\theta/\lambda$ *vs* $\sin\theta/\lambda$ plots for undoped and Co-doped photoanodes prepared using method A ($NaNO_3$) and method B (urea). Plot representation and linear fitting were performed in a MATLAB code [150], which plots the experimental data, linear fit and error curves based on a degree of confidence of 95 %. Then, D_{XRD} and ε were determined through the intercept and slope of the linear fits, respectively (values displayed in Tables 4.3 and 4.4). Microstrain was again < 0.2, thus was considered negligible [29, 115, 152].

Figure 4.7(a) and (b) present the behaviour of D_{XRD}, D and j as a function of the different C_{Co} synthesized by methods A and B, respectively. It was observed that the crystallite size

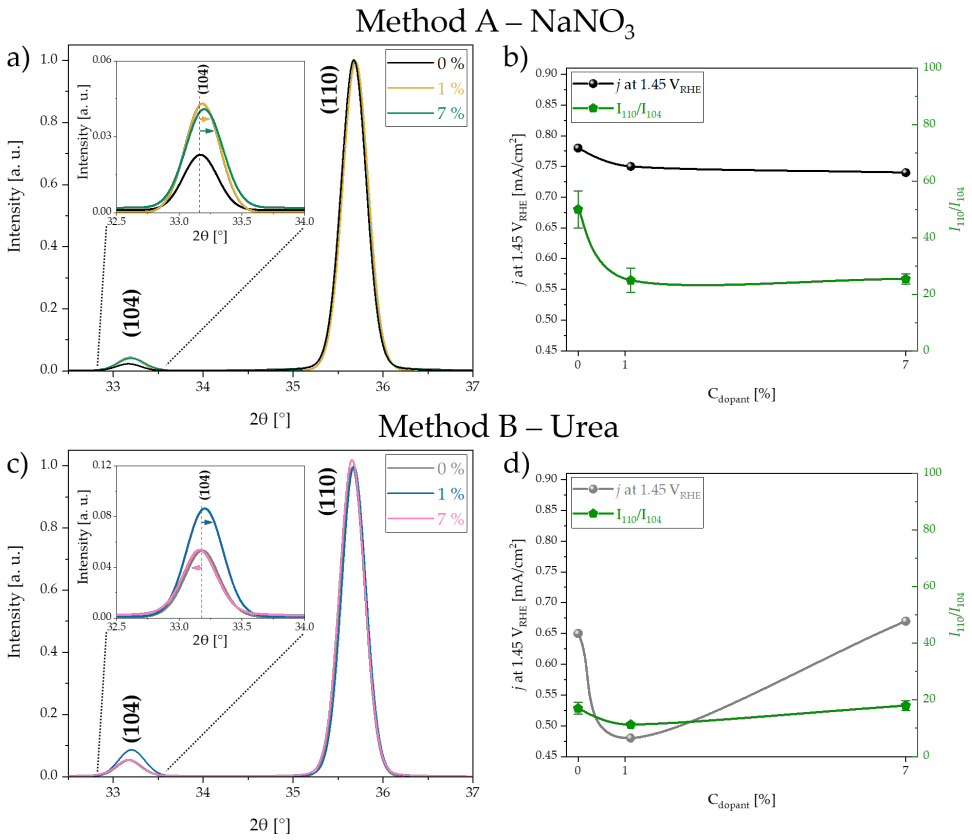

FIGURE 4.5: Pseudo-Voigt fits of XRD (110) and (104) experimental peaks, with inset graph showing a higher magnification of peak (104). j and I_{110}/I_{104} relation as a function of Co doping concentration. (a) and (b) correspond to the synthesis with method A, while (c) and (d) correspond to method B.

	Method A - $NaNO_3$		
Doping %	0	1	7
D_{XRD} [nm]	29.3 ± 2.2	29.6 ± 2.6	29.3 ± 2.1
ε [%]	0.04 ± 0.03	0.06 ± 0.03	0.05 ± 0.03

TABLE 4.3: Crystallite size (D_{XRD}) and microstrain (ε) of Co-doped hematite NWs synthesized by method A.

in method A remained constant along Co doping concentration, while in method B decreased when the dopant was introduced. Generally, a correlation was obtained between the D_{XRD} and j response for both sets of samples, except for 7 % Co-doped hematite with method B. Therefore, we can conclude that the D_{XRD} is one of the factors that contribute to the j performance of the photoanodes.

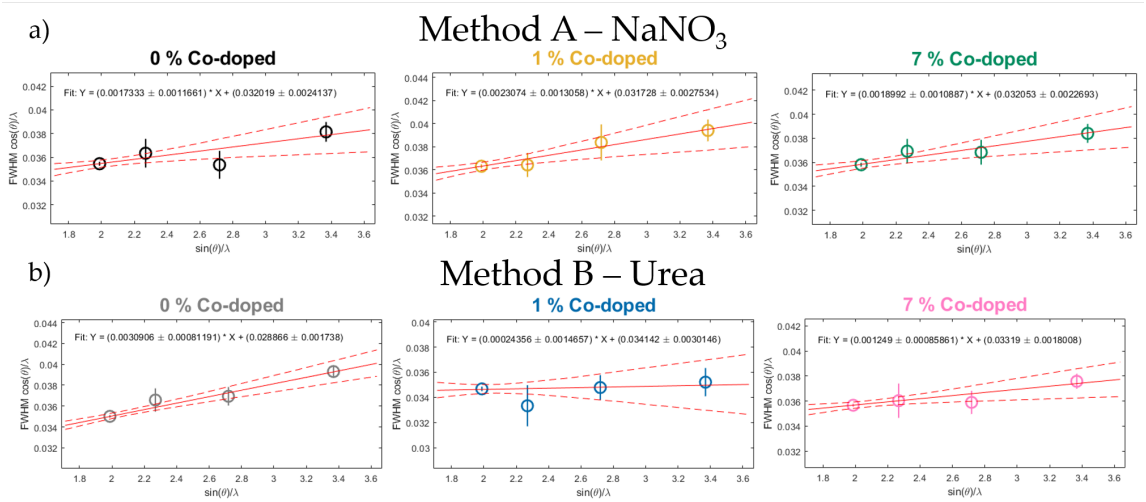

FIGURE 4.6: Linear fits using the Williamson-Hall relationship for Co doped samples synthesized by (a) method A with $NaNO_3$ and (b) method B with urea.

	Method B - Urea		
Doping %	0	1	7
D_{XRD} [nm]	32.6 ± 1.8	27.5 ± 2.4	28.3 ± 1.5
ε [%]	0.09 ± 0.02	0.01 ± 0.04	0.03 ± 0.02

TABLE 4.4: Crystallite size (D_{XRD}) and microstrain (ε) of Co-doped hematite NWs synthesized by method B.

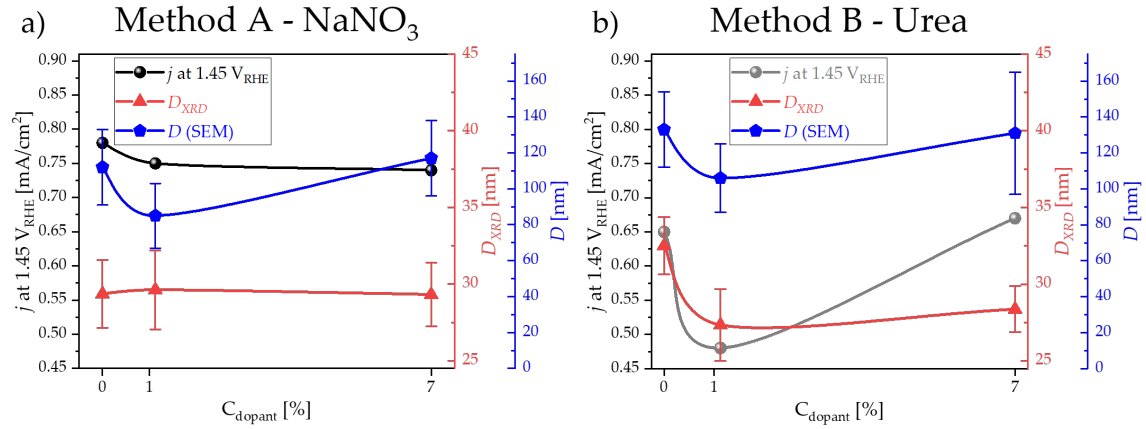

FIGURE 4.7: Photocurrent density (j), crystallite size (D_{XRD}) and NWs diameter (D) as a function of C_{Co} for (a) method A with $NaNO_3$ and (b) method B with urea.

Rutherford Backscattering Spectrometry

Rutherford Backscattering Spectrometry was performed on 1 % Co-doped hematite samples to further understand the principles of the notable variations in PEC performance and morphology achieved compared with the respective bare hematite samples. The setup was described in

Chapter 2, with measurements performed in the same conditions as for Mn doping in Chapter 3. Therefore, the calibration curves obtained in Chapter 3 (Figures A.6 and A.7 in Appendix A) are also applied here.

Figure 4.8(a) and (b) represents the experimental RBS data and fitting curves of the undoped and 1 % Co-doped hematite photoanodes from method A ($NaNO_3$) and method B (urea), respectively. At first sight, it is possible to notice the difference in RBS spectra obtained for the two groups of samples. Both analysed samples from method A showed a well-defined Fe barrier (with high slope tilts), suggesting the existence of fewer voids along the hematite NWs. On the other hand, the large tilts verified in method B indicate a larger presence of voids, both at the surface and in-depth of the photoanodes. This was confirmed by the volume fraction estimated by NDF fits: 0.82 in method A and 0.85 in method B for 1 % Co-doped hematite NWs (also verified for bare hematite in Chapter 3). Moreover, samples synthesized with $NaNO_3$ as the oxidation agent presented an initial ascent of their Sn barriers closer to the Sn surface energy, suggesting a higher Sn diffusion from the FTO to the hematite NWs, which could have benefited the higher *j* performance achieved by these photoanodes. As for the RBS measurements in Mn-doped hematite NWs, Co similar atomic mass as Fe associated with the low concentration on the sample made it impossible to visually distinguish the Co dopant in the RBS spectra. Nevertheless, initial NDF fits proved the presence of a small percentage of the Co atomic element for the 1 % Co-doped α-Fe_2O_3 NWs. However, further fits are necessary to provide more accurate percentages and to determine the in-depth distribution of the Mn dopant.

NDF code estimates the thickness of the detected elements, according to their barriers. Values obtained for the presence of Sn were in accordance with the mean thickness value of the FTO substrate ($\overline{L_{FTO}} \sim 526 \pm 22$ nm) plus the Sn diffusion length into the hematite structure. However, thickness values obtained for α-Fe_2O_3 were significantly lower than the ones obtained by SEM images. The reason behind this falls on α-Fe_2O_3 being nanostructured, while the NDF code is set for bulk films. RBS established unit is at/cm^2, so the thickness in nanometers is given by dividing the thickness (in at/cm^2) with the material density (in at/cm^3). As a result of using the α-Fe_2O_3 density for bulk material, the thickness values in nanometers are lower than expected (nanostructure material has a lower density which leads to higher estimated thickness). Even so, since the density used was the same on all samples, comparisons between them are valid. Hence, the thickness variations between samples determined by NDF fits of RBS spectra correlated with the *L* from SEM.

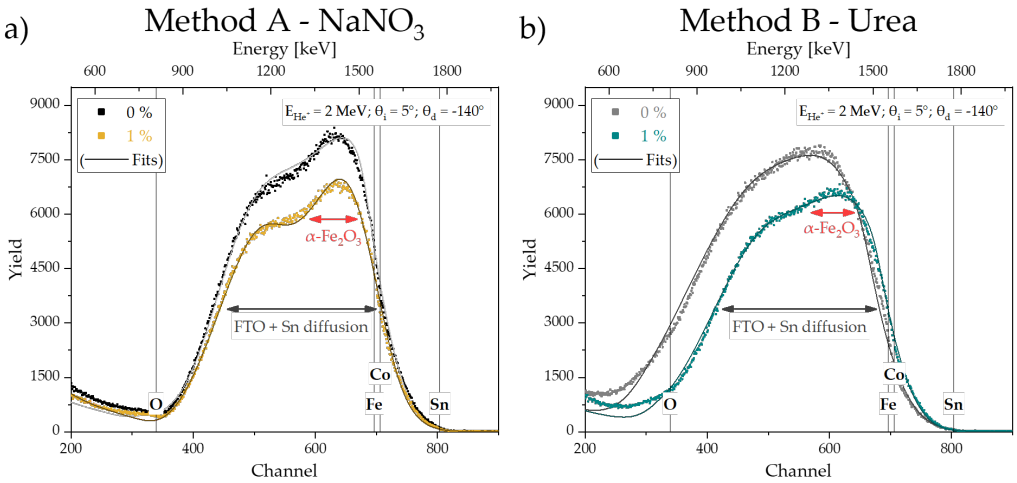

FIGURE 4.8: RBS spectra of undoped and 1 % Co-doped hematite samples synthesized by (a) method A and (b) method B, with respective fits from NDF code. Barriers correspondent to FTO substrate + Sn diffusion and α-Fe_2O_3 represented for 1 % Co-doped samples.

4.3.4 Optical Characterization

UV-Vis spectroscopy measured the optical properties of the photoanodes, enabling the analysis of the absorbance spectra and further band gap determination. Figure 4.9 shows the absorbance spectra of bare and Co-doped hematite photoanodes from both methods A ($NaNO_3$) and B (urea)[1], followed by the A and α at 535 nm presented in Table 4.5. All measured samples showed a maximum absorption peak approximately at 535 nm, presenting a red-shift from the characteristic hematite absorption maximum peak of ~ 440 nm [136, 146, 147]. This shift mainly arises from the two-step annealing. Between approaches, method B showed a higher red-shift with higher absorption over the wavelength range of 600 – 700 nm. However, the radiation in this range does not possess enough energy to generate electron-hole pairs, as it is lower than the photoanode band gap energy (E_g). Hence, this increase in absorption did not reflect a photocurrent enhancement.

	Method A - $NaNO_3$			Method B - Urea		
Doping %	0	1	7	0	1	7
A [%]	87.6	88.5	87.5	88.1	—	88.7
L [nm]	378	391	279	684	445	462
α [nm^{-1}]	0.53	0.52	0.72	0.30	—	0.44

TABLE 4.5: Absorbance (A), photoanode thickness (L) and absorption coefficients (α) at 535 nm of the undoped and Co-doped hematite NWs for both method A and B.

[1] A failure of the UV-vis-NIR spectrophotometer did not allow the measure on the 1 % Co-doped hematite photoanode on time for the dissertation submission date.

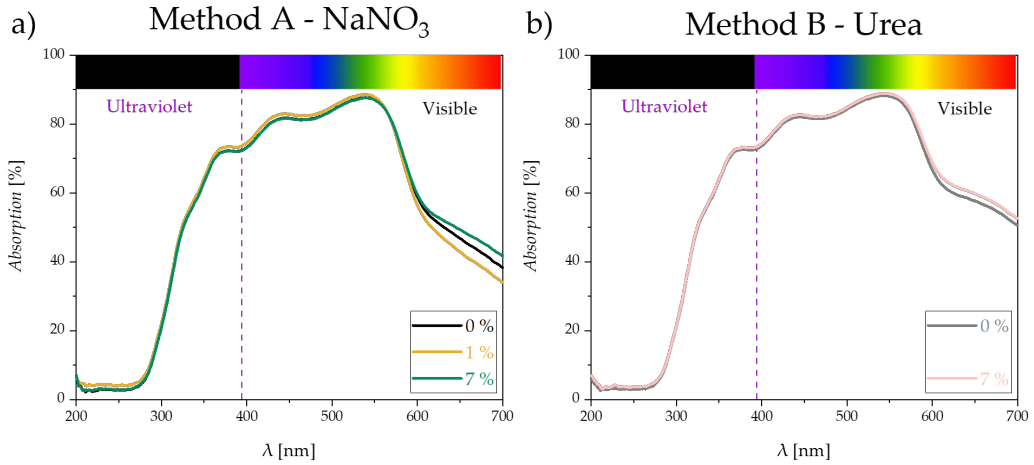

FIGURE 4.9: Absorbance spectra of of Co-doped α-Fe_2O_3 NWs synthesized by (a) method A with $NaNO_3$ and (b) method B with urea.

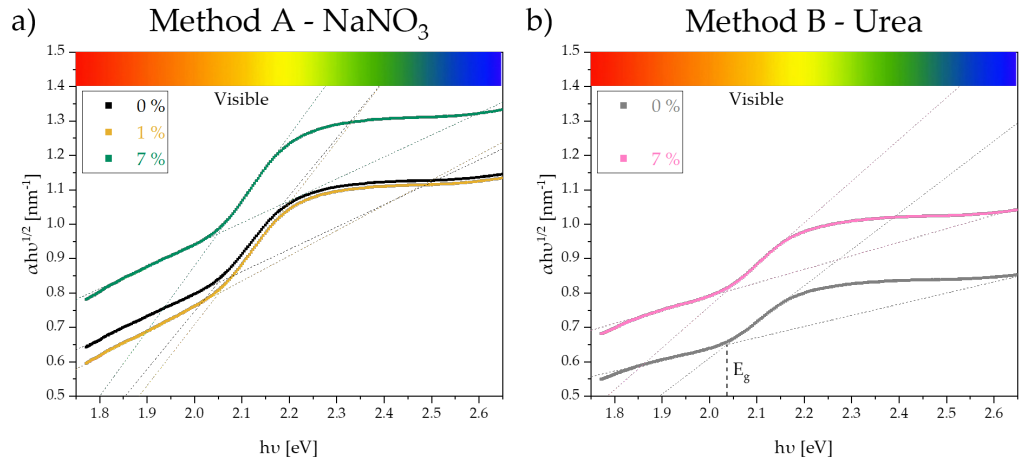

FIGURE 4.10: Tauc plots of Co-doped α-Fe_2O_3 NWs synthesized by (a) method A with $NaNO_3$ and (b) method B with urea.

In addition, Tauc plots (Figure 4.10) were represented to calculate the band gap values of the Co-doped photoanodes. Table 4.6 displays the obtained E_g compared with L from SEM. Samples prepared with method B (0 % and 7 %) showed smaller E_g (between 2.035 to 2.037 eV) than method A (between 2.049 to 2.052 eV), resulting from the higher red-shift observed in absorption spectra (Figure 4.9). Moreover, in method A, the slight reduction in the E_g of the 7 % sample compared to bare hematite appears to have contributed to the tiny increase in the j performance reported by this sample, as lower E_g are usually related to more visible light absorption [26]. However, method A samples achieved higher j responses while having larger E_g, implying that other factors, such as the smaller NWs thickness, preferential growth in the crystallographic (110) plane and higher Sn diffusion, must be balancing the overall j performance.

	Method A - $NaNO_3$			Method B - Urea		
Doping %	0	1	7	0	1	7
E_g [eV]	2.049	2.052	2.049	2.037	—	2.035
L [nm]	378	391	279	684	445	462

TABLE 4.6: Optical band gap energies (E_g) and photoanode thickness (L) of the undoped and Co-doped hematite NWs for both method A and B.

4.3.5 Conclusions

In this chapter, the impact of the oxidation agent was further extended to Cobalt doping of hematite NWs. Hematite NWs were synthesized by two hydrothermal methods: method A with sodium nitrate ($NaNO_3$) and method B with urea (CH_4N_2O) as the oxidation agent. Co-doped hematite NWs were prepared by both approaches (undoped samples were prepared in Chapter 3) to examine the PEC performance and morphological, structural and optical properties upon Co doping with various concentrations (1 and 7 %). As concluded in Chapter 3, the photoanode PEC performance is influenced by the combination of the contributions from multiple factors, like the NWs aggregation, an enriched crystalline structure, elemental doping by Sn diffusion from the FTO substrate and external reagent addition, and a well-adjusted optical band gap.

Overall, method A ($NaNO_3$) achieved higher j responses compared to method B (urea), associated with enhanced morphological and structural properties. Although photoanodes prepared by method A presented NWs aggregation, the thinner D of NWs with a shorter L obtained by method A ($NaNO_3$) led to a higher $\overline{j_A} \sim 0.76$ mA·cm^{-2} (1.45 V_{RHE}) compared with the lowest $\overline{j_B} \sim 0.60$ mA·cm^{-2} (1.45 V_{RHE}) from method B. Additionally, the preferential growth in the crystallographic (110) plane and higher Sn diffusion derived from XRD diffractograms and RBS spectra, respectively, were found to also contribute to the PEC performance of method A photoanodes. Even though samples prepared by method B (urea) presented higher absorption and a more suitable E_g, the morphological and structural features limited the j performance of these photoanodes.

In summary, the photoanodes prepared with $NaNO_3$ as the oxidation agent in the hydrothermal synthesis achieved the best j performances and properties features. For both methods A and B, the introduction of the Co dopant did not result in j improvements; however, it proved to be beneficial for the V_{onset} decrease, reaching cathodic shifts of 40 mV and 30 mV for 1 % in method A ($NaNO_3$) and 7 % in method B (urea), respectively.

Chapter 5

Optimization of Ti Doping in Hematite NWs

5.1 Overview

Titanium (Ti) has become one of the most common n-type cation dopants for hematite [98, 103–105, 109–112], just naming a few. From porous films [104] to flower-like clusters [105] and nanorods [109], an intense study has been developed to find the optimum doping route for Ti into α-Fe_2O_3. Although synthesis techniques like spray pyrolysis [105, 106], pulse laser deposition (PLD) [104] and electrodeposition [110] have been experimented, the hydrothermal technique has settled as one of main routes to effectively improve the PEC performance of hematite [98, 103, 107, 109, 111, 112].

Deng et al. reported, in 2012, the highest photocurrent density obtained so far for Ti-doped α-Fe_2O_3 nanorods synthesised by hydrothermal method [109]. The Ti doping promoted urchin-like nanostructures on top of nanorod arrays which increased the effective surface area, reduced the electron-hole recombination and increased the donor density, leading to a j of 1.91 mA·cm^{-2} at 1.23 V_{RHE}. Likewise, Wu et al. observed a decrease in the feature size of the nanorods as Ti was introduced in hematite structure increasing j by 2.2 times compared with the undoped hematite [112].

On a different strategy, Yang et al. reported the synthesis of Ti-doped α-Fe_2O_3 NWs with two hydrothermal stages: an initial short stage without the dopant forms a uniform undoped β-FeOOH layer, followed by a prolonged stage with the Ti dopant to dope β-FeOOH NWs [103] - this strategy was used in the synthesis methods studied in Chapters 3 to 5. The thin undoped β-FeOOH layer acts as an underlayer and a preparation of the substrate to the formation of the

doped NWs, suppressing the back-diffusion of electrons from the FTO and improving the crystallinity at the hematite/FTO interface. A 40 mV cathodic shift in V_{onset} plus a photocurrent density of 1.4 mA·cm^{-2} at 1.40 V_{RHE} was attained with this strategy, corresponding to an improvement of 20 % in comparison with the Ti-doped hematite without the undoped underlayer.

Summarizing, Ti presents itself as an important dopant of α-Fe_2O_3 to improve the photocurrent density by increasing the effective surface area and the donor density, while reducing the electron-hole recombination. However, onset potentials are usually anodic shifted when the dopant is introduced in hematite structure, with V_{onset} values being around 0.9 - 1.0 V_{RHE}. In terms of the oxidation agent used in the synthesis process, no reports with urea were found, being $NaNO_3$ the main oxidation agent used to produce hematite nanorods. Having this in consideration, a variation of the Ti dopant concentration was performed by the synthesis method A (with $NaNO_3$). Although there was curiosity in experimenting with method B (with urea), the late arrival of the Ti^{4+} precursor reagent, unable the experiment. Nevertheless, the experimentation of method B in Ti doping is marked as ongoing work by our laboratory. Our strategy is then to evaluate the impact doping concentration (C_{dopant}) has on hematite, enabling a direct comparison between different dopants (Ti, Co and Mn) relative to changes in morphology, structure and optical properties, which culminate in PEC performance variations.

5.2 Experimental Details

Ti-doped hematite photoanodes were prepared by a hydrothermal method (Subsection 2.1.3 of Chapter 2). The FTO glass substrates were cleaned by the methodology described in Subsection 2.1.2 and placed in a 25 mL stainless-steel autoclave filled with a 20 mL chemical solution of 0.15 M $FeCl_3 \cdot 6H_2O$ + 1 M $NaNO_3$ (oxidation agent) + 56 μL HCl – method A.

Afterwards, a first hydrothermal stage of 50 min at 95 °C with the undoped solution was performed to deposit a uniform undoped β-FeOOH layer (Subsection 2.1.3). Then, the amount of $C_6H_{18}N_2O_8Ti$ (0.5, 1 and 1.5 % in relation to the Fe^{3+} concentration) was added to the solution for the second stage of 13 h at 95 °C, merging with the undoped solution to dope the β-FeOOH NWs with Ti^{4+}. Finally, a thermal annealing treatment at 550 °C for 2 h (10 °C/min ramp) and 800 °C for 20 min (8 °C/min ramp) was conducted on all samples to convert the as-prepared β-FeOOH phase into the stable hematite phase (Subsection 2.1.3) [29]. The bare hematite photoanodes of method A ($NaNO_3$) and method B (urea) were the same as in Chapter 3.

Summarizing, four samples according to the concentration of Ti dopant (0, 0.5, 1 and 1.5 %) were synthesized for method A with $NaNO_3$ to allow the analysis of the doping concentration

Synthesis Method	Doping Concentration [%]
Method A – $NaNO_3$	0 0.5 1 1.5

TABLE 5.1: Ti-doped and undoped hematite samples prepared.

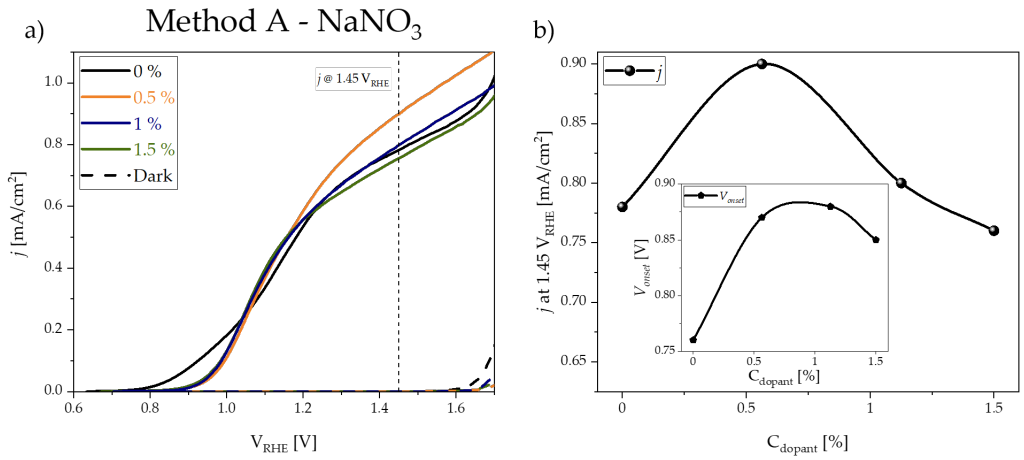

FIGURE 5.1: (a) Photocurrent density-voltage characteristic curves of the Ti-doped hematite nanowires synthesised with method A ($NaNO_3$). (c) j at 1.45 V_{RHE}, and insight graph showing V_{onset}, as a function of doping concentration (C_{dopant}).

impact on hematite NWs synthesized by the same method A route as Mn and Co doping in Chapters 3 and 4. Table 5.1 summarizes the prepared photoanodes.

5.3 Results and Discussion

5.3.1 Photoelectrochemical response

As PEC cells are essentially evaluated by their photoelectrochemical performance, j-V curves were performed to study the doping concentration effect and directly compare the Ti effect against other dopants (Co and Mn). Figure 5.1(a) presents the characteristic curves under dark and simulated sunlight for the several Ti-doped α-Fe_2O_3 photoanodes synthesised with method A. The extracted photocurrent density (j) at 1.45 V_{RHE} and the onset potential (V_{onset}) from j-V curves were plotted against the C_{dopant} to clearly analyse the doping impact of Ti on these parameters (Figure 5.1(b)). As reported by several authors [109, 110, 112], the onset potential positively shifted to higher potentials. In terms of j, an increase of 15 % compared with the undoped hematite was attained for 0.5 % Ti doping. Further doping to 1 % matches the undoped hematite photocurrent, while 1.5 % decreases its performance. Since all samples undertook the same synthesis process, it is safe to assume that this improvement comes from doping with Ti.

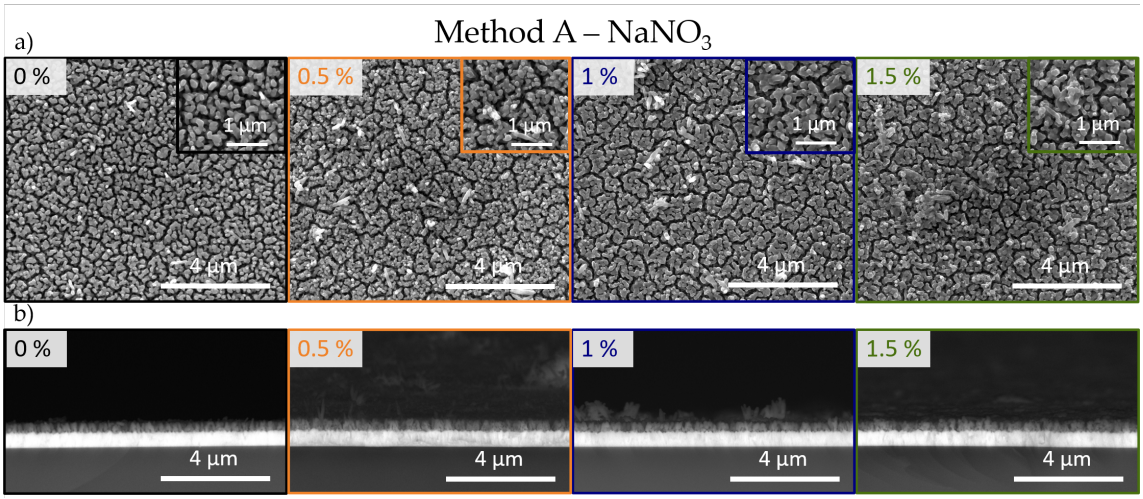

FIGURE 5.2: Scanning electron microscopy images of Ti-doped α-Fe_2O_3 NWs. (a) Top-section images, with inset figures showing a closer look of the photoanodes' NWs. (b) Cross-section images. Red circles and arrows indicate the longer aggregated NWs on top os NWs nanostructured film.

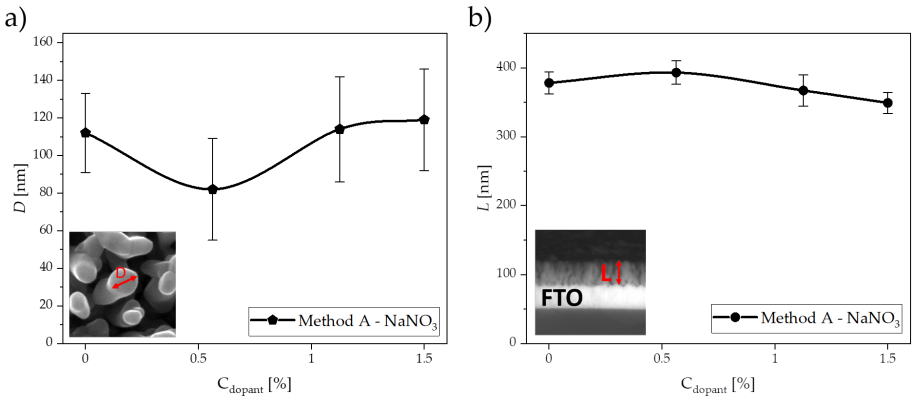

FIGURE 5.3: (a) Diameter (D) and (b) thickness (L) of Ti-doped α-Fe_2O_3 NWs as function of C_{dopant} (0 – 1.5 %).

To further understand the origin of this improvement, the morphological, structural and optical properties were inspected by SEM, XRD and RBS, and UV-Vis, respectively.

5.3.2 Morphological Characterization

SEM images show that Ti doping of hematite synthesised NWs, as expected [26, 103]. Through Figure 5.2 it is possible to observe the growth of longer aggregated NWs, which stand out from the NWs nanostructured film (visible on Figure A.4 from Appendix A), for the Ti C_{dopant} of 0.5 % and 1 %. A similar morphology was reported by Deng et al., where urchin-like nanostructures consisting of longer NWs standing on the short nanorods film increased the effective surface area [109].

Figure 5.3(a) and (b) represents the D and L behaviour against the C_{dopant}. The introduction of 0.5 % Ti doping led to a decrease in D, which then increase to a similar value as bare hematite with further doping (1 % and 1.5 %). The decrease of NWs diameter from the nanostructure film upon 0.5 % led to a higher surface area, which is related to an increase in j performance [109, 112]. On the other hand, no significant variation of the photoanode thickness was observed upon Ti doping (Figure 5.3(b)).

5.3.3 Structural Characterization

The structural characterization of Ti-doped hematite NWs was assessed by X-Ray Diffraction (XRD). Rutherford Backscattering Spectrometry (RBS) measures were not performed on these photoanodes due to the short availability of the equipment, prior to the preparation of the samples. Nevertheless, XRD analysis established of influential correlations between the j performance and XRD features.

X-Ray Diffraction

The determination of the crystalline phase and inspection of crystal structure was assessed by the X-Ray Diffraction technique. Once again, the use of a parallel beam (PB) with grazing incident omega (ω) angles configuration allowed the identification and improved study of hematite peaks by removing most of the FTO signal [26]. XRD diffractograms (Figure 5.4) prove the synthesis of the thermodynamically stable hematite phase (JCPDS 33-0664), described as corundum crystalline structure with hexagonal closed-packed unit cell. A preferential orientation occurs at the plane (110), with peaks from planes (012), (104), (113), (024), (116), (214) or (300) being also identified. Although no peaks related to Ti doping were detected, owing to the doping concentration in the material being lower than the diffractometer detection limit, a differentiation from the undoped, Mn and Co-doped samples was observed by the relative intensity increase of peaks from planes (012), (104), (113), (024) and, especially, (116) - see Figure 5.5. This shows that, contrary to previous samples, Ti promoted a higher growth in multiple planes, contributing to a less ordered photoanode. Despite this being associated with a lower conductivity, as for instance, the (104) plane is associated with oxygen vacancies that act as electron trapping sites and recombination centres, the photocurrent density did not seem affected by this, as shown by the 15 % increase in j for 0.5 % doping.

From peak broadening analysis, crystallite size (D_{XRD}) and microstrain (ε) were estimated, using the Williamson-Hall method (Equation 2.2) described in Chapters 2 and 3. Figure 5.7

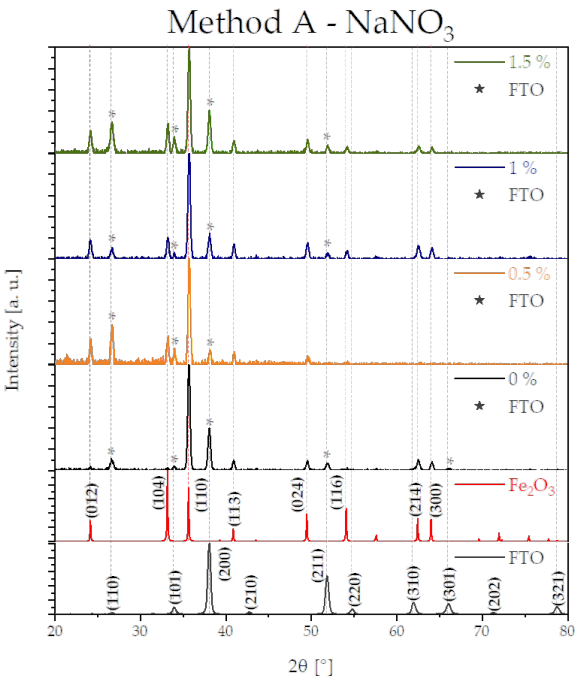

FIGURE 5.4: X-Ray Diffraction patterns of Ti-doped α-Fe_2O_3 photoanodes synthesised by method A ($NaNO_3$).

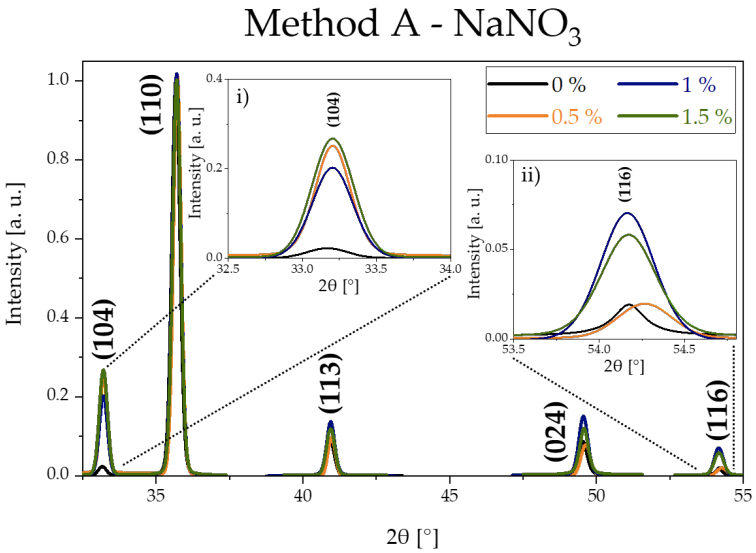

FIGURE 5.5: (a) Pseudo-Voigt fits of XRD (104), (110), (113), (024) and (116) experimental peaks, with inset graphs showing a higher magnification of (i) peak (104) and (ii) peak (116).

presents the crystallite size (D_{XRD}), diameter of NWs (D) and photocurrent density (j) variations for the different Ti C_{dopant} synthesised with method A (values displayed in Table 5.2). Although a high degree of error was found on 0.5 % sample (mainly due to an extremely low absolute intensity), it is reasonable to state 0.5 % Ti doping improved the crystalline structure of hematite, as the D_{XRD} was higher than the rest of samples. This improvement, along with the thinner NWs

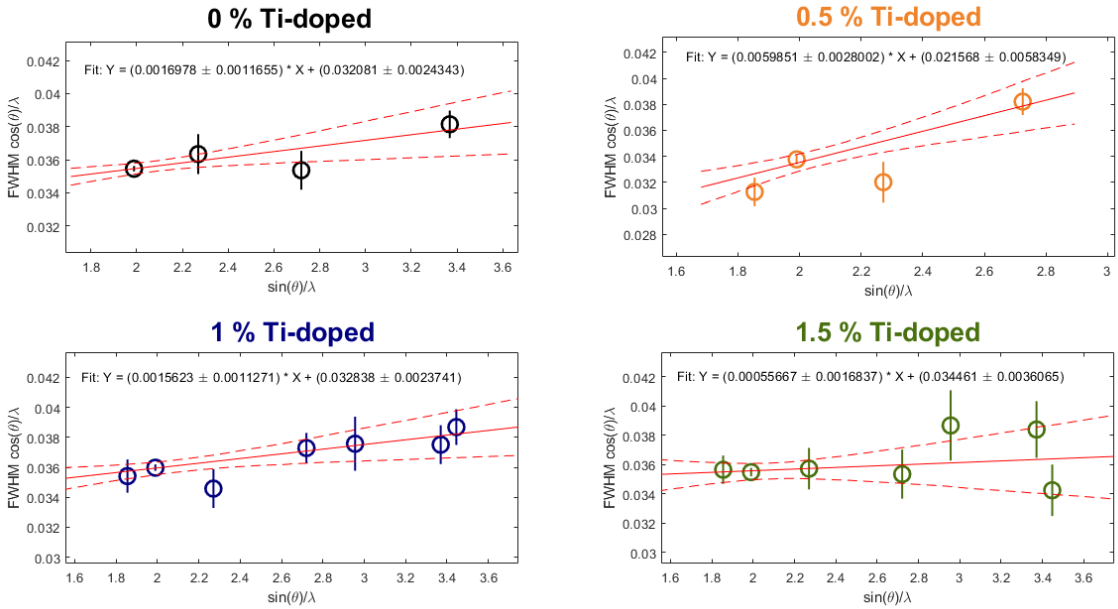

FIGURE 5.6: Linear fits using the Williamson-Hall relationship for Ti doped samples synthesized by method A (with $NaNO_3$).

	Method A - $NaNO_3$			
Doping %	0	0.5	1	1.5
D_{XRD} [nm]	29.3 ± 2.2	43.6 ± 11.8	28.6 ± 2.1	27.3 ± 2.8
ε [%]	0.04 ± 0.03	0.15 ± 0.07	0.04 ± 0.03	0.01 ± 0.04

TABLE 5.2: Crystallite size and microstrain of Ti-doped hematite NWs synthesized by method A.

D appears to support the 15 % increase achieved in j for the 0.5 % Ti-doped sample.

5.3.4 Conclusions

Ti doping with method A ($NaNO_3$) showed an optimum C_{dopant} of 0.5 %, reaching a $j \sim 0.9$ mA·cm^{-2} at 1.45 V_{RHE} (15 % increase response compared to bare hematite). This was associated with an increase in the effective surface area and an enhanced crystallinity quality.

Due to the a short availability of the RBS equipment prior to the preparation of the samples, RBS measures were not performed on these photoanodes. Additionally, fails in the Ultraviolet-Visible spectroscopy equipment on the last month of the thesis, disabled the optical characterization of this set of samples. These characterizations are intended to be performed in order to

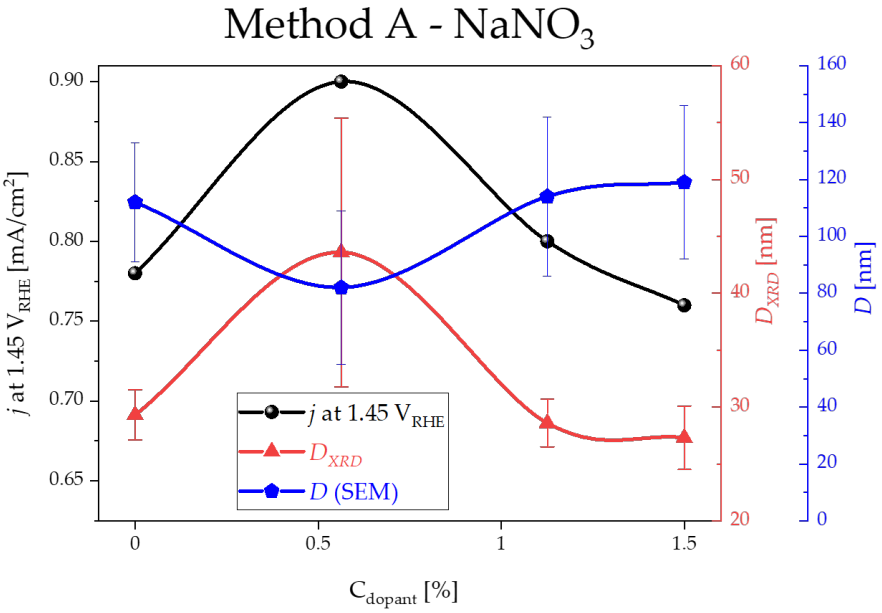

FIGURE 5.7: Photocurrent density (j), crystallite size (D_{XRD}) and NWs diameter (D) as a function of Ti doping concentration.

fully assess the impact of the Ti doping concentration on the synthesis with method A. Furthermore, as mentioned in the experimental section, experiments with urea are also seen as future work.

Chapter 6

Evaluation of the role of Multilayers in Tungsten Trioxide Nanoplates by Electrochemical Impedance Spectroscopy

This chapter presents the evaluation of the role of multilayers in tungsten trioxide (WO_3) nanoplates through Electrochemical Impedance Spectroscopy (EIS).

6.1 Overview

Semiconductor WO_3-based nanoplates were prepared by hydrothermal method. It was investigated the impact of different hydrothermal conditions, especially the temperature, time, and layer-by-layer thickness increase approach [26]. The different layers of WO_3 nanoplates were prepared by sequential steps of hydrothermal (12 h at 90 °C) and annealing processes (Subsection 2.1.4 of Chapter 2). Additionally, the morphological, structural, optical and photoelectrochemical features of the obtained photoelectrodes have already been studied. Figure 6.1 presents the variation of multilayer WO_3 photoelectrodes thickness (L) as a function of the number of layers (black color). On the other hand, Figure 6.2 shows the j-V curves measured of the multilayer WO_3 nanoplates, where an optimum j response for 5 layers sample can be observed. Ideal conditions were obtained with certain hydrothermal temperature and time in terms of photoresponse and then applied in the layer-by-layer hydrothermal growth approach. Photocurrent improvements of over 70 % were achieved with the studied conditions.

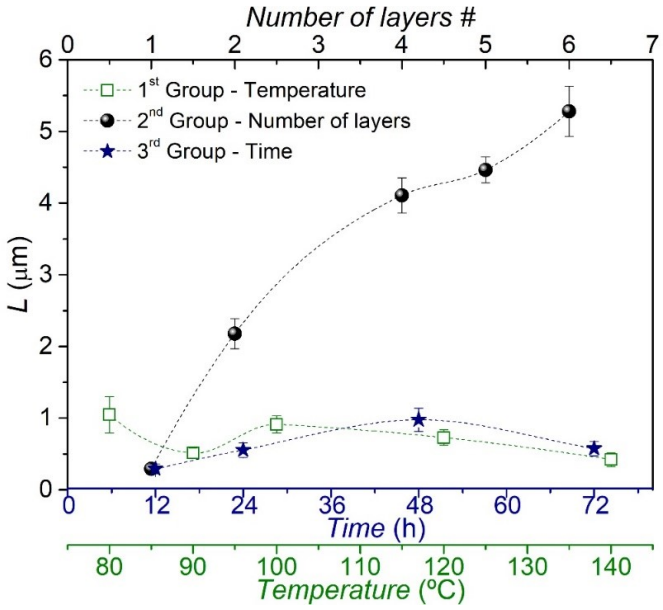

FIGURE 6.1: WO_3 photoelectrodes thickness (L) as a function of the hydrothermal parameters: temperature (1st Group), number of layers (2nd Group) and time (3rd Group); average L extracted from cross-section views of the SEM images. [Adapted from [26]]

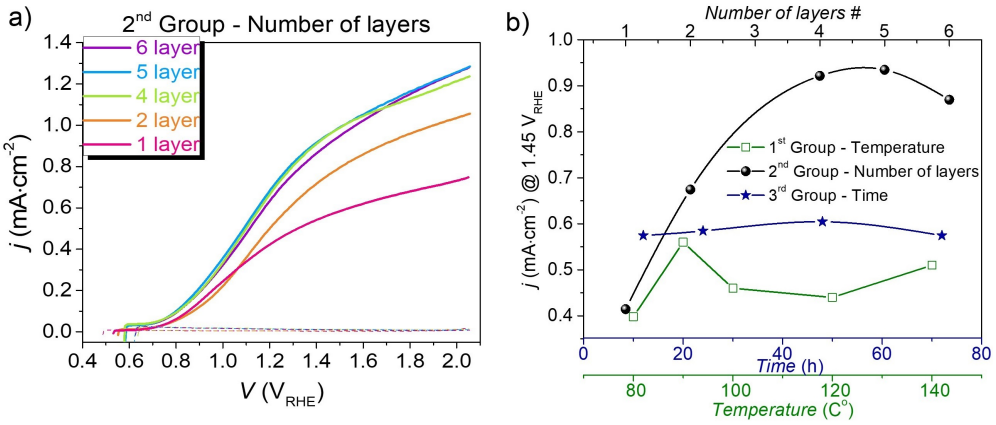

FIGURE 6.2: j-V characteristic curves for WO_3 samples: (a) 2nd group (number of layers) - samples prepared with several layers (1 to 6 layers), i.e. sequential steps of hydrothermal growth, each step (1 layer) during 12 h at 90 °C; (b) temperature, number of layers and time hydrothermal parameters as a function of j at 1.45 V_{RHE} for the different groups of samples. [Adapted from [26]]

EIS measurements, under dark conditions, were performed on the group of materials that displayed the most promising results, which was the variation of the number of layers, as an attempt to better understand the effect that the number of layers has on electrochemical performance, through the better understanding of the semiconductor/electrolyte interfacial phenomena. From the Nyquist plots (Figure 6.3), it is possible to extract detailed information about the group of resistances and capacitances that describe the behaviour of the electrochemical reaction kinetics, ohmic conduction processes and mass transport limitations on the PEC cell

performance, by fitting a suitable electrical analogue to the EIS data, as described elsewhere [115, 157].

This work is based on the article to be submitted: Hydrothermal growth of WO_3 nanoplates multilayers, by Paula Quitério, João P. Freitas, Tânia Lopes, Adélio Mendes, Célia T. Sousa, João P. Araújo and Arlete Apolinário.

6.2 Results and Discussion

According to literature, an initial analysis included fitting the experimental data with three different circuits, illustrated in Figure 6.4 [115, 157]. Circuit A consists on a simplified Randles circuit with one RC element (R_T and C_T) related to both the bulk semiconductor transport and the charge transfer at the semiconductor/electrolyte interface; while circuit B presents two RC elements, one representing the bulk semiconductor transport (R_{SC} and C_b) and the other the charge transfer at the semiconductor/electrolyte interface (R_{CT} and C_{dl}). Both these circuits use constant phase elements (CPE) instead of the ideal double layer capacitor, as the photoanodes are nanostructured [158]. Finally, circuit C consists on a simplified Randles circuit with an ideal double layer capacitor.

Sample with 1 layer presents two RC elements, fitting with circuit B. However, the RC element associated with the higher frequencies refers to the FTO/electrolyte interface, instead of the bulk semiconductor transport. This was only seen for this sample, which presents a larger resistance and capacitance compared to others, as the low volume deposited on the 1 layer sample left some areas of the FTO exposed to the electrolyte. The RC element associated with the WO_3 bulk semiconductor transport was only observed on the 6 layers sample at high frequencies. This suggests that an increase in charge transport resistance is offered in samples with a thickness higher than 5.5 μm (samples' thickness can be seen in Figure 6.1), such that circuit B can then be properly utilized. Samples with 2 – 5 layers had larger deposited volumes, which suppressed the FTO/electrolyte interface, yet kept a low charge transport resistance. Therefore, only the RC element from the semiconductor/electrolyte interface was observed. Circuit C presented large errors associated with the RC element fitted, as the photoanodes are nanostructured and an ideal double layer capacitor was used. Hence, it was not a suitable option.

Therefore, the proposed electrical analogue, in Figure 6.5 (a), known as simplified Randles cell [159], comprises a series resistance (R_S) and one RC element in series representing the semiconductor/electrolyte interface (R_{CT} and C_{dl}), with the use of a constant phase element (CPE) instead of the ideal double layer capacitor, as the photoanodes are nanostructured [158].

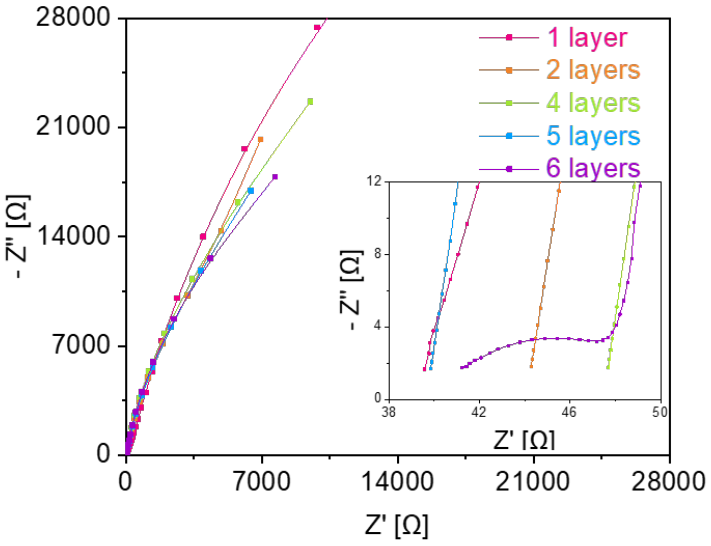

FIGURE 6.3: Nyquist diagrams obtained at 1.45 V_{RHE} for the increased number of layers of WO_3, with an insight graph focused on the high frequency range.

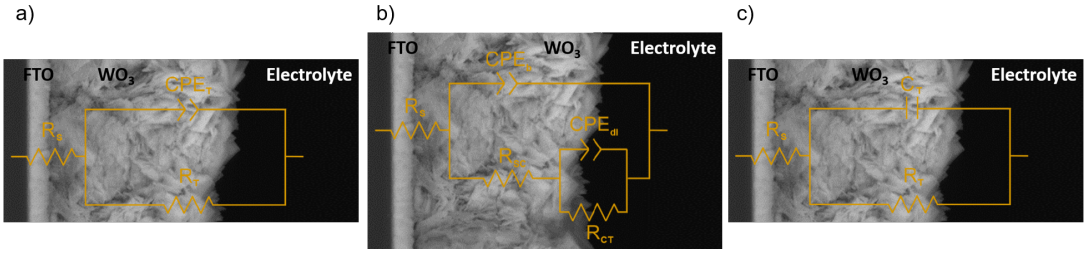

FIGURE 6.4: Equivalent circuit analogous fitted to EIS data measurements: (a) Circuit A - simplified Randles circuit with constant phase element; (b) Circuit B - two *RC* elements with constant phase elements; (c) Circuit C - simplified Randles circuit.

The experimental data were fitted to the equivalent circuit analogous, on the low frequency range (0.6 Hz – 45 Hz), allowing the study of the charge transfer effect at the semiconductor/-electrolyte interface, without the impact of the phenomena occurring at high frequencies.

Fitting the experimental data with the equivalent circuit analogous from Figure 6.5 (a) on the low frequency range, the parameters R_S, R_{CT} and C_{dl} were obtained. As expected, the series resistance (R_S) remains constant for the different samples, as shown in Figure 6.5 (b), since it englobes the resistances from FTO substrate, electrolyte ion conductivity and setup connections, which remained the same. On the other hand, the charge transfer resistance (R_{CT}) decreases as the number of WO_3 layers increases, achieving its lower value for 5 layers, as seen in Figure 6.5 (c). The double layer capacitance (C_{dl}) also increases, meaning the double layer width decreases (Figure 6.5 (d)). In summary, the lowest resistance to the charge transfer and the highest *j* value in the *j*-*V* curves (Figure 6.2(a) and (b)), confirm that 5 layers are the optimum

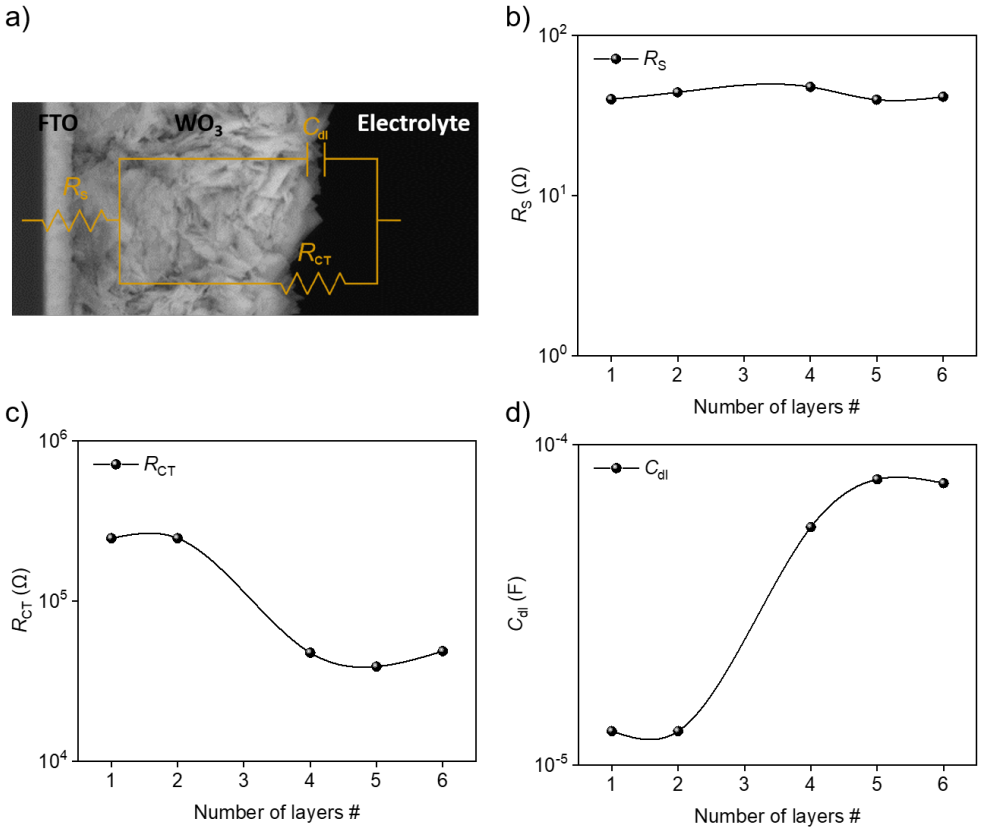

FIGURE 6.5: (a) Equivalent circuit analogous fitted to EIS data measurements. Number of layers effect on WO_3 photoanode impedance parameters at 1.45 V_{RHE}: (b) Series resistance, R_S; (c) Charge transfer resistance, R_{CT}; (d) Double layer capacitor - C_{dl}.

number of layers for a WO_3 nanoplates photoanode.

To further analyze the behaviour of the effect of the number of layers, a Mott-Schottky analysis was performed - figure Figure 6.6, determining the donor density (N_D) and flat-band potential (E_{fb}) from the equation [160]:

$$\frac{1}{C^2} = \frac{2}{\varepsilon\varepsilon_0 A^2 q N_D}\left(E - E_{fb} - \frac{k_B T}{q}\right), \tag{6.1}$$

where C is the space charge capacitance (F/cm^2), A is the surface area of the electrode (A = 0.283 cm^2), ε_0 is the vacuum permittivity (ε_0 = 8.854×10^{-14} F/cm), ε is the dielectric constant for nanostructured WO_3 (ε = 50) [115, 161], q is the electron charge (q = 1.6×10^{-19} C), E is the applied potential (V), k_B is the Boltzmann constant (k_B = 1.38×10^{-23} J/K), and T is the temperature ($\frac{k_B T}{q}$ = 0.026 V at 25 °C).

All plots showed positive slopes, assuring that all samples are n-type semiconductors. The calculated N_D and V_{fb} are listed in the table presented in Figure 6.6 (b).

a)

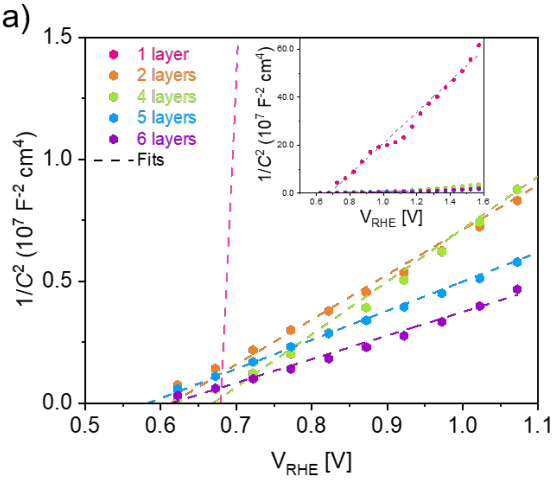

b)

Layers	N_D [cm^3]	V_{fb} [V]
1	4.36 x 10^{21}	0.65
2	1.53 x 10^{23}	0.59
4	1.31 x 10^{23}	0.64
5	2.36 x 10^{23}	0.56
6	2.91 x 10^{23}	0.59

FIGURE 6.6: (a) Mott-Schottky plots and fits for the WO_3 study of number of layers by EIS under dark conditions, with insight graph representing a wider potential range. (b) EIS parameters calculated from Mott-Schottky analysis.

Although the Mott-Schottky equation is based on planar structures, hence not offering precise values for nanostructured materials, it still can be applied to compare changes between samples prepared with the same methods and measured on a similar setup. One layer sample exhibit a donor density of about 4.36×10^{21} cm^{-3} and a flat band potential of 0.65 V, in accordance with previous literature [115, 162]. However, for the rest of the samples, a large increase in the donor density was observed, reaching 10^{23} cm^{-3}, which to our knowledge was not yet achieved for this kind of nanostructure. A reason for this might rely on not having used the effective area, i. e. since the photoanodes are nanostructured, the area in contact with the electrolyte is larger than the area used for calculation, which is based on the opening area of the smaller sample holder of the cappuccino PEC cell. Additionally, the increase in volume by the increment of layers must have led to a larger number of free electrons. For the flat band potential, the lowest value was obtained for the 5 layers sample, in agreement with the lowest onset potential title also achieved (Figure 6.2(a)). Thus, an increase in the number of layers is beneficial for the photoelectrochemical performance, obtaining the best photoanode performance for 5 layers.

6.3 Conclusions

EIS measurements allowed a better understanding of the effect the number of layers has on electrochemical performance. Fitting the experimental data with a simplified Randles cell circuit (Figure 6.5 (a)) on the low frequency range, allowed a better understanding of the semiconductor/electrolyte interfacial phenomena, without the impact of the phenomena occurring at high frequencies.

Sample with 5 layers showed the lowest resistance to charge transfer between the semiconductor/electrolyte interface, corroborating the results obtained in the *j*-*V* curves, where the best photocurrent density was attained for the 5 layers sample. Additionally, this sample presented the lowest flat band potential, yielding a lower onset potential.

In conclusion, an increase in the number of layers was beneficial for the photoelectrochemical performance of the WO_3 nanoplates photoanodes, obtaining the best photoanode performance for 5 layers of sequential hydrothermal growth steps of 90 °C for 12 h.

Chapter 7

Conclusions and Ongoing/Future Work

This chapter presents the overall conclusions of work developed in this dissertation, followed by a summary description of the ongoing and future work to be developed.

7.1 Conclusions

This dissertation was divided into two parts. The first part (Chapters 3 to 5) was composed of the optimization of hematite NWs by performing a systematic and multifaceted study of Mn, Co and Ti doping in hematite nanowires, combining the variation of two parameters: (i) the oxidation agent of the hydrothermal solution and (ii) the concentration of the dopant. The oxidation agent used to oxidize to Fe^{3+} precursor in the hydrothermal treatment was tested with $NaNO_3$ (method A) and urea (method B). Secondly, the doping concentration was tested for: 1, 7 and 13 % for Mn, 1 and 7 % for Co, and 0.5, 1 and 1.5 % for Ti, establishing the doping range from literature [93–95, 98, 100, 103]. Furthermore, the impact of these synthesis parameters on the photoelectrochemical (PEC) performance, photocurrent (j) and onset potential (V_{RHE}), was correlated with morphological, structural and optical characterization. On the second part (Chapter 6), Electrochemical Impedance Spectroscopy (EIS) was performed on WO_3 nanoplates developed also by hydrothermal method, in an attempt to better understand the effect of the photoanode material thickness, achieved by the sequential WO_3 growth of layers. EIS provided a better understanding of the semiconductor/electrolyte interfacial phenomena, enabling a correlation between the EIS features with the j-V measurements.

For the success of this dissertation, it was fundamental the strong collaboration between three research groups: the Institute of Physics for Advanced Materials, Nanotechnology and

Photonics (IFIMUP), from Faculty of Sciences from the University of Porto (FCUP); the Laboratory for Process Engineering, Environment, Biotechnology and Energy (LEPABE), from Faculty of Engineering from the University of Porto (FCUP); and the Campus Técnologico e Nuclear (CTN), from Instituto Superior Técnico (IST), Lisbon. The IFIMUP's know-how in the preparation and characterization of advanced nanostructures, allied with LEPABE's strong experience in dye-sensitized solar cell (DSC) and PEC cells development and characterization, and CTN's remarkable application of ionizing radiation to characterize multifaceted samples, was crucial to achieving the objectives of this dissertation.

Generally, the oxidation agent unveiled a strong impact on the synthesis of both undoped (bare) and doped hematite NWs. Regarding bare hematite (C_{dopant} = 0 %), a higher photocurrent density (j) was obtained for method A ($j \sim 0.78$ mA·cm^{-2}) compared with method B ($j \sim 0.65$ mA·cm^{-2} at 1.45 V_{RHE}). The smaller thickness measured by SEM images along with a higher conductivity suggested by the structural preferential growing in the (110) plane and higher Sn diffusion led to an enhanced j response of method A ($NaNO_3$).

The introduction of the Mn dopant showed no j improvements in method A ($NaNO_3$), whereas in method B (urea), a 7 % Mn C_{dopant} achieved a 37 % increase in j response ($j \sim 0.89$ mA·cm^{-2} at 1.45 V_{RHE}), compared to the respective bare hematite photoanode. This increase was associated with an enhanced crystallinity quality and thin thickness. Additionally, Rutherford Backscattering Spectrometry (RBS) measurements suggested that the 7 % Mn dopant promoted a higher Sn diffusion, which is associated with higher conductivity. Furthermore, low doping concentrations (1 %) promoted the contribution of the (104) plane, which proved to be beneficial to the decrease of the onset potential (V_{onset}), reaching remarkable cathodic shifts of 70 mV and 60 mV for method A ($NaNO_3$) and method B (urea), respectively.

On other hand, for both methods ($NaNO_3$) and B (urea), the introduction of the Co dopant did not result in j improvements, however, proved to be beneficial for the decrease of V_{onset}, reaching cathodic shifts of 40 mV and 30 mV for 1 % in method A ($NaNO_3$) and 7 % in method B (urea), respectively. Finally, Ti doping with method A ($NaNO_3$) showed an optimum C_{dopant} of 0.5 %, reaching a $j \sim 0.9$ mA·cm^{-2} at 1.45 V_{RHE} (15.5 % increase response compared to bare hematite). This was associated with an increase in the effective surface area and an enhanced crystallinity quality.

On the second part of this dissertation, Electrochemical Impedance Spectroscopy (EIS) was performed on WO_3 nanoplates in an attempt to better understand the effect that the number

of layers has on electrochemical performance, through a better understanding of the semiconductor/electrolyte interfacial phenomena. EIS features corroborated the *j*-*V* results with the 5 layers sample achieving the lowest resistance to charge transfer between the semiconductor/electrolyte interface and lower flat-band potential. Thereby, EIS measures reinforced that 5 layers were the optimum number of layers for a WO_3 nanoplates photoanode.

7.2 Ongoing and Future Work

From the promising results obtained throughout this dissertation, the continuous development of PEC cells is being carried out in different manners. Remarkable results of Mn-doping regarding a 70 mV cathodic shift of V_{onset} aligned with the deep complete characterization of the material allow us to establish short-term goals to finish this work for publication. Two ongoing strategies are being implemented for the finalization of this work (also in the frame of the H2INNOVATE project):

- Further study closing the gap between the doping concentrations of Mn doping in hematite NWs, to inspect if there is a doping range (possibly between 1 % and 7 %) where we can establish a better compromise between the high *j* response obtained by 7 % doping and the lower V_{onset} attained by 1 % doping.

- Additional characterization techniques, such as X-Ray Photoelectron Spectroscopy (XPS), are required to confirm the presence of the dopant at the surface of the samples. This will lead to an enhancement of the RBS fits, which will allow a deeper study of the dopants distributions along the in-depth profile of the hematite NWs. RBS measures of the 13 % Mn doping photoanodes will enable us to further inspect the effect of excessive doping. Last but not least, EIS will unveil the electrochemical phenomena occurring at the semiconductor/electrolyte interface and 'bulk' semiconductor. This combined with the donor density and flat-band potential determination will allow a deeper understanding of the *j* improvements and V_{onset} shifts presented upon Mn doping.

Moreover, further improvements in the efficiency of the photoanodes can be achieved by employing other strategies based on the photoanodes developed in this dissertation:

- Surface treatments, like the deposition of co-catalyst, increase the water oxidation kinetics and lower the electron-hole recombination. In specific, the co-catalyst FeCo, electrodeposited to a stoichiometry of $Fe_{10}Co_{90}$, has proved to increase the photocurrent for

more than 60 % on hematite films photoanodes as well as produced an approximately 10 mV cathodic shift on the V_{onset} [146, 163]. In this work, the same $Fe_{10}Co_{90}$ co-catalyst was electrodeposited on Mn-doped hematite NWs in order to access the impact of the co-catalyst into a nanostructured hematite photoanode. Initial studies on samples with a low PEC response to test the applicability of this co-catalyst on hematite NWs samples showed promising results, presenting a 6 × fold increase in j compared with the measure previous to the deposition of the co-catalyst. However, further experiments are planned using the enhanced samples prepared in this work.

- As a long-term goal for future work, more advanced photoanodes will be prepared employing strategies such as heterojunctions [164] and homojunctions [165], which increase the charge separation efficiency of the PEC cells. Combining the acquired hydrothermal methods of WO_3 and hematite, a heterojunction of these two semiconductors will be performed in a two-step approach. Some first heterojunction samples, combing WO_3 and α-Fe_2O_3 semiconductors, were already successfully performed during this thesis, however, further tests should be implemented in the future.

Appendix A

Complementary Results

This appendix contains complementary results that help the presented results and discussions taken in Chapters 3 to 5.

The front illumination and backside illumination were tested on the same sample, in order to verify the advantage of using front illumination:

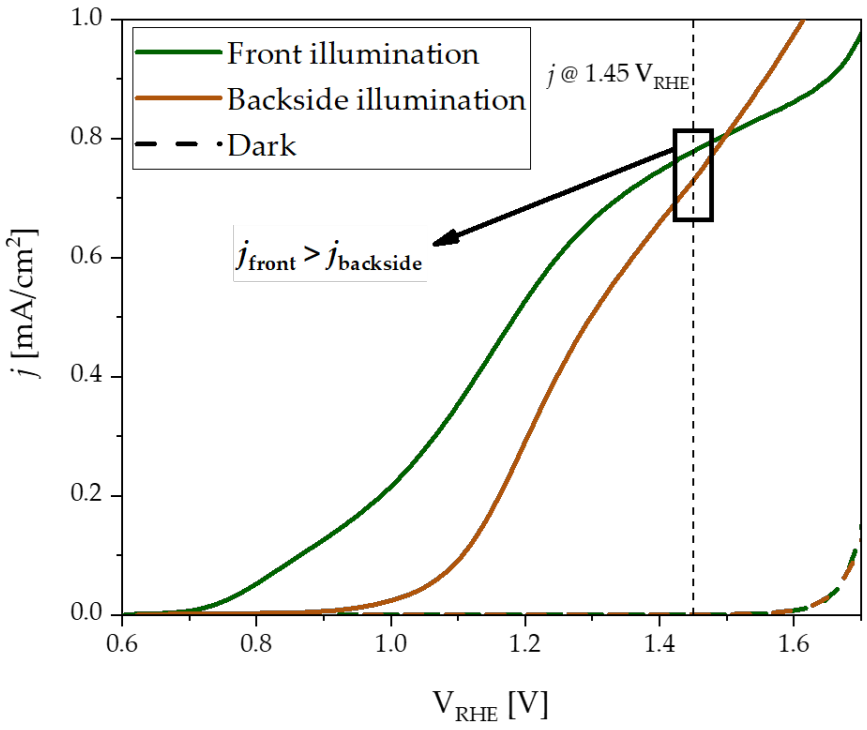

FIGURE A.1: *j-V* curves from 1 % Mn-doped (method A - $NaNO_3$) collected from front illumination and backside illumination. As expected, the front illumination gives more photocurrent density.

Morphological Characterization

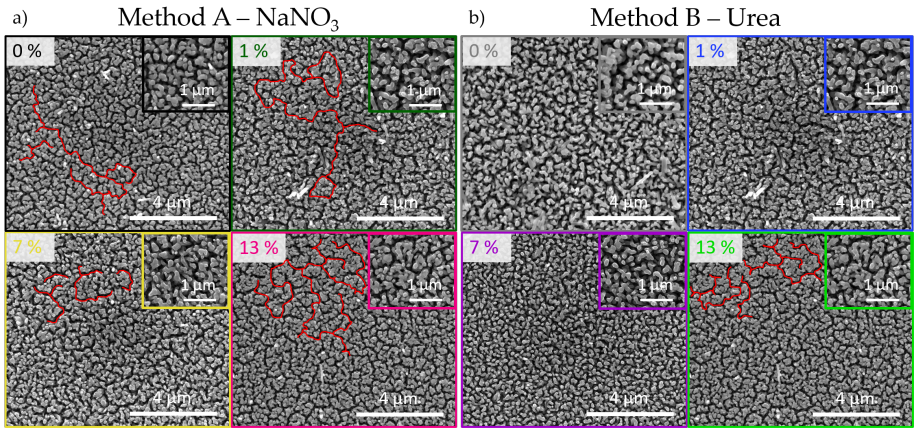

FIGURE A.2: Scanning Electron Microscopy images of Mn-doped α-Fe_2O_3 NWs synthesized by (a) method A with $NaNO_3$ and (b) method B with urea. Inset figures show a closer look of the photoanodes' NWs. Red lines mark some of the "paths" formed in the synthesis process.

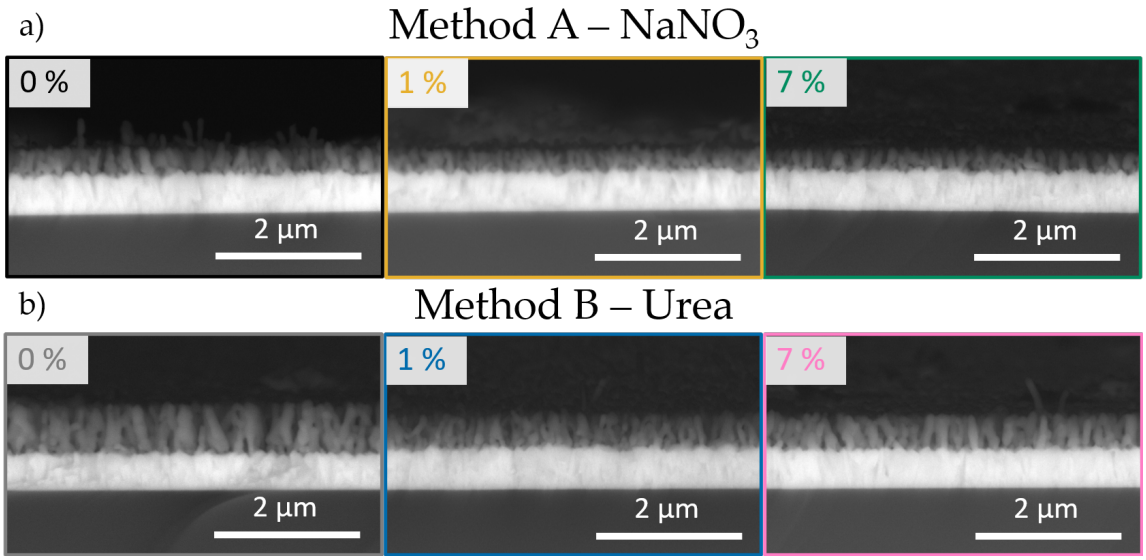

FIGURE A.3: Scanning Electron Microscopy cross-section images of Co-doped α-Fe_2O_3 NWs synthesized by (a) method A with $NaNO_3$ and (b) method B with urea.

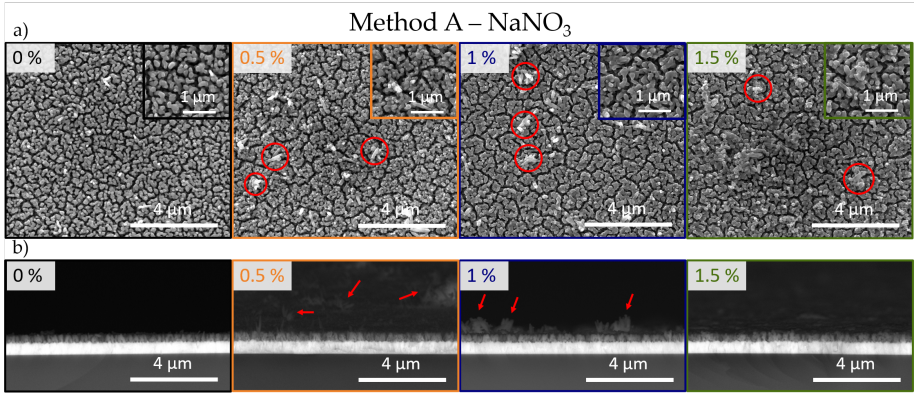

FIGURE A.4: (a) Top-section and (b) cross-section Scanning Electron Microscopy images of Ti-doped α-Fe_2O_3 NWs synthesized by method A with $NaNO_3$. Inset figures on (a) show a closer look of the photoanodes' NWs. Red circles and lines mark some of the longer aggregated NWs which stand out from the NWs nanostructured film.

Structural Characterization

X-ray Diffraction

Identified peaks from α-Fe_2O_3 were individually fitted with the Pseudo-Voigt function:

$$I = I_0\left[\eta\frac{2}{\pi}\frac{w}{4(\theta-\theta_C)^2+w^2} + (1-\eta)\frac{\sqrt{4\ln 2}}{\sqrt{\pi}w}\exp\left(\frac{4\ln 2}{w^2}(\theta-\theta_C)^2\right)\right], \tag{A.1}$$

where I_0 corresponds to the peak intensity, η the profile shape factor ($0 < \eta < 1$), w the full width at hall maximum (FWHM) and θ_C the diffraction angle peak. Figure A.5 shows an example of the fits performed on experimental data.

D_{XRD} and ε values were determined by:

$$D_{XRD} = \frac{k}{b}; \tag{A.2}$$

$$\varepsilon = \frac{m}{4}; \tag{A.3}$$

where k is the Scherrer constant ($k = 0.94$), b the interception at origin and m the slope.

Rutherford Backscattering Spectrometry

Table A.1 displays the atomic number, atomic mass and energy at surface of the elements associated with the photoanodes and the incident ion He^+ for detector RBS2 (θ_d = -140 °).

The RBS measures of the calibration samples for each detector is displayed on Figure A.6, following the linear fits performed to determine the calibration curves in Figure A.7.

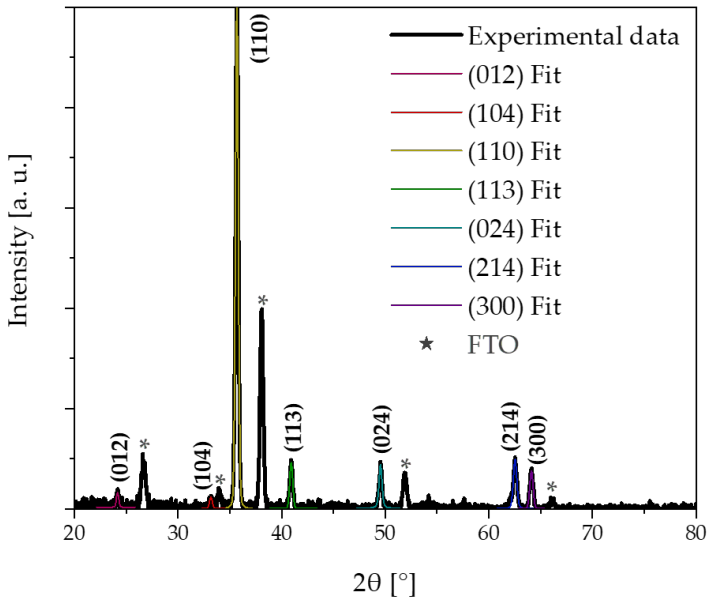

FIGURE A.5: Pseudo-Voigt fits for all identified hematite peaks, performed individually. Graph presents the fits of undoped hematite synthesized by method A, as an example.

Element	Atomic Number (Z)	Atomic Mass (M) [g/mol]	Energy after collision ($E_{1_{RBS2}}$) [keV]
He^+	2	4.0026	- - -
O	8	15.999	339.6025
Si	14	28.085	529.3918
Ti	22	47.867	665.3907
Mn	25	54.938	693.2633
Fe	26	55.845	696.435
Co	27	58.933	706.4306
Sn	50	118.71	803.7923

TABLE A.1: Atomic number, atomic mass and energy at surface for detector RBS2 for elements associated with the photoanodes (M_2,Z_2) and the incident ion He^+ (M_1,Z_1).

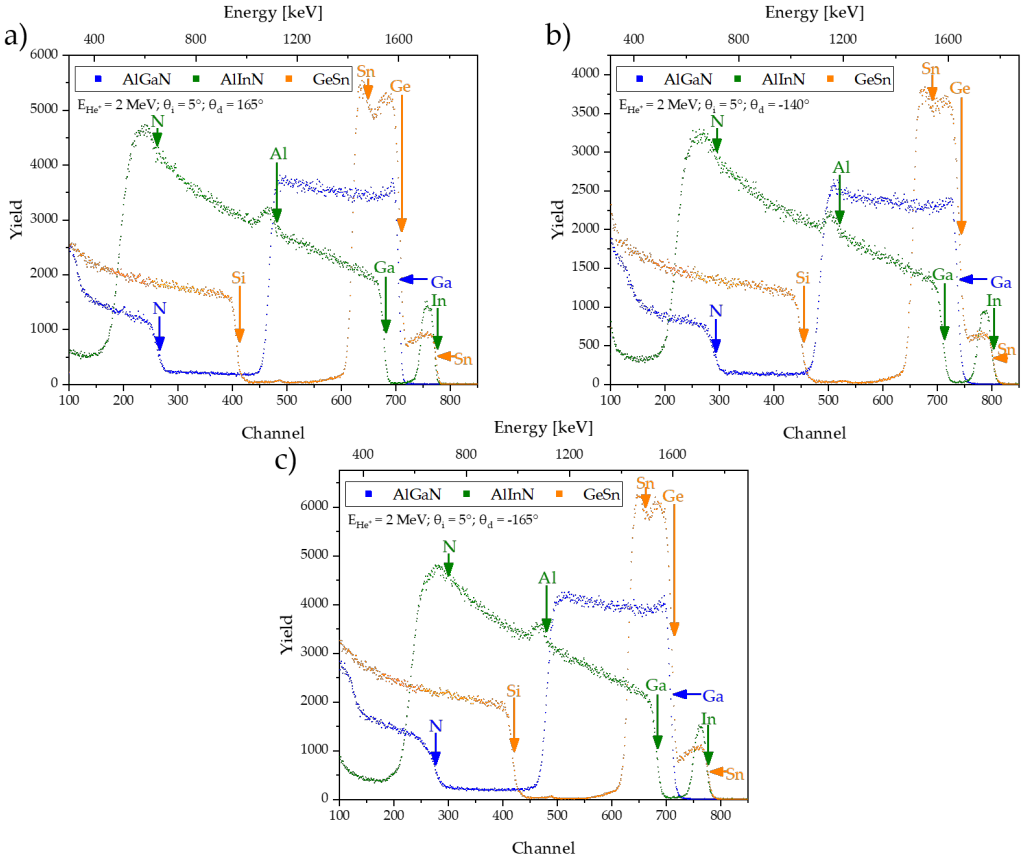

FIGURE A.6: RBS spectra of the calibration samples, with peak elements defined for (a) detector RBS1, (b) detector RBS2 and (c) detector ERD.

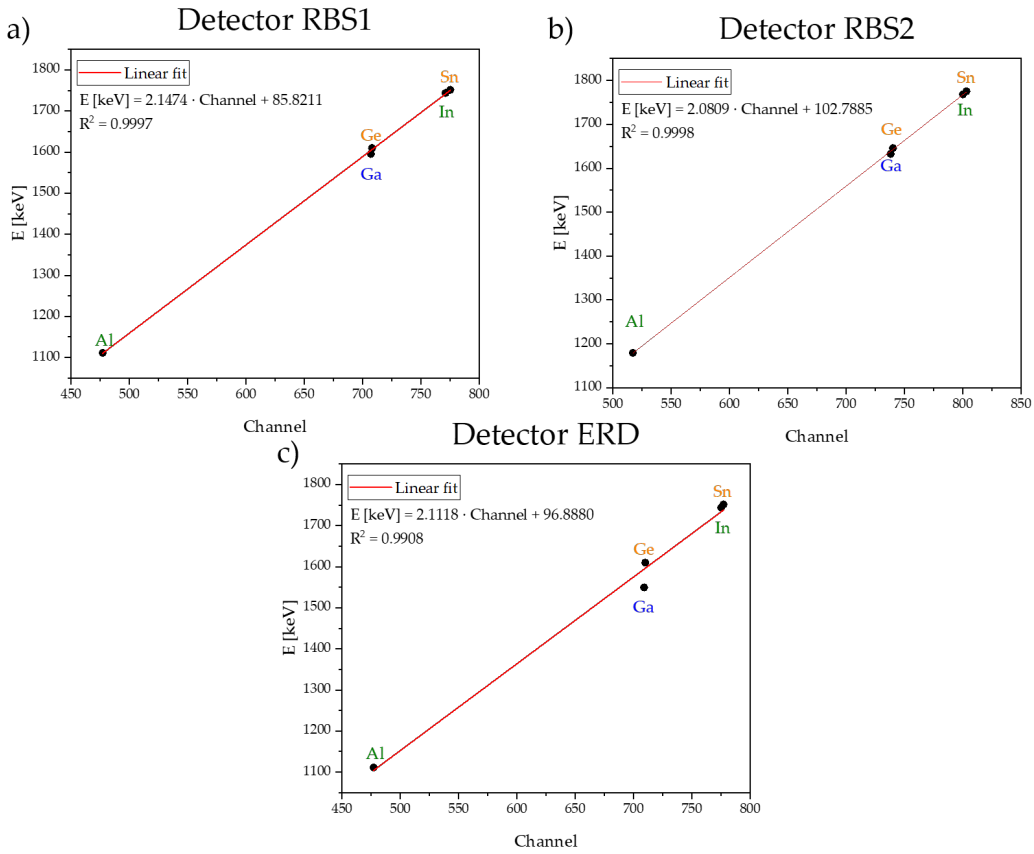

FIGURE A.7: Calibration curves for the (a) detector RBS1, (b) detector RBS2 and (c) detector ERD.

Optical Characterization of bare hematite photoanodes

Figure A.8 displays the absorption spectra of bare hematite NWs synthesized by method A ($NaNO_3$) and method B (urea). Although an extra red-shift was observed in method B, it did not correlated to an improved *j* response.

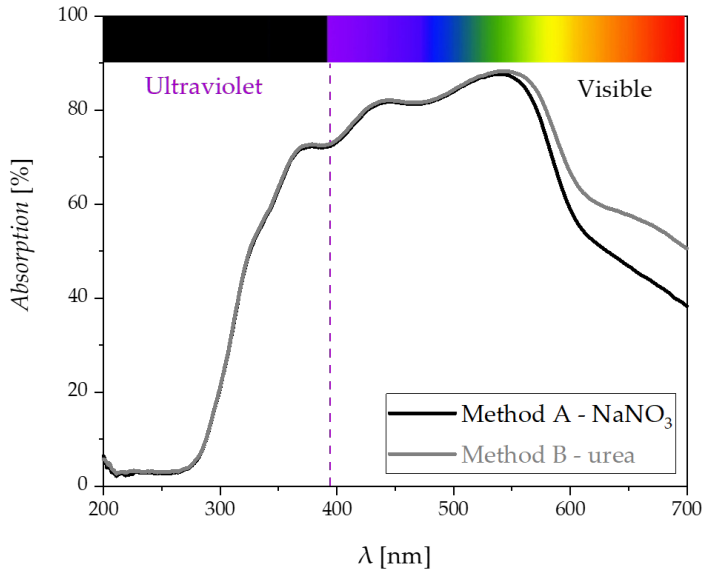

FIGURE A.8: Absorption spectra of bare α-Fe_2O_3 NWs synthesized by method A ($NaNO_3$) and method B (urea).

Bibliography

[1] IEA, "World energy outlook 2021," *IEA, Paris*, 2021. [Online]. Available: https://www.iea.org/reports/world-energy-outlook-2021

[2] B. Gates, *How to avoid a climate disaster: the solutions we have and the breakthroughs we need*. Knopf, 2021.

[3] M. R. Hannah Ritchie and P. Rosado, "Energy," *Our World in Data*, 2020. [Online]. Available: https://ourworldindata.org/energy

[4] A. Buis. Part 2: Selected findings of the ipcc special report on global warming. Consulted on 19-10-2022. [Online]. Available: https://climate.nasa.gov/news/2865/a-degree-of-concern-why-global-temperatures-matter/

[5] Decisions can be consulted here:. Consulted on 19-10-2022. [Online]. Available: https://unfccc.int/decisions

[6] M. R. Hannah Ritchie and P. Rosado, "Co2 and greenhouse gas emissions," *Our World in Data*, 2020. [Online]. Available: https://ourworldindata.org/co2-and-other-greenhouse-gas-emissions

[7] S. B. Pieter de Pous, Artur Patuleia and C. Rosslowe, "More renewables, less inflation - restoring eu economic stability through investment in renewables," *E3G & EMBER*, 2022. [Online]. Available: https://ember-climate.org/app/uploads/2022/10/E3G-EMBER-Briefing-More-renewables-less-inflation.pdf

[8] R. De Levie, "The electrolysis of water," *Journal of Electroanalytical Chemistry*, vol. 476, no. 1, pp. 92–93, 1999.

[9] Hydrogen in history. Consulted on: 20/10/2022. [Online]. Available: https://www.theworldofhydrogen.com/gasunie/history/

[10] (2022) Timeline of hydrogen technologies. Consulted on: 20/10/2022. [Online]. Available: https://en.wikipedia.org/wiki/Timeline_of_hydrogen_technologies

[11] K. van Kranenburg-Bruinsma, Y. van Delft, A. Gavrilova, R. de Kler, C. Schipper-Rodenburg, R. Smokers, M. Verbeek, and R. Verbeek, "E-fuels-towards a more sustainable future for truck transport, shipping and aviation," 2020.

[12] (2021) First uk trial of hydrogen blended gas hailed a success. Consulted on: 20/10/2022. [Online]. Available: https://hydeploy.co.uk/about/news/first-uk-trial-of-hydrogen-blended-gas-hailed-a-success/

[13] G. Thomas and J. Keller. Hydrogen storage - overview. Accessed: 04-08-2022. [Online]. Available: https://www1.eere.energy.gov/hydrogenandfuelcells/pdfs/bulk_hydrogen_stor_pres_sandia.pdf

[14] Gasoline. Accessed: 04-08-2022. [Online]. Available: https://en.wikipedia.org/wiki/Gasoline

[15] A. Zablocki. (2019) Fact sheet: Energy storage. Consulted on: 20/10/2022. [Online]. Available: https://www.eesi.org/papers/view/energy-storage-2019

[16] IRENA, "Making the breakthrough: Green hydrogen policies and technology costs," 2021. [Online]. Available: https://www.irena.org/-/media/Files/IRENA/Agency/Publication/2020/Nov/IRENA_Green_Hydrogen_breakthrough_2021.pdf?la=en&hash=40FA5B8AD7AB1666EECBDE30EF458C45EE5A0AA6

[17] R. Rapier. (2020) Life cycle emissions of hydrogen. [Online]. Available: https://4thgeneration.energy/life-cycles-emissions-of-hydrogen/

[18] The hazer process. Consulted on 20-10-2022. [Online]. Available: https://hazergroup.com.au/about/#hazerprocess

[19] The basf process. Consulted on 20-10-2022. [Online]. Available: https://report.basf.com/2020/en/managements-report/responsibility-along-the-value-chain/environmental-protection-health-and-safety/carbon-management.html

[20] W. de Jong, "Pec versus pv-e a future potential comparison," Master's thesis, 2018.

[21] A. Fujishima and K. Honda, "Electrochemical photolysis of water at a semiconductor electrode," *nature*, vol. 238, no. 5358, pp. 37–38, 1972.

[22] Q. Chen, G. Fan, H. Fu, Z. Li, and Z. Zou, "Tandem photoelectrochemical cells for solar water splitting," *Advances in Physics: X*, vol. 3, no. 1, p. 1487267, 2018.

[23] J. Brillet, J.-H. Yum, M. Cornuz, T. Hisatomi, R. Solarska, J. Augustynski, M. Graetzel, and K. Sivula, "Highly efficient water splitting by a dual-absorber tandem cell," *Nature Photonics*, vol. 6, no. 12, pp. 824–828, 2012.

[24] F. F. Abdi, L. Han, A. H. Smets, M. Zeman, B. Dam, and R. Van De Krol, "Efficient solar water splitting by enhanced charge separation in a bismuth vanadate-silicon tandem photoelectrode," *Nature communications*, vol. 4, no. 1, pp. 1–7, 2013.

[25] Gurudayal, R. A. John, P. P. Boix, C. Yi, C. Shi, M. C. Scott, S. A. Veldhuis, A. M. Minor, S. M. Zakeeruddin, L. H. Wong, M. Grätzel, and N. Mathews, "Atomically altered hematite for highly efficient perovskite tandem water-splitting devices," *ChemSusChem*, vol. 10, no. 11, pp. 2449–2456, 2017.

[26] P. Quitério, "Environmentally friendly photoanodes for solar water splitting," Ph.D. dissertation, Faculty of Sciencies from University of Porto, 2020.

[27] A. G. Tamirat, J. Rick, A. A. Dubale, W.-N. Su, and B.-J. Hwang, "Using hematite for photoelectrochemical water splitting: a review of current progress and challenges," *Nanoscale horizons*, vol. 1, no. 4, pp. 243–267, 2016.

[28] A. Mao, K. Shin, J. K. Kim, D. H. Wang, G. Y. Han, and J. H. Park, "Controlled synthesis of vertically aligned hematite on conducting substrate for photoelectrochemical cells: nanorods versus nanotubes," *ACS applied materials & interfaces*, vol. 3, no. 6, pp. 1852–1858, 2011.

[29] P. Quiterio, A. Apolinario, D. Navas, S. Magalhaes, E. Alves, A. Mendes, C. T. Sousa, and J. P. Araujo, "Photoelectrochemical water splitting: Thermal annealing challenges on hematite nanowires," *The Journal of Physical Chemistry C*, vol. 124, no. 24, pp. 12 897–12 911, 2020.

[30] Z. Najaf, D. L. T. Nguyen, S. Y. Chae, O.-S. Joo, A. U. H. A. Shah, D.-V. N. Vo, V.-H. Nguyen, Q. Van Le, and G. Rahman, "Recent trends in development of hematite (α-fe2o3) as an efficient photoanode for enhancement of photoelectrochemical hydrogen production by solar water splitting," *International Journal of Hydrogen Energy*, vol. 46, no. 45, pp. 23 334–23 357, 2021.

[31] J. Yang, W. Li, J. Li, D. Sun, and Q. Chen, "Hydrothermal synthesis and photoelectrochemical properties of vertically aligned tungsten trioxide (hydrate) plate-like arrays fabricated directly on fto substrates," *Journal of Materials Chemistry*, vol. 22, no. 34, pp. 17 744–17 752, 2012.

[32] T. Zhu, M. N. Chong, Y. W. Phuan, and E.-S. Chan, "Electrochemically synthesized tungsten trioxide nanostructures for photoelectrochemical water splitting: Influence of heat treatment on physicochemical properties, photocurrent densities and electron shuttling," *Colloids and Surfaces A: Physicochemical and Engineering Aspects*, vol. 484, pp. 297–303, 2015.

[33] T. Zhu, M. N. Chong, Y. W. Phuan, J. D. Ocon, and E. S. Chan, "Effects of electrodeposition synthesis parameters on the photoactivity of nanostructured tungsten trioxide thin films: optimisation study using response surface methodology," *Journal of the Taiwan Institute of Chemical Engineers*, vol. 61, pp. 196–204, 2016.

[34] R. Daghrir, P. Drogui, and M. A. El Khakani, "Photoelectrocatalytic oxidation of chlortetracycline using ti/tio2 photo-anode with simultaneous h2o2 production," *Electrochimica acta*, vol. 87, pp. 18–31, 2013.

[35] H. Li, Q. Zhou, Y. Gao, X. Gui, L. Yang, M. Du, E. Shi, J. Shi, A. Cao, and Y. Fang, "Templated synthesis of tio2 nanotube macrostructures and their photocatalytic properties," *Nano Research*, vol. 8, no. 3, pp. 900–906, 2015.

[36] M. S. A. S. Shah, K. Zhang, A. R. Park, K. S. Kim, N.-G. Park, J. H. Park, and P. J. Yoo, "Single-step solvothermal synthesis of mesoporous ag–tio 2–reduced graphene oxide ternary composites with enhanced photocatalytic activity," *Nanoscale*, vol. 5, no. 11, pp. 5093–5101, 2013.

[37] A. Murphy, P. Barnes, L. Randeniya, I. Plumb, I. Grey, M. Horne, and J. Glasscock, "Efficiency of solar water splitting using semiconductor electrodes," *International journal of hydrogen energy*, vol. 31, no. 14, pp. 1999–2017, 2006.

[38] F. Morin, "Electrical properties of α-fe 2 o 3," *Physical Review*, vol. 93, no. 6, p. 1195, 1954.

[39] J. H. Kennedy and K. W. Frese, "Photooxidation of water at α-fe2 o 3 electrodes," *Journal of the Electrochemical Society*, vol. 125, no. 5, p. 709, 1978.

[40] N. J. Cherepy, D. B. Liston, J. A. Lovejoy, H. Deng, and J. Z. Zhang, "Ultrafast studies of photoexcited electron dynamics in γ-and α-fe2o3 semiconductor nanoparticles," *The Journal of Physical Chemistry B*, vol. 102, no. 5, pp. 770–776, 1998.

[41] R. M. Cornell, U. Schwertmann *et al.*, *The iron oxides: structure, properties, reactions, occurrences, and uses*. Wiley-vch Weinheim, 2003, vol. 664.

[42] K. Sivula, F. Le Formal, and M. Grätzel, "Solar water splitting: progress using hematite (α-fe2o3) photoelectrodes," *ChemSusChem*, vol. 4, no. 4, pp. 432–449, 2011.

[43] S. Shen, S. A. Lindley, X. Chen, and J. Z. Zhang, "Hematite heterostructures for photoelectrochemical water splitting: rational materials design and charge carrier dynamics," *Energy & Environmental Science*, vol. 9, no. 9, pp. 2744–2775, 2016.

[44] M. Cornuz, M. Grätzel, and K. Sivula, "Preferential orientation in hematite films for solar hydrogen production via water splitting," *Chemical Vapor Deposition*, vol. 16, no. 10-12, pp. 291–295, 2010.

[45] K. Sivula, R. Zboril, F. Le Formal, R. Robert, A. Weidenkaff, J. Tucek, J. Frydrych, and M. Gratzel, "Photoelectrochemical water splitting with mesoporous hematite prepared by a solution-based colloidal approach," *Journal of the American Chemical Society*, vol. 132, no. 21, pp. 7436–7444, 2010.

[46] A. Galuza, A. Beznosov, and V. Eremenko, "Optical absorption edge in α–fe 2 o 3: The exciton–magnon structure," *Low Temperature Physics*, vol. 24, no. 10, pp. 726–729, 1998.

[47] I. Balberg and H. Pinch, "The optical absorption of iron oxides," *Journal of Magnetism and Magnetic Materials*, vol. 7, no. 1-4, pp. 12–15, 1978.

[48] B. Iandolo, B. Wickman, I. Zorić, and A. Hellman, "The rise of hematite: origin and strategies to reduce the high onset potential for the oxygen evolution reaction," *Journal of Materials Chemistry A*, vol. 3, no. 33, pp. 16 896–16 912, 2015.

[49] C. Sanchez, K. Sieber, and G. Somorjai, "The photoelectrochemistry of niobium doped α-fe2o3," *Journal of electroanalytical chemistry and interfacial electrochemistry*, vol. 252, no. 2, pp. 269–290, 1988.

[50] P. S. Bassi, L. H. Wong, J. Barber *et al.*, "Iron based photoanodes for solar fuel production," *Physical Chemistry Chemical Physics*, vol. 16, no. 24, pp. 11 834–11 842, 2014.

[51] K. M. Rosso, D. M. Smith, and M. Dupuis, "An ab initio model of electron transport in hematite (α-fe 2 o 3) basal planes," *The Journal of chemical physics*, vol. 118, no. 14, pp. 6455–6466, 2003.

[52] N. J. Cherepy, D. B. Liston, J. A. Lovejoy, H. Deng, and J. Z. Zhang, "Ultrafast studies of photoexcited electron dynamics in γ-and α-fe2o3 semiconductor nanoparticles," *The Journal of Physical Chemistry B*, vol. 102, no. 5, pp. 770–776, 1998.

[53] S. D. Tilley, M. Cornuz, K. Sivula, and M. Grätzel, "Light-induced water splitting with hematite: improved nanostructure and iridium oxide catalysis," *Angewandte Chemie International Edition*, vol. 49, no. 36, pp. 6405–6408, 2010.

[54] S. C. Warren, K. Voïtchovsky, H. Dotan, C. M. Leroy, M. Cornuz, F. Stellacci, C. Hébert, A. Rothschild, and M. Grätzel, "Identifying champion nanostructures for solar water-splitting," *Nature materials*, vol. 12, no. 9, pp. 842–849, 2013.

[55] J. Christian, R. Singh Gaur, T. Wolfe, and J. Trasorras, "Tungsten chemicals and their applications," *International Tungsten Industry Association: London, UK*, 2011.

[56] W. J. Lee, Y.-K. Fang, J.-J. Ho, W.-T. Hsieh, S.-F. Ting, D. Huang, and F. C. Ho, "Effects of surface porosity on tungsten trioxide (wo3) films electrochromic performance," *Journal of electronic materials*, vol. 29, no. 2, pp. 183–187, 2000.

[57] G. Hodes, D. Cahen, and J. Manassen, "Tungsten trioxide as a photoanode for a photoelectrochemical cell (pec)," *Nature*, vol. 260, no. 5549, pp. 312–313, 1976.

[58] H. Zheng, J. Z. Ou, M. S. Strano, R. B. Kaner, A. Mitchell, and K. Kalantar-zadeh, "Nanostructured tungsten oxide–properties, synthesis, and applications," *Advanced Functional Materials*, vol. 21, no. 12, pp. 2175–2196, 2011.

[59] S. S. Kalanur, L. T. Duy, and H. Seo, "Recent progress in photoelectrochemical water splitting activity of wo3 photoanodes," *Topics in Catalysis*, vol. 61, no. 9, pp. 1043–1076, 2018.

[60] X. Liu, F. Wang, and Q. Wang, "Nanostructure-based wo 3 photoanodes for photoelectrochemical water splitting," *Physical Chemistry Chemical Physics*, vol. 14, no. 22, pp. 7894–7911, 2012.

[61] T. Vogt, P. M. Woodward, and B. A. Hunter, "The high-temperature phases of wo3," *Journal of Solid State Chemistry*, vol. 144, no. 1, pp. 209–215, 1999.

[62] B. Gerand, G. Nowogrocki, J. Guenot, and M. Figlarz, "Structural study of a new hexagonal form of tungsten trioxide," *Journal of Solid State Chemistry*, vol. 29, no. 3, pp. 429–434, 1979.

[63] D. Migas, V. Shaposhnikov, V. Rodin, and V. Borisenko, "Tungsten oxides. i. effects of oxygen vacancies and doping on electronic and optical properties of different phases of wo 3," *Journal of Applied Physics*, vol. 108, no. 9, p. 093713, 2010.

[64] K. H. Yoon, J. W. Lee, Y. S. Cho, and D. H. Kang, "Structural and photocurrent–voltage characteristics of tungsten oxide thin films on p-gaas," *Applied physics letters*, vol. 68, no. 4, pp. 572–574, 1996.

[65] P. Shandilya, S. Sambyal, R. Sharma, P. Mandyal, and B. Fang, "Properties, optimized morphologies, and advanced strategies for photocatalytic applications of wo3 based photocatalysts," *Journal of Hazardous Materials*, p. 128218, 2022.

[66] R. Vemuri, K. K. Bharathi, S. Gullapalli, and C. Ramana, "Effect of structure and size on the electrical properties of nanocrystalline wo3 films," *ACS applied materials & interfaces*, vol. 2, no. 9, pp. 2623–2628, 2010.

[67] Y. Li, J. Feng, H. Li, X. Wei, R. Wang, and A. Zhou, "Photoelectrochemical splitting of natural seawater with α-fe2o3/wo3 nanorod arrays," *International Journal of Hydrogen Energy*, vol. 41, no. 7, pp. 4096–4105, 2016.

[68] Q. Wu, Q. Bu, S. Li, Y. Lin, X. Zou, D. Wang, and T. Xie, "Enhanced interface charge transfer via nn wo3/ti–fe2o3 heterojunction formation for water splitting," *Journal of Alloys and Compounds*, vol. 803, pp. 1105–1111, 2019.

[69] S. K. Mohapatra, S. E. John, S. Banerjee, and M. Misra, "Water photooxidation by smooth and ultrathin α-fe2o3 nanotube arrays," *Chemistry of Materials*, vol. 21, no. 14, pp. 3048–3055, 2009.

[70] A. Mao, G. Y. Han, and J. H. Park, "Synthesis and photoelectrochemical cell properties of vertically grown α-fe 2 o 3 nanorod arrays on a gold nanorod substrate," *Journal of Materials Chemistry*, vol. 20, no. 11, pp. 2247–2250, 2010.

[71] T. Liu, Y. Ling, Y. Yang, L. Finn, E. Collazo, T. Zhai, Y. Tong, and Y. Li, "Investigation of hematite nanorod–nanoflake morphological transformation and the application of ultrathin nanoflakes for electrochemical devices," *Nano Energy*, vol. 12, pp. 169–177, 2015.

[72] A. Duret and M. Grätzel, "Visible light-induced water oxidation on mesoscopic α-fe2o3 films made by ultrasonic spray pyrolysis," *The Journal of Physical Chemistry B*, vol. 109, no. 36, pp. 17 184–17 191, 2005.

[73] J. S. Nyarige, T. P. Krüger, and M. Diale, "Structural and optical properties of hematite and l-arginine/hematite nanostructures prepared by thermal spray pyrolysis," *Surfaces and Interfaces*, vol. 18, p. 100394, 2020.

[74] L. Vayssieres, N. Beermann, S.-E. Lindquist, and A. Hagfeldt, "Controlled aqueous chemical growth of oriented three-dimensional crystalline nanorod arrays: Application to iron (iii) oxides," *Chemistry of materials*, vol. 13, no. 2, pp. 233–235, 2001.

[75] M. Wang, H. Wang, Q. Wu, C. Zhang, and S. Xue, "Morphology regulation and surface modification of hematite nanorods by aging in phosphate solutions for efficient pec water splitting," *International Journal of Hydrogen Energy*, vol. 41, no. 15, pp. 6211–6219, 2016.

[76] E. L. Tsege, T. S. Atabaev, M. A. Hossain, D. Lee, H.-K. Kim, and Y.-H. Hwang, "Cu-doped flower-like hematite nanostructures for efficient water splitting applications," *Journal of Physics and Chemistry of Solids*, vol. 98, pp. 283–289, 2016.

[77] H. Srivastava, P. Tiwari, A. Srivastava, and R. V. Nandedkar, "Growth and characterization of α-fe2o3 nanowires," *Journal of Applied Physics*, vol. 102, p. 054303, 2007.

[78] A. Mao, N.-G. Park, G. Y. Han, and J. H. Park, "Controlled growth of vertically oriented hematite/pt composite nanorod arrays: use for photoelectrochemical water splitting," *Nanotechnology*, vol. 22, no. 17, p. 175703, 2011.

[79] T. J. LaTempa, X. Feng, M. Paulose, and C. A. Grimes, "Temperature-dependent growth of self-assembled hematite (α-fe2o3) nanotube arrays: rapid electrochemical synthesis and photoelectrochemical properties," *The Journal of Physical Chemistry C*, vol. 113, no. 36, pp. 16 293–16 298, 2009.

[80] M. G. Ahmed, I. E. Kretschmer, T. A. Kandiel, A. Y. Ahmed, F. A. Rashwan, and D. W. Bahnemann, "A facile surface passivation of hematite photoanodes with tio2 overlayers for efficient solar water splitting," *ACS Applied Materials & Interfaces*, vol. 7, no. 43, pp. 24 053–24 062, 2015.

[81] X.-L. Cheng, J.-S. Jiang, C.-Y. Jin, C.-C. Lin, Y. Zeng, and Q.-H. Zhang, "Cauliflower-like -fe2o3 microstructures: Toluenewater interface-assisted synthesis, characterization, and

applications in wastewater treatment and visible-light photocatalysis," *Chemical Engineering Journal*, vol. 236, pp. 139–148, 2014.

[82] L. Wang, H. Hu, N. T. Nguyen, Y. Zhang, P. Schmuki, and Y. Bi, "Plasmon-induced hole-depletion layer on hematite nanoflake photoanodes for highly efficient solar water splitting," *Nano Energy*, vol. 35, pp. 171–178, 2017.

[83] B. J. Rani, M. P. Kumar, G. Ravi, S. Ravichandran, R. K. Guduru, and R. Yuvakkumar, "Electrochemical and photoelectrochemical water oxidation of solvothermally synthesized zr-doped α-fe2o3 nanostructures," *Applied Surface Science*, vol. 471, pp. 733–744, 2019.

[84] J. Liu, Y. Cai, Z. Tian, G. Ruan, Y. Ye, C. Liang, and G. Shao, "Highly oriented ge-doped hematite nanosheet arrays for photoelectrochemical water oxidation," *Nano Energy*, vol. 9, pp. 282–290, 2014.

[85] R. van de Krol, Y. Liang, and J. Schoonman, "Solar hydrogen production with nanostructured metal oxides," *Journal of Materials Chemistry*, vol. 18, no. 20, pp. 2311–2320, 2008.

[86] N. Beermann, L. Vayssieres, S.-E. Lindquist, and A. Hagfeldt, "Photoelectrochemical studies of oriented nanorod thin films of hematite," *Journal of the Electrochemical Society*, vol. 147, no. 7, p. 2456, 2000.

[87] K. Byrappa, N. Keerthiraj, and S. M. Byrappa, "Hydrothermal growth of crystalsdesign and processing," in *Handbook of Crystal Growth*. Elsevier, 2015, pp. 535–575.

[88] K. Chen, X. Chen, and D. Xue, "Hydrothermal route to crystallization of feooh nanorods via fecl 3· 6h 2 o: effect of fe 3+ concentration on pseudocapacitance of iron-based materials," *CrystEngComm*, vol. 17, no. 9, pp. 1906–1910, 2015.

[89] A. Liu, Y. Zhang, W. Ma, W. Song, C. Chen, and J. Zhao, "Facial boron incorporation in hematite photoanode for enhanced photoelectrochemical water oxidation," *Journal of Photochemistry and Photobiology A: Chemistry*, vol. 355, pp. 290–297, 2018.

[90] F. Bouhjar, M. Mollar, M. Chourou, B. Marí, and B. Bessais, "Hydrothermal synthesis of nanostructured cr-doped hematite with enhanced photoelectrochemical activity," *Electrochimica Acta*, vol. 260, pp. 838–846, 2018.

[91] Y. Ling, G. Wang, D. A. Wheeler, J. Z. Zhang, and Y. Li, "Sn-doped hematite nanostructures for photoelectrochemical water splitting," *Nano Letters*, vol. 11, no. 5, pp. 2119–2125, 2011.

[92] L. Xi, S. Y. Chiam, W. F. Mak, P. D. Tran, J. Barber, S. C. J. Loo, and L. H. Wong, "A novel strategy for surface treatment on hematite photoanode for efficient water oxidation," *Chemical Science*, vol. 4, no. 1, pp. 164–169, 2013.

[93] L. Xi, P. D. Tran, S. Y. Chiam, P. S. Bassi, W. F. Mak, H. K. Mulmudi, S. K. Batabyal, J. Barber, J. S. C. Loo, and L. H. Wong, "Co3o4-decorated hematite nanorods as an effective photoanode for solar water oxidation," *The Journal of Physical Chemistry C*, vol. 116, no. 26, pp. 13 884–13 889, 2012.

[94] Gurudayal, S. Y. Chiam, M. H. Kumar, P. S. Bassi, H. L. Seng, J. Barber, and L. H. Wong, "Improving the efficiency of hematite nanorods for photoelectrochemical water splitting by doping with manganese," *ACS applied materials & interfaces*, vol. 6, no. 8, pp. 5852–5859, 2014.

[95] J. Huang, G. Hu, Y. Ding, M. Pang, and B. Ma, "Mn-doping and nife layered double hydroxide coating: effective approaches to enhancing the performance of α-fe2o3 in photoelectrochemical water oxidation," *Journal of Catalysis*, vol. 340, pp. 261–269, 2016.

[96] W. M. de Carvalho and F. L. Souza, "Recent advances on solar water splitting using hematite nanorod film produced by purpose-built material methods," *Journal of materials research*, vol. 29, no. 1, pp. 16–28, 2014.

[97] J. H. Davies, *The physics of low-dimensional semiconductors: an introduction*. Cambridge university press, 1998.

[98] Z. Fu, T. Jiang, Z. Liu, D. Wang, L. Wang, and T. Xie, "Highly photoactive ti-doped α-fe2o3 nanorod arrays photoanode prepared by a hydrothermal method for photoelectrochemical water splitting," *Electrochimica Acta*, vol. 129, pp. 358–363, 2014.

[99] Y.-C. Chen, C.-L. Kuo, and Y.-K. Hsu, "Facile preparation of zn-doped hematite thin film as photocathode for solar hydrogen generation," *Journal of Alloys and Compounds*, vol. 768, pp. 810–816, 2018.

[100] J. Wang, C. Du, Q. Peng, J. Yang, Y. Wen, B. Shan, and R. Chen, "Enhanced photoelectrochemical water splitting performance of hematite nanorods by co and sn co-doping," *international journal of hydrogen energy*, vol. 42, no. 49, pp. 29 140–29 149, 2017.

[101] Y. Liu, Y.-X. Yu, and W.-D. Zhang, "Photoelectrochemical properties of ni-doped fe2o3 thin films prepared by electrodeposition," *Electrochimica acta*, vol. 59, pp. 121–127, 2012.

[102] X. Guo, L. Wang, and Y. Tan, "Hematite nanorods co-doped with ru cations with different valence states as high performance photoanodes for water splitting," *Nano Energy*, vol. 16, pp. 320–328, 2015.

[103] T.-Y. Yang, H.-Y. Kang, K. Jin, S. Park, J.-H. Lee, U. Sim, H.-Y. Jeong, Y.-C. Joo, and K. T. Nam, "An iron oxide photoanode with hierarchical nanostructure for efficient water oxidation," *Journal of Materials Chemistry A*, vol. 2, no. 7, pp. 2297–2305, 2014.

[104] M. H. Lee, J. H. Park, H. S. Han, H. J. Song, I. S. Cho, J. H. Noh, and K. S. Hong, "Nanostructured ti-doped hematite (-fe2o3) photoanodes for efficient photoelectrochemical water oxidation," *International Journal of Hydrogen Energy*, vol. 39, no. 30, pp. 17 501–17 507, 2014.

[105] S. Y. Chae, G. Rahman, and O.-s. Joo, "Elucidation of the structural and charge separation properties of titanium-doped hematite films deposited by electrospray method for photoelectrochemical water oxidation," *Electrochimica Acta*, vol. 297, pp. 784–793, 2019.

[106] D. Sharma, S. Upadhyay, A. Verma, V. R. Satsangi, R. Shrivastav, and S. Dass, "Nanostructured ti-fe2o3/cu2o heterojunction photoelectrode for efficient hydrogen production," *Thin Solid Films*, vol. 574, pp. 125–131, 2015.

[107] C. Zheng, Z. Zhu, S. Wang, and Y. Hou, "Naf-assisted hydrothermal synthesis of ti-doped hematite nanocubes with enhanced photoelectrochemical activity for water splitting," *Applied Surface Science*, vol. 359, pp. 805–811, 2015.

[108] W. B. Ingler Jr, J. P. Baltrus, and S. U. Khan, "Photoresponse of p-type zinc-doped iron (iii) oxide thin films," *Journal of the American Chemical Society*, vol. 126, no. 33, pp. 10 238–10 239, 2004.

[109] J. Deng, J. Zhong, A. Pu, D. Zhang, M. Li, X. Sun, and S.-T. Lee, "Ti-doped hematite nanostructures for solar water splitting with high efficiency," *Journal of Applied Physics*, vol. 112, no. 8, p. 084312, 2012.

[110] L. Wang, C.-Y. Lee, and P. Schmuki, "Ti and sn co-doped anodic α-fe2o3 films for efficient water splitting," *Electrochemistry communications*, vol. 30, pp. 21–25, 2013.

[111] R. Mazzaro, S. B. Bibi, M. Natali, G. Bergamini, V. Morandi, P. Ceroni, and A. Vomiero, "Hematite nanostructures: An old material for a new story. simultaneous photoelectrochemical oxidation of benzylamine and hydrogen production through ti doping," *Nano Energy*, vol. 61, pp. 36–46, 2019.

[112] F. Wu, J. Xie, Y. You, Z. Zhao, L. Wang, X. Chen, P. Yang, and Y. Huang, "Cobalt metal–organic framework ultrathin cocatalyst overlayer for improved photoelectrochemical activity of ti-doped hematite," *ACS Applied Energy Materials*, vol. 3, no. 5, pp. 4867–4876, 2020.

[113] F. Francisco, P. Dias, D. Ivanou, F. Santos, J. Azevedo, and A. Mendes, "Synthesis of host-guest hematite photoelectrodes for solar water splitting," *ChemNanoMat*, vol. 5, no. 7, pp. 911–920, 2019.

[114] K. Chen, X. Chen, and D. Xue, "Hydrothermal route to crystallization of feooh nanorods via fecl 3· 6h 2 o: effect of fe 3+ concentration on pseudocapacitance of iron-based materials," *CrystEngComm*, vol. 17, no. 9, pp. 1906–1910, 2015.

[115] A. Apolinario, T. Lopes, C. Costa, J. P. Araujo, and A. M. Mendes, "Multilayered wo3 nanoplatelets for efficient photoelectrochemical water splitting: the role of the annealing ramp," *ACS Applied Energy Materials*, vol. 2, no. 2, pp. 1040–1050, 2019.

[116] R. G. Gordon, "Criteria for choosing transparent conductors," *MRS bulletin*, vol. 25, no. 8, pp. 52–57, 2000.

[117] A. M. N. Vilanova, "Photoelectrochemical devices for solar hydrogen production," 2021.

[118] J. I. Goldstein, D. E. Newbury, P. Echlin, D. C. Joy, C. Fiori, and E. Lifshin, *Scanning electron microscopy and X-ray microanalysis - A Text for Biologists, Materials Scientists, and Geologists*. Plenum Press, New York, 1981.

[119] W. Zhou and Z. L. Wang, *Scanning microscopy for nanotechnology: techniques and applications*. Springer science & business media, 2007.

[120] V. K. Zworykin, "The scanning electron microscope," *Scientific American*, vol. 167, no. 3, pp. 111–113, 1942.

[121] L. Reimer, *Scanning electron microscopy: physics of image formation and microanalysis*. Springer, 1998.

[122] A. Chauhan, "Deformation and damage mechanisms of ods steels under high-temperature cyclic loading," Ph.D. dissertation, 02 2018.

[123] Microscopy. [Online]. Available: https://sites.ualberta.ca/~ccwj/teaching/microscopy/

[124] Y. Leng, *Materials Characterization: Introduction to Microscopic and Spectroscopic Methods*. John Wiley & Sons, 2008.

[125] C. Kittel, P. McEuen, and P. McEuen, *Introduction to solid state physics*. John Wiley & Sons, 1996, vol. 7.

[126] W. D. Callister, *Materials Science and Engineering: An Introduction*. John Wiley & Sons, 2006, vol. 7.

[127] G. Williamson and W. Hall, "X-ray line broadening from filed aluminium and wolfram," *Acta metallurgica*, vol. 1, no. 1, pp. 22–31, 1953.

[128] W. Grant, *Methods of Surface Analysis: Techniques and Applications*. Cambridge University Press, 1989, ch. Rutherford back-scattering spectrometry.

[129] S. N. C. de Magalhães, "Caracterizaçao e modificaçao de heteroestruturas de nitretos do grupo iii," Ph.D. dissertation, Universidade de Aveiro (Portugal), 2013.

[130] H. Geiger and E. Marsden, "Lxi. the laws of deflexion of a particles through large angles," *The London, Edinburgh, and Dublin Philosophical Magazine and Journal of Science*, vol. 25, no. 148, pp. 604–623, 1913.

[131] W.-K. Chu, *Backscattering spectrometry*. Academic Press, 1978.

[132] E. N. Kaufmann, *Characterization of Materials, 2 Volume Set*. John Wiley & Sons, 2003.

[133] N. Barradas, C. Jeynes, and R. Webb, "Simulated annealing analysis of rutherford backscattering data," *Applied Physics Letters*, vol. 71, no. 2, pp. 291–293, 1997.

[134] J. F. Ziegler, M. D. Ziegler, and J. P. Biersack, "Srim–the stopping and range of ions in matter (2010)," *Nuclear Instruments and Methods in Physics Research Section B: Beam Interactions with Materials and Atoms*, vol. 268, no. 11-12, pp. 1818–1823, 2010.

[135] X. Shi, L. Cai, M. Ma, X. Zheng, and J. H. Park, "General characterization methods for photoelectrochemical cells for solar water splitting," *ChemSusChem*, vol. 8, no. 19, pp. 3192–3203, 2015.

[136] T. Lopes, L. Andrade, F. Le Formal, M. Gratzel, K. Sivula, and A. Mendes, "Hematite photoelectrodes for water splitting: evaluation of the role of film thickness by impedance spectroscopy," *Physical Chemistry Chemical Physics*, vol. 16, no. 31, pp. 16 515–16 523, 2014.

[137] A. J. Bard, L. R. Faulkner, and H. S. White, *Electrochemical methods: fundamentals and applications*. John Wiley & Sons, 2022.

[138] T. S. T. Lopes, "Characterization and phenomenological modeling of photoelectrochemical cells for hydrogen production from solar energy," Ph.D. dissertation, Universidade do Porto (Portugal), 2014.

[139] S. Zhang, L. Li, and A. Kumar, *Materials characterization techniques*. Taylor & Francis Group, LLC, 2009.

[140] J. Tauc, "Optical properties and electronic structure of amorphous ge and si," *Materials research bulletin*, vol. 3, no. 1, pp. 37–46, 1968.

[141] B. A. Balko and K. M. Clarkson, "The effect of doping with ti (iv) and sn (iv) on oxygen reduction at hematite electrodes," *Journal of the Electrochemical Society*, vol. 148, no. 2, p. E85, 2001.

[142] H. G. Cha, H. S. Noh, M. J. Kang, and Y. S. Kang, "Photocatalysis: progress using manganese-doped hematite nanocrystals," *New Journal of Chemistry*, vol. 37, no. 12, pp. 4004–4009, 2013.

[143] R. Ramprasath, V. Manikandan, S. Aldawood, S. Sudha, S. Cholan, N. Kannadasan, S. Sampath, and B. Gokul, "Polyol-assisted hydrothermal synthesis of mn-doped α–fe2o3 (mfo) nanostructures: Spin disorder-induced magnetism and photocatalytic properties." *Environmental Research*, vol. 214, p. 113866, 2022.

[144] D. Varshney and A. Yogi, "Structural and electrical conductivity of mn doped hematite (α-fe2o3) phase," *Journal of Molecular Structure*, vol. 995, no. 1-3, pp. 157–162, 2011.

[145] M. Grätzel, "Photoelectrochemical cells," *nature*, vol. 414, no. 6861, pp. 338–344, 2001.

[146] A. de Cerdeira Oliveira, "H2 solar: Photoelectrochemical cells for water splitting," Master's thesis, Faculty of Sciencies from University of Porto, 2021.

[147] P. S. Shinde, S. H. Choi, Y. Kim, J. Ryu, and J. S. Jang, "Onset potential behavior in α-fe 2 o 3 photoanodes: the influence of surface and diffusion sn doping on the surface states," *Physical Chemistry Chemical Physics*, vol. 18, no. 4, pp. 2495–2509, 2016.

[148] S. Kment, P. Schmuki, Z. Hubicka, L. Machala, R. Kirchgeorg, N. Liu, L. Wang, K. Lee, J. Olejnicek, M. Cada *et al.*, "Photoanodes with fully controllable texture: the enhanced water splitting efficiency of thin hematite films exhibiting solely (110) crystal orientation," *ACS nano*, vol. 9, no. 7, pp. 7113–7123, 2015.

[149] N. Iordanova, M. Dupuis, and K. M. Rosso, "Charge transport in metal oxides: a theoretical study of hematite α-fe 2 o 3," *The Journal of chemical physics*, vol. 122, no. 14, p. 144305, 2005.

[150] S. Magalhães, M. Dias, B. Nunes, F. Oliveira, M. Cerqueira, and E. Alves, "Confronting vegards rule in ge1- x sn x epilayers: from fundamentals to the effect of defects," *Journal of Physics D: Applied Physics*, vol. 55, no. 29, p. 295301, 2022.

[151] A. Annamalai, H. H. Lee, S. H. Choi, S. Y. Lee, E. Gracia-Espino, A. Subramanian, J. Park, K.-j. Kong, and J. S. Jang, "Sn/be sequentially co-doped hematite photoanodes for enhanced photoelectrochemical water oxidation: effect of be2+ as co-dopant," *Scientific reports*, vol. 6, no. 1, pp. 1–11, 2016.

[152] M. P. Proenca, C. T. Sousa, A. M. Pereira, P. B. Tavares, J. Ventura, M. Vazquez, and J. P. Araujo, "Size and surface effects on the magnetic properties of nio nanoparticles," *Physical Chemistry Chemical Physics*, vol. 13, no. 20, pp. 9561–9567, 2011.

[153] MROX software. [Online]. Available: https://www.mrox.eu/software/pt/

[154] V. V. Deshmane and A. V. Patil, "Cobalt oxide doped hematite as a petrol vapor sensor," *Materials Chemistry and Physics*, vol. 246, p. 122813, 2020.

[155] A. H. Asif, N. Rafique, R. A. K. Hirani, H. Wu, L. Shi, and H. Sun, "Heterogeneous activation of peroxymonosulfate by co-doped fe2o3 nanospheres for degradation of p-hydroxybenzoic acid," *Journal of Colloid and Interface Science*, vol. 604, pp. 390–401, 2021.

[156] W. L. Kwong, C. C. Lee, A. Shchukarev, and J. Messinger, "Cobalt-doped hematite thin films for electrocatalytic water oxidation in highly acidic media," *Chemical Communications*, vol. 55, no. 34, pp. 5017–5020, 2019.

[157] P. Dias, T. Lopes, L. Meda, L. Andrade, and A. Mendes, "Photoelectrochemical water splitting using wo 3 photoanodes: the substrate and temperature roles," *Physical Chemistry Chemical Physics*, vol. 18, no. 7, pp. 5232–5243, 2016.

[158] T. Lopes, L. Andrade, and A. Mendes, "Photoelectrochemical cells for hydrogen production from solar energy," *Solar Energy Sciences and Engineering Applications*, 2013.

[159] M. Simić, A. K. Stavrakis, and G. M. Stojanović, "A low-complexity method for parameter estimation of the simplified randles circuit with experimental verification," *IEEE Sensors Journal*, vol. 21, no. 21, pp. 24 209–24 217, 2021.

[160] R. Van de Krol, M. Grätzel *et al.*, *Photoelectrochemical hydrogen production*. Springer, 2012, vol. 90.

[161] Z. Zhou, Z. Wu, Q. Xu, and G. Zhao, "A solar-charged photoelectrochemical wastewater fuel cell for efficient and sustainable hydrogen production," *Journal of Materials Chemistry A*, vol. 5, no. 48, pp. 25 450–25 459, 2017.

[162] G. Roselló-Márquez, R. M. Fernández-Domene, R. Sánchez-Tovar, and J. Garcia-Anton, "Influence of annealing conditions on the photoelectrocatalytic performance of wo3 nanostructures," *Separation and Purification Technology*, vol. 238, p. 116417, 2020.

[163] S. M. Gonçalves, "Customization of thermal expansion in nanowires," 2021.

[164] A. Kay, D. A. Grave, D. S. Ellis, H. Dotan, and A. Rothschild, "Heterogeneous doping to improve the performance of thin-film hematite photoanodes for solar water splitting," *ACS Energy Letters*, vol. 1, no. 4, pp. 827–833, 2016.

[165] S.-M. Tao and L.-Y. Lin, "Design of efficient mn-doped α-fe2o3/ti-doped α-fe2o3 homojunction for catalyzing photoelectrochemical water splitting," *International Journal of Hydrogen Energy*, vol. 45, no. 11, pp. 6487–6499, 2020.